ABSTRACT

Title of Dissertation: INTEGRATED TEMPERATURE MEASUREMENT AND CONTROL IN POLYMER MICROFLUIDIC SYSTEMS

Christopher Robert Kimball, Doctor of Philosophy, 2003

Dissertation directed by: Associate Professor Don DeVoe
Department of Mechanical Engineering

Methods for integrating electrical components in low cost polymer microfluidic systems are presented. These methods include deposition and photolithographic patterning of thin-film metal layers on polycarbonate and poly(methyl methacrylate), and the embedding of pre-fabricated and diced chips. The design and performance of Resistive Temperature Detectors (RTDs) fabricated with these methods is also discussed.

The fabrication and testing of two polymer microfluidic systems is presented. The first system contains a two-dimensional array of RTDs in a microchannel capable of measuring the temperature distribution within the fluid. The second system employs Temperature Gradient Gel Electrophoresis (TGGE) for the detection of mutations in DNA samples.

A compact mathematical model of the thermal effects caused by an integrated microheater is presented and validated with experimental measurements. This model may be applied to a wide variety of polymer microsystems which contain heaters and/or temperature sensors. The design of bubble pumps, hot plate chemical sensors, temperature gradient gel/capillary electrophoresis systems, flow sensors, etc. will be aided by this model.

INTEGRATED TEMPERATURE MEASUREMENT AND CONTROL IN POLYMER MICROFLUIDIC SYSTEMS

by

Christopher Robert Kimball

Dissertation submitted to the Faculty of the Graduate School of the
University of Maryland, College Park in partial fulfillment
of the requirements for the degree of
Doctor of Philosophy
2003

Advisory Committee:

Associate Professor Don DeVoe, Chair
Associate Professor Bongtae Han
Associate Professor Cheng Lee
Assistant Professor Benjamin Shapiro
Assistant Professor Elisabeth Smela

FORWARD

The dissertation submitted to the Faculty of the Graduate School of the University of Maryland, College Park, entitled "Integrated Temperature Measurement and Control in Polymer Microfluidic Systems" contains the following previously published work.

Chapter 2 contains work published in *Micro Total Analysis Systems 2003*, entitled "Integrated Microfluidic Gas Sensor for Water Monitoring". The authors of this publication are L. Zhu, C. Kimball, N. Sniadecki, M. Beamesderfer, S. Semancik, and D.L. DeVoe. Mr. Kimball has made a substantial contribution to this work, including:

- Development of a technique for embedding silicon chips in epoxy without the presence of gaps or bubbles at the periphery of the chip.
- Concept of planarization of the silicon-epoxy surface with photo-definable polyimide to allow the deposition and patterning of thin metal films for electrical contact with the silicon chip.

Chapter 4 contains work published in *Proceedings of Transducers'03*, entitled "Temperature Gradient Gel Electrophoresis in an Integrated Polycarbonate Microsystem". The authors of this publication are C. Kimball, J. Buch, C. Lee, and D.L. DeVoe. Mr. Kimball has made a substantial contribution to this work, including:

- Design analysis, and fabrication of a thin film microheater system for establishing a two-dimensional temperature gradient.
- Design and development of an automated measurement and control system for sensing and controlling the two-dimensional temperature gradient.

The inclusion of this work has been approved by the Dissertation Chair, Dr. Don DeVoe, and by the Director of Graduate Studies in Mechanical Engineering, Dr. Ugo Piomelli.

DEDICATION

To Natalya and my mother for their support and encouragement in this endeavor.

ACKNOWLEDGEMENTS

I would like thank my advisor, Dr. Don DeVoe, for his support and insight throughout this work. I am also very grateful to my former advisor, Dr. Lung-Wen Tsai, who drew me to Maryland and guided me in my first 2 1/2 years here. I am indebted to Tom Laughran for his expertise and many, many e-beam runs. Finally, I would like to thank my friends and colleagues here at the University, especially Nate Sniadecki, Sean Andersson, Sameer Joshi, and Mandar Chincholkar, for their assistance and good humor over the last 5 years. This work was funded in part by the National Cancer Institute through grant CA092819. We would like to thank Dr. Ed Highsmith (Mayo Clinic in Rochester, MN) for graciously providing the DNA used in this study.

TABLE OF CONTENTS

LIST OF TABLES

LIST OF FIGURES

Chapter 1

Introduction

1.1 Integrated Microfluidics in Silicon, Glass, and Quartz

The first microfluidic device was reported in 1979, and consisted of a gas chromatography system fabricated in silicon [1]. Since then, microfluidic devices have found many applications in chemical detection and chemical analysis, due to the many advantages such systems offer over conventional detection and analysis devices. The required sample volumes are greatly reduced, the analysis times may be reduced, the cost is reduced, and the devices may be made portable and possibly even disposable. The simplest type of microfluidic device consists of only a micromachined channel filled with a fluid which is manipulated externally. A myriad such devices have been reported, and some are commercially available. For example, Agilent Technologies sells a system, the Agilent Bioanalyzer, which incorporates a micromachined channel in glass for capillary electrophoresis. External electrodes are inserted into the ends of the channels, and an external optical excitation/detection system is used. Further reductions in cost and size can be realized by integrating the functional components (such as electrodes, sensors, pumps, valves, etc) into the micromachined channels. Extensive research has been carried out to this end using silicon, glass, and quarts

as substrates. These materials have been chosen as substrates because they are compatible with existing methods of microfabrication. Examples of integrated functional components in silicon/glass substrates include fluorescence detection [2, 3], heaters and resistive temperature detectors [4, 5], pumps [5, 6], and valves [7].

Although the above silicon, glass, and quartz based microfluidic devices are fabricated with the same techniques used for other MEMS and microelectronic devices, there are some fundamental differences. Microfluidic systems are often much larger than their microelectronic cousins, due to fundamental differences between manipulating large molecules versus electrons. For example, capillary electrophoresis channels are typically at least several millimeters long, whereas transistors can be in the range of a few tens of nanometers. As the size of the devices increase, the number of devices which can be batch fabricated simultaneously decreases. Therefore, the cost of the substrate and the processing steps becomes much more significant, since the cost of the run is divided between fewer devices. Unlike microelectronic devices, many microfluidic devices must be thoroughly cleaned between uses, which can be very difficult. In such cases, it is strongly desirable for the device to be disposable. However, making a device disposable severely limits the cost. This poses a dilemma for silicon/glass based microfluidic devices. The dilemma may be overcome by using a less expensive substrate material which is easier to process. Polymers are a promising candidate to meet this demand.

1.2 Microchannels in Polymers

There are a wide variety of polymers which have been used to fabricate microchannels, including poly(dimethylsiloxane) (PDMS) [8], polycarbonate (PC) [9], poly(methyl methacrylate) (PMMA) [10, 11], polyimide (PI) [12], poly(p-xylylene) (paralyne) [13, 14], polyolefins [15], polycaprolactone (PCL) [16], and epoxy [17, 18]. A variety of photo-curing polymers have been used to create microchannels [19]. Etching of copper coated printed circuit boards has also been used to fabricate microchannels [20, 21].

Although many methods of fabricating microchannels have been reported, they can all be divided into two general categories: direct micromachining techniques and replication techniques. Direct micromachining requires each channel to be micromachined, whereas a replication technique uses micromachining to generate a single mold, which is copied many times to produce channels without individual micromachining. Replication techniques are generally much less expensive than direct micromachining, and can only be done with polymers. Reported techniques for direct micromachining include surface micromachining [13], micro stereo lithography (MSL) [22, 23], bulk plasma etching [9], and laser ablation [24]. However, these techniques have not found significant commercial applications in microfluidics due to their high cost. Replication techniques can be divided into three categories: casting, hot embossing, and injection molding. A thorough discussion of replication techniques can be found in [25], and is summarized here.

Casting: A polymer in liquid form is poured into a mold, where it is solidified. Casting requires cycle times of minutes to hours, and has been used primarily for academic applications with PDMS [8] and epoxy [17]. Casting

has also been reported for other polymers, including Teflon [26].

Injection molding: A molten polymer is injected into an evacuated mold, where it is cooled until solid and then ejected. Injection molding allows cycle times of a few seconds to 3 minutes, and has been the most widely commercialized method of generating microchannels [10, 15]. Injection molding has already been developed extensively for generating nanometer scale features extremely inexpensively, so it is by far the most promising method of making inexpensive microfluidic devices. Compact discs, which are used to store audio (CD), data (CD-ROM), and video (DVD), have become household items which cost very little to manufacture. All of these storage devices consist of polycarbonate disks which are injection molded to form nano-sized pits and grooves which represent the digital data. These pits and grooves have a minimum size of 830 nanometers and spacing of 1.6 microns for CD and CD-ROM, and a minimum size of 400 nanometers and spacing of 740 nanometers for DVD [27]. The same equipment and techniques can be used to fabricate microchannels with the same accuracy and cost by simply changing the mold insert.

Hot embossing: A thermoplastic polymer is heated above its glass transition temperature, pressed against a mold, and cooled below the glass transition temperature before separating the polymer from the mold. A suitable polymer must have a glass transition temperature above the desired service temperature of the device, but well below the melt temperature or decomposition temperature of the polymer. Polycarbonate and PMMA are the most commonly used polymers for hot embossing. Hot embossing allows cycle times of 3-10 minutes, and has found some commercial applications in generating

microchannels [9]. Hot embossing equipment and molds can be obtained much less expensively than injection molding equipment and molds, so hot embossing is reported much more frequently in the literature than injection molding. However, components produced by hot embossing can generally be produced by injection molding without any significant changes. Therefore, hot embossing is a good method for developing processes which can be made commercially by injection molding.

Once an open polymer microchannel has been replicated, it must be sealed to form a microfluidic device. This can be accomplished by adhesives, thermal bonding, lamination, plasma treatment, or localized bonding.

Adhesives: Adhesives with a low viscosity can be applied as a thin coating to bond a wafer with microchannels to another wafer, creating a sealed device [20, 21, 28]. The adhesive can be epoxy or other compounds, and in some cases may be diluted with a solvent to reduce viscosity.

Lamination: A thin polymer film (approximately 0.001 inches thick) with a heat activated adhesive is pressed onto the surface of the microchannel wafer [29]. This process is very similar to the macroscopic lamination of paper products.

Thermal Bonding: Two pieces of plastic (one or both of which contain microchannels) are pressed together and heated close to the glass transition temperature. This has been most commonly reported for PMMA and polycarbonate [30, 31].

Plasma Treatment: This method of sealing microfluidic systems has only been reported for PDMS [8]. The PDMS surface to be bonded is exposed to

oxygen plasma, which activates surface functional groups and allows for siloxane (Si-O-Si) bonds when brought into contact with another suitable surface, such as PDMS, glass, or silicon. Bonding of PDMS to a few other polymers has also been reported [8].

Localized Bonding: Several methods have been reported for bonding a very localized area, rather than an entire wafer. These include the use of lasers [32] and lithographically patterned heaters [33].

The first three methods can significantly change channel geometries; the degree of change depends on materials and process parameters. Unfortunately, the literature lacks any thorough characterization of these methods.

1.3 Integrated Polymer Microfluidic Systems

Once a sealed microchannel has been fabricated, it may be filled with fluid and manipulated externally. However, to fully realize the cost and size benefits of a microsystem, it may be desirable to integrate the functional components into the microfluidic device. The most basic integrated functionality is patterned metal layers, which may form electrodes, heaters, resistive temperature sensors, etc. There are two common methods of generating a patterned metal layer: lift-off and direct patterning of a deposited layer. In the former method, photoresist is spun directly onto the substrate and lithographically patterned (generating the 'shadow mask'). The desired metal is evaporated, but does not coat the side wall of the patterned resist due to the highly directional nature of evaporation. Finally, the resist is removed, washing away the unwanted metal regions and leaving the desired pattern. The latter method starts with depositing the desired metal directly on the substrate. Photoresist is applied to the metal layer and

lithographically patterned, generating a mask for metal etching. Finally, the photoresist is removed.

Photoresist itself is composed of a polymer (usually a Novalak resin) and solvent to keep it in liquid form. These solvents can damage some of the plastics used in microfluidics, including PMMA and polycarbonate. Two types of damage may occur, depending on the solubility parameter(s) of the particular solvent and polymer: the polymer surface may dissolve, or it may swell. A solvent which dissolves the polymer is unacceptable for the lift-off process, but may be used for patterning on top of a deposited metal layer if the metal layer provides a sufficient barrier. If the metal layer is thin enough or porous enough not to provide a sufficient barrier, than no solvents which dissolve or swell the polymer surface may be applied. A solvent which swells the polymer can be used for lift-off if there are no pre-existing metal features on the substrate. However, pre-existing metal features may be destroyed if the surface of the polymer substrate swells around or under the features. All commercially available photoresist from the major U.S. manufactures (Shipley and Clariant) contain solvents which affect the PC surface.

Lift-off has been performed on PMMA to form electrodes [11, 34]. In both cases, there were no features on the polymer wafer before application of the resist. In [34], it is stated that the resist used does not contain any solvents which would dissolve PMMA. The name of the resist manufacturer is given, but the company is German and no further information can be obtained. In [11], no mention is made of the resist used. Screen printing, electroless deposition, and direct lithography on deposited metal layers have been investigated by Aclara for the purpose of forming electrodes [15]; however, no details are given.

Polyimide (which is not affected by most solvents when cured) has been used as a substrate for directly patterning a sputtered titanium/platinum or copper layer to form electrodes and heaters [12, 35]. This device was fabricated with a direct micromachining process, and illustrates the difficulties associated with this type of process. First, a sacrificial layer of chromium and aluminum is evaporated on a carrier wafer (which will not be part of the final device). A layer of photosensitive polyimide is spun on 5 to 20 microns thick and lithographically patterned. A layer of titanium and platinum is evaporated and lithographically patterned to form electrodes. Another layer of photosensitive polyimide is spun on and lithographically patterned to form the channel walls. On a second carrier wafer, a sheet of Mylar is placed on the surface, followed by spin coating of a 5 to 20 micron layer of photodefinable polyimide. The two polyimide surfaces are bonded, and the Mylar film/top carrier wafer is removed. The top layer of polyimide is lithographically patterned, and the three layer polyimide structure is released from the bottom carrier wafer by etching the sacrificial bottom layer of aluminum. This process requires two evaporation steps, four spin coatings, four lithography steps, bonding, and sacrificial release. The number of steps required for fabrication will make the cost of this type of device similar to that of silicon and glass based systems, thereby negating much of the advantage of a polymer device.

Electrodes are only one very small step in creating integrated polymer microfluidic systems. A complete system may require valves, pumps, sensors, etc. Some limited work has been done to this end. PMMA valves have been demonstrated using a CNC milling machine [36], and hot embossing [35]. The latter method employed two embossed PMMA wafers which are bonded together

with a polyimide membrane between them. The polyimide membrane contains the lithographically patterned titanium or copper layer which forms heaters for actuating the valve. Direct micromachining on printed circuit boards (PCB) has produced a variety of components including a pH regulation system [37], pump [38], bubble sensor, and flow sensor [39]. In these devices, the channels are etched in the copper layer of the PCB and epoxy is used to attach a cover plate for sealing the channels. Beebe has demonstrated several types of autonomous valves, based on hydrogels, which actuate in response to fluid conditions [19].

1.4 Motivation for Further Research

To fully realize the cost, size, and performance benefits of a microsystem, it may be desirable to integrate the functional components (pumps, valves, detectors, heater, electrodes, etc.) within the microsystem. The present techniques for producing integrated microfluidic systems are too costly for many applications because of their reliance on expensive substrates and/or multiple microfabrication steps to produce a simple channel. Polymer replication techniques, especially injection molding, offer a means of very inexpensively producing microfluidic devices. The techniques for accurately and cheaply producing nanometer scale feature in polycarbonate have been extensively developed and commercialized through the compact disc industry. However, electrodes are the only integrated functional components which have been demonstrated in a hot embossed or injection molded microfluidic system. In order to realize the goal of inexpensive integrated systems, more techniques for integrating functional components in hot embossed/injection molded microfluidic systems must be developed. Polycarbonate and PMMA are the most commonly used polymers for hot emboss-

ing/injection molding, so these new integration methods should be compatible with PMMA and PC.

As mentioned previously, working with PC or PMMA has two major drawbacks:

Chemical limitations: Most organic solvents used in microfabrication will either dissolve polycarbonate or cause surface swelling. Either of these phenomena will damage any existing metal layers, due in part to the poor adhesion between metals and polymers. Theoretically, any metal layer would protect the surface of the plastic, but in practice, metal layers are usually not perfect. When the thickness of an evaporated metal layer is less than approximately 1000 Angstroms, the porosity becomes sufficient to allow solvent penetration and hence damage to the metal layer as the surface of the polymer changes and/or expands.

Temperature limitations: The glass transition temperature of PC is 150°C, at which point it can begin to flow and take the shape of anything it comes in contact with. Therefore, processing temperatures generally must be maintained below 150°C (except when flow is desired, i.e. embossing).

Therefore, a process must meet the above limitations to be compatible with PC or PMMA.

Many microfluidic applications require temperature control, including Polymerase Chain Reaction (PCR) [40], separation methods such as Temperature Gradient Capillary/Gel Electrophoresis (TGGE/TGCE) [41] and Temperature Gradient Focusing (TGF) [42], bubble pumps [43], gas sensors [44, 45], flow sensors [46, 47], etc. Some of these applications have been demonstrated by simply controlling the temperature of the whole substrate; others require controlling

the temperature of only a small region of the system. Even in the former cases, significant increases in performance and power consumption can be achieved by controlling the temperature in only a small region through the use of integrated heaters and temperature sensors.

Based on the preceding facts, it is clear that a need exists for the development of methods to integrate temperature control elements (heaters and temperature sensors) in low cost polymer microfluidic systems. Therefore, this work will address the need by presenting novel methods for the design and fabrication of low cost polymer microfluidic systems with integrated temperature control.

Chapter 2

Fabrication of Thermal Components in Polymer Microsystems

2.1 Deposition of Metal Thin-Films by Evaporation

2.1.1 Experimental Results

Aluminum, chromium, gold, and titanium have been deposited via evaporation onto polycarbonate (PC), poly(methyl methacrylate) (PMMA), and polystyrene (PS). Chromium and titanium were found to adhere to the substrates enough to allow lithographic patterning. These metals were used as adhesion layers for thicker gold layers. The thickness ranges used were 100 Å to 1000 Å for chromium and titanium, and 1200 Å to 5000 Å for gold.

The most important material properties for a Resistive Temperature Detector (RTD) are the room temperature resistivity (ρ_{rt}) and Thermal Coefficient of Resistivity (TCR or α). Table 2.1 gives bulk values for these material properties from the literature for several metals commonly used in electrical applications. Table 2.2 summarizes the bulk material property values measured for the thin films used in this study. The sheet resistance, $R_{\mathrm{s}} = \rho/t$, was measured using a four point probe. The bulk resistivity values given in Table 2.2 were calculated based on the target thickness, t, of the metal film. The target thickness was used since there is no method available to us for measuring film

Material	ρ_{rt} (Ωm) $\times 10^{-9}$	α $(^{\circ}C^{-1})$ $\times 10^{-9}$	Source
Gold	24.4	0.34	[48]
Silver	15.9	0.41	[48]
Platinum	106	0.39	[48]
Chromium	130	0.214	[49]
Titanium	420	0.38	[49]

Table 2.1: Approximate values of room temperature resistivity, ρ_{rt}, and thermal coefficient of resistivity, α, for some metals.

thicknesses of several hundred angstroms. Therefore, some of the variations in Table 2.1 may be due to variations in thickness. The TCR values were obtained by heating the substrate with a thermocouple attached. The normalized change in resistance $\Delta R/R_{RT}$ is plotted versus temperature, and the slope of the resulting line is the TCR value. For chromium and titanium films, the overlying gold layer was removed before measuring resistivity and TCR. For gold films, the underlying adhesion layer was removed before measuring resistivity. When measuring the TCR of gold films, the adhesion layer was not removed. Normally, the sheet resistance of the gold layer is much lower than the sheet resistance of the adhesion layer, making the effect of the adhesion layer negligible. However, two fabricated devices were evaluated in which the gold layers appeared to have significantly higher resistivities and lower TCR values than previous tests. These values are reflected in Table 2.2. The apparent deviant material properties could be a result of the actual gold properties, the thickness of the gold layer, or both. The wafers were already patterned and bonded, so no four-point measurements or other investigations could be performed.

	ρ_{rt} (Ωm) $\times 10^9$				α $(^\circ C^{-1})$ $\times 10^2$			
	Mean	Range	σ	Wafers	Mean	Range	σ	Wafers
Au	72	26-135	73%	3	0.22	0.17-0.30	33%	3
Ti	1397	841-2654	42%	14	0.18	0.17-0.18		2
Cr	2375	1985-2741	13%	5	0.048	0.040-0.054	12%	4

Table 2.2: Measured values of room temperature resistivity, ρ_{rt}, and thermal coefficient of resistivity, α, for the thin films used in this study. For each material property, the mean value, maximum and minimum value, standard deviation, and number of wafers tested is given. The standard deviation, σ, is given as a percentage of the mean value.

One notable problem was observed: 1000 Å thick layers of chromium emerged from deposition with a hazy appearance. Under $400x$ magnification, it is evident that the haziness is caused by a fine crazing of the metal, shown in Figure 2.1. Upon removal of the metal layer, the same damage pattern is visible in the polymer substrate itself. This phenomena was observed in two separate runs in which 1000 Å chromium layers were attempted. On the other hand, thinner layers of chromium appeared normal. Furthermore, 1000 Å layers of titanium did not suffer this problem, and even more surprisingly, 5000 Å layers of gold were deposited many times without encountering this problem. One possible explanation for this phenomena is heating of the substrate during the deposition process. When the shutter opens, exposing the wafer to the evaporant, the substrate surface is still at room temperature. Therefore, the first part of the film is deposited on a room temperature surface. As deposition continues, the surface of the substrate begins to heat up and expand more than the metal film, due to the

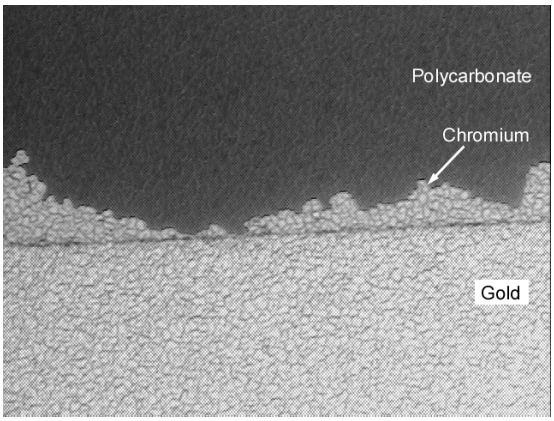

Figure 2.1: Crazing of thin film metal layers during evaporation. 1000 Å chromium followed by 5000 Å of gold were deposited. The lower region is chromium/gold, while the upper region is bare PC after metal removal with etchants. Some chromium is visible in the center. The metal was partially removed by placing a drop of etchant on the surface, avoiding the use of photoresist.

polymer's higher coefficient of thermal expansion (CTE). If the temperature rise and resulting expansion is great enough, it may tear the lowest part of the metal film. The upper layers are now deposited on an elevated temperature surface. When the substrate cools after deposition, the opposite phenomena may occur, i.e. the upper part of the metal film will be put under compressive stress and may buckle. If this is in fact the cause of the problem, it raises two questions: First, why does deposition of some metals (chromium) cause failure of the film much sooner than other metals (especially gold)? Second, what may be done to reduce or eliminate the problem? After offering a potential explanation to the first question, the second question will be revisited at the end of this section.

Differences in strength between different thin films may influence whether a evaporated metal film will exhibit crazing. The ultimate strength of a thin film

is highly dependent on both the micro structure of the film and the material. The microstructure will vary greatly depending on deposition conditions. As a result, any literature data pertaining to thin films of chromium, titanium, or gold would be difficult to apply without performing mechanical tests. However, it is possible to make some predictions as to what the temperature rise will be when depositing a given material. Once again, the final answer depends on material properties which are not easily measurable; In this case they may be approximated using readily available handbook data. Doing so will make it difficult to predict the exact temperature rise, but may still show significant differences between materials.

2.1.2 Thermal Phenomena During Metal Deposition

A very simple model of the substrate is considered. The substrate is clipped firmly against a water cooled stainless steel chuck during e-beam evaporation, which can be approximated as a room temperature boundary condition. The source is over two feet away from the 10 cm diameter substrate, so variations in heat flux over the surface of the substrate are neglected. Therefore, a one-dimensional model is used, with a room temperature boundary condition on one side and prescribed heat flux on the other side. The surface heat flux is denoted q''_{w}, with units of $\mathrm{W/m^2}$. The temperature rise at the deposition surface of the substrate is

$$\Delta T_{\mathrm{w}} = \frac{t}{k} q''_{\mathrm{w}}, \tag{2.1}$$

where t is the thickness of the substrate and k is the thermal conductivity of the polymer. This assumes equilibrium has been achieved, which is infact the case for the depositions performed. A transient model is presented in Section 3.3.4

and is summarized here. Equation 3.60 predicts the percentage of equilibrium achieved after time t. It is found that the 1/16" polycarbonate wafers used in this study achieve 95% of thermal equilibrium in 24 seconds. The deposition rates used are 5-7 Å/sec for chromium and titanium, and 10 Å/sec for gold. Therefore, equilibrium will be achieved after 120-168 Å of chromium or titanium are deposited, and after 240 Å of gold are deposited.

Source Temperature

The heat flux reaching the wafer surface will be a function of the source temperature, which is in turn a function of the material being evaporated and the desired deposition rate. A few facts from the kinetic theory of gases [50] are relevant. First, the mean velocity, $\bar{v}$, of atoms or molecules in a gas is

$$\bar{v} = \sqrt{\frac{8000RT}{\pi m}} \tag{2.2}$$

where R is the universal gas constant (8.3145 J mol^{-1} K^{-1}), T is the temperature of the gas, and m is the atomic (molecular) mass of the gas species. The atomic (molecular) flux, or number of gas atoms (molecules) crossing a unit area per second, is denoted $\dot{N}$ and is given by

$$\dot{N} = \frac{n_v \bar{v}}{4} \tag{2.3}$$

where n_v is the atomic or molecular density (number of atoms or molecules per unit volume). For an ideal gas n_v is found by rearranging the ideal gas law:

$$n_v = \frac{PN_{\mathrm{A}}}{RT} \tag{2.4}$$

where P is the pressure and N_{A} is Avogadro's number (6.022×10^{23} atoms or molecules per mole). Combining Equations 2.2-2.4, the atomic (molecular) flux

can be written

$$\dot{N} = \sqrt{\frac{500 N_{\mathrm{A}}^2}{\pi m R T}} P \tag{2.5}$$

Equation 2.5 applies to any ideal gas.

A crucible, with radius r_{s}, containing a liquid metal undergoing evaporation is now considered. The total number of atoms leaving the source per second is $N_{\mathrm{s}} = \pi r_{\mathrm{s}}^2 \dot{N}_{\mathrm{s}}$. Assuming the atomic flux is uniform in all directions, the departing atoms will uniformly cover a hemisphere with surface area $2\pi d^2$, where d is the distance from the source to the wafer. Therefore, the atomic flux arriving at the wafer surface is

$$\dot{N}_{\mathrm{w}} = \frac{\dot{N}_{\mathrm{s}}}{2} \left(\frac{r_{\mathrm{s}}}{d}\right)^2 = \sqrt{\frac{125 N_{\mathrm{A}}^2}{\pi m R T_{\mathrm{s}}}} \left(\frac{r_{\mathrm{s}}}{d}\right)^2 P_{\mathrm{s}} \tag{2.6}$$

where T_{s} is the liquid metal temperature and P_{s} is the vapor pressure at the surface of the liquid (not the chamber pressure). The atomic flux arriving at the wafer is related to the deposition rate, v_d, by

$$\dot{N}_{\mathrm{w}} = 1000 \frac{\rho \, v_d N_{\mathrm{A}}}{m} \tag{2.7}$$

Combining Equations 2.6 and 2.7, an expression is found relating vapor pressure and temperature required for a desired deposition rate:

$$P_{\mathrm{s}} = \sqrt{8000\pi} \rho v_d \sqrt{\frac{R T_{\mathrm{s}}}{m}} \left(\frac{d}{r_{\mathrm{s}}}\right)^2 \tag{2.8}$$

In order to determine the source temperature for a given material, the relationship between temperature and vapor pressure for that material must be known. Such relationships have been empirically determined, and are presented in handbooks [51] as curve fit equations of the form

$$\ln(0.0075 P_{\mathrm{s}}) = -\frac{A}{T_{\mathrm{s}}} + B + C \ln T_{\mathrm{s}} \tag{2.9}$$

Material	A	B	C	Temp. Range (K)
Chromium	20680	14.56	-1.31	298-m.p.
Gold	19280	12.38	-1.01	1336-3240
Titanium	23200	11.74	-0.66	m.p.-b.p.

Table 2.3: Coefficients of vapor pressure - temperature relationship for metals, $\ln(0.0075p) = -\frac{A}{T} + B + C \ln T$. Melting point is abbreviated m.p. and boiling point is abbreviated b.p.

where P_s is given in units of Pa. The coefficients for chromium, gold, and titanium are given in Table 2.3. Equations 2.8 and 2.9 may be combined and solved numerically for the source temperature, given the deposition rate and metal property values. There are two modes of heat transfer from the source to the substrate during evaporation:

Direct Heat Transfer

As high temperature metal atoms contact the surface of the substrate, they transfer thermal energy to the substrate. The thermal energy transfered in this manor has two components:

- Average kinetic energy, which is denoted q''_K, is given by

$$q''_K = \rho c_p \Delta T v_d, \tag{2.10}$$

  where ρ and c_p are the density and specific heat capacity, respectively, of the metal being deposited.

- Latent heat of fusion, L_f, and latent heat of condensation L_c, (or latent heat of sublimation, L_s). Energy is released as the gas phase metal atoms

form more stable (and lower energy) crystal stuctures. This heat flux is given by:

$$q''_{\mathrm{L}} = 1000 \rho m L v_d \tag{2.11}$$

where $L = L_c + L_f$ (or if sublimation occurs, $L = L_s$), and m is the atomic mass.

Radiation

Radiation heat transfer occurs due to the exchange of infrared and visible electromagnetic radiation between the source and substrate. The source is modeled as a circular area with temperature T_{s} and radius r_{s}, the wafer being coated is modeled as another circular area with temperature T_{w} and radius r_{w}, and the walls of the chamber are modeled as a room temperature surface connecting the two disks. This geometry is a complete enclosure with three surfaces, shown in Figure 2.2. All the surfaces are assumed to be coated with the metal being evaporated, and the emissivity is assumed to vary with temperature. Emissivity values are only available from the literature for temperatures up to approximately 1200 K, whereas the typical source temperatures for evaporation at 10^{-7} torr chamber pressure and 10-20 Å/sec range from 1700 K to 2300 K. Extrapolation is used to estimate the emissivities at higher temperatures by curve fitting the available data with a linear approximation, as shown in Figure 2.3. Titanium and gold both appear to have emissivity values which increase linearly, justifying a linear approximation. However, chromium increases much more rapidly than the linear approximation, so the extrapolated value will be significantly lower than the actual value. This fact must be remembered when interpreting the results. The use of extrapolation for any data set will significantly reduce the accuracy of the

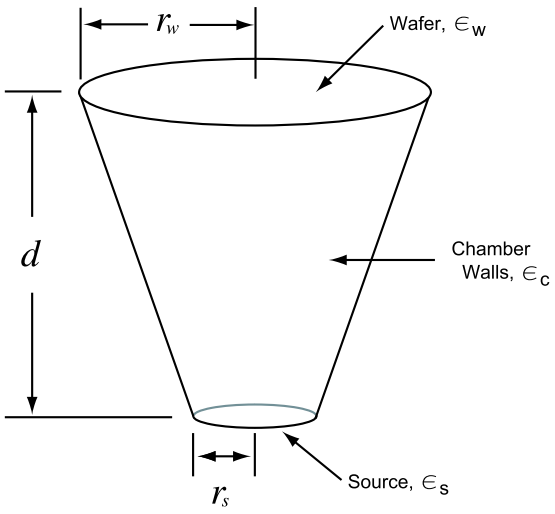

Figure 2.2: Geometry of model used to approximate radiation heat transfer during evaporation. The geometry forms an enclosure with three surfaces: the source is considered surface 1, the wafer is surface 2, and the chamber walls are surface 3.

results, but some conclusions may still be drawn. First, the emissivity increases with temperature. Second, chromium and titanium have a significantly higher emissivity than gold.

For an enclosure with N surfaces, the temperature of surface i is related to the radiation flux, J, leaving each of the other surfaces in the enclosure:

$$\frac{\epsilon_i}{1-\epsilon_i}(\sigma T_i^4 - J_i) = \sum_{j=1}^{N} F_{ij}(J_i - J_j) \tag{2.12}$$

where ϵ_i is the emissivity of surface i, and F_{ij} is the view factor, defined as the fraction of radiation leaving surface i which is intercepted by surface j. There are two helpful relations which can be used to determine unknown view factors

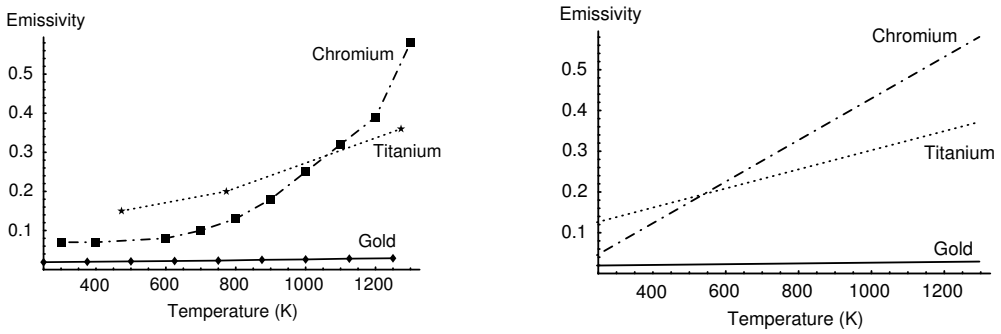

(a) (b)

Figure 2.3: Emissivity of gold, chromium, and titanium as a function of temperature. (a). Handbook data [52]. (b). Linear approximation of handbook data used in calculations.

from known ones:

$$A_i F_{ij} = A_j F_{ji} \qquad \text{and} \qquad \sum_{j=1}^{N} F_{ij} = 1 \tag{2.13}$$

The source, wafer, and chamber walls are considered to be surfaces 1, 2, and 3, respectively. The view factor between the source and wafer is found to be

$$F_{sw} = \frac{1}{2}\left(S - \sqrt{S^2 - 4\left(\frac{r_\mathrm{w}}{r_\mathrm{s}}\right)^2}\right) \tag{2.14}$$

$$S = \frac{r_\mathrm{s}^2 + r_\mathrm{w}^2 + d}{r_\mathrm{s}^2} \tag{2.15}$$

Equation 2.12 is written for each surface, using Equation 2.13:

$$\frac{\epsilon_\mathrm{s}}{1-\epsilon_\mathrm{s}}(\sigma T_\mathrm{s}^4 - J_\mathrm{s}) = F_\mathrm{sw}(J_\mathrm{s} - J_\mathrm{w}) + (1 - F_\mathrm{sw})(J_\mathrm{s} - J_\mathrm{c}) \tag{2.16a}$$

$$\frac{\epsilon_\mathrm{w}}{1-\epsilon_\mathrm{w}}(\sigma T_\mathrm{w}^4 - J_\mathrm{w}) = \left(\frac{r_\mathrm{s}}{r_\mathrm{w}}\right)^2 F_\mathrm{sw}(J_\mathrm{w} - J_\mathrm{s}) + (1 - \left(\frac{r_\mathrm{s}}{r_\mathrm{w}}\right)^2 F_\mathrm{sw})(J_\mathrm{w} - J_\mathrm{c}) \tag{2.16b}$$

$$\frac{\epsilon_\mathrm{c}}{1-\epsilon_\mathrm{c}}(\sigma T_\mathrm{c}^4 - J_\mathrm{c}) = \frac{r_\mathrm{s}^2}{C}(1 - F_\mathrm{sw})(J_3 - J_\mathrm{s}) + \frac{r_\mathrm{w}^2}{C}(1 - \left(\frac{r_\mathrm{s}}{r_\mathrm{w}}\right)^2 F_\mathrm{sw})(J_\mathrm{c} - J_\mathrm{w}) \tag{2.16c}$$

where

$$
\begin{aligned}
C &= \left(r_{\mathrm{w}}\sqrt{r_{\mathrm{w}}^2+h_{\mathrm{w}}^2}-r_{\mathrm{s}}\sqrt{r_{\mathrm{s}}^2+h_{\mathrm{s}}^2}\right)^2 \\
h_{\mathrm{s}} &= d\left(\frac{r_{\mathrm{s}}}{r_{\mathrm{w}}+r_{\mathrm{w}}}\right) \\
h_{\mathrm{s}} &= d\left(\frac{r_{\mathrm{w}}+2r_{\mathrm{s}}}{r_{\mathrm{w}}+r_{\mathrm{w}}}\right)
\end{aligned}
$$

Equations 2.16a-2.16c may be solved simultaneously for J_s, J_w, and J_c. The resulting expression for J_w is then used to find the radiation component of the wafer heat flux:

$$q''_{\mathrm{R}}(T_{\mathrm{w}}) = \frac{\epsilon_{\mathrm{w}}}{1-\epsilon_{\mathrm{w}}}(\sigma T_{\mathrm{w}}^4 - J_{\mathrm{w}}) \tag{2.17}$$

Note that Equation 2.17 is a function of the source, wafer, and chamber temperatures. The source and chamber temperatures are known, but the wafer temperature is still unknown.

Wafer Temperature

The total heat flux on the surface of the substrate is now the sum of Equations 2.10, 2.11, and 2.17, which may be combined with Equation 2.1:

$$q''_{\mathrm{w}}(T_{\mathrm{w}}) = q''_{\mathrm{K}} + q''_{\mathrm{L}} + q''_{\mathrm{R}}(T_{\mathrm{w}}) = k\frac{T_{\mathrm{w}}-T_{\mathrm{rt}}}{t} \tag{2.18}$$

The wafer temperature, T_{w}, is found by numerically solving Equation 2.18 for each combination of material properties and deposition rate. The resulting substrate temperatures are shown in Figure 2.4. The wafer temperature may then be used to find the heat flux applied to the wafer. Heat fluxes are shown in Table 2.4 for two different conditions. First, the chamber walls are assumed to be coated with the metal being deposited, hence possessing the same emissivity as the metal at room temperature. Second, the chamber walls are assumed to be black bodies,

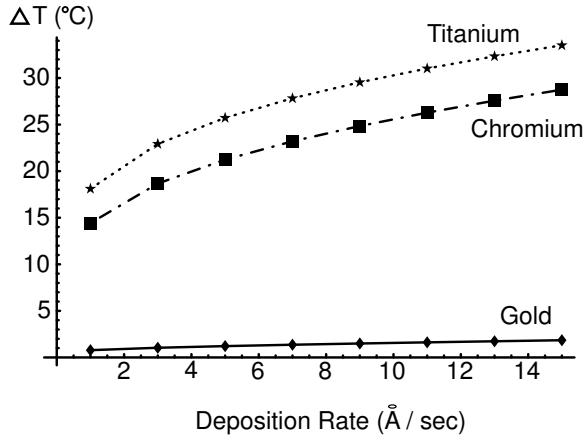

Figure 2.4: Estimated temperature rise of the polymer substrate surface during evaporative deposition.

with an emissivity of 1. Assuming black body walls reduces the heat flux reaching the wafer by 97% for chromium and titanium, which implies that most of the heat flux is due to radiation which is reflected around the chamber.

Conclusions

Figure 2.4 suggests that decreasing the deposition rate enough might avoid thermal problems at the substrate surface. However, lower deposition rates may lead to more contaminated metal layers, as can be seen from a comparison of impingement rates for air molecules and metal atoms. Equation 2.5 may be used to predict the flux of O_2 and N_2 molecules impacting the surface, while Equation 2.7 may be used to predict the flux of metal atoms impacting the surface. The ratio of these two values, shown in Figure 2.5 as a function of deposition rate, gives an idea of how significant oxidation and other contamination may be.

Several conclusions may be drawn from the preceding results.

	Metal-coated chamber			Black body chamber		
	Au	Ti	Cr	Au	Ti	Cr
Kinetic Energy	35	42	55	35	42	55
Latent Heat	4	5	6	4	5	6
Radiation	143	3369	2908	0.25	50	19
Total	182	3415	2969	39	97	79

Table 2.4: Substrate heat fluxes caused by evaporation for a deposition rate of 10 Å/sec. All values are in W/m^2

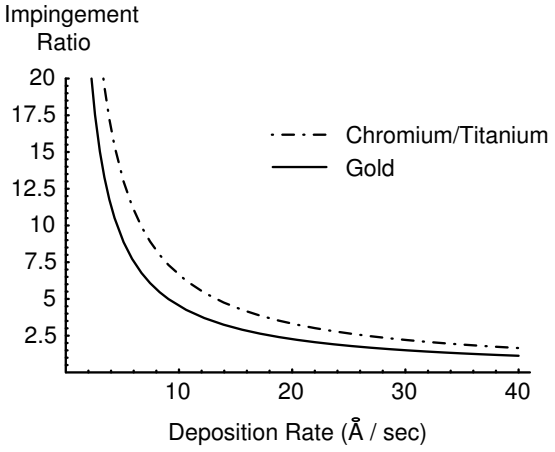

Figure 2.5: Ratio of air molecule impingements to metal atom impingements on the substrate surface as a function of deposition rate.

- As the source emissivity increases, the source becomes a better emitter of radiation (because it has the highest temperature in the system), and the wafer temperature increases. As the emissivity of the chamber walls increase, they become better radiation absorbers (because they have the lowest temperature of the system) and the temperature of the wafer decreases.

- The actual temperature rise during chromium deposition will probably be much higher than shown in Figure 2.4 because the approximated source emissivity is too low. This would make the temperature rise during chromium deposition the highest of the three metals studied, followed closely by titanium, while the temperature rise during gold deposition is much smaller. This agrees well with the observed trend: chromium films suffers problems during deposition most readily, while gold may be deposited in very thick layers without problems.

- Decreasing deposition rates may not be a reasonable method of reducing thermal problems, since it may result in contaminated films.

- Most of the substrate heating occurs due to radiation reflected from the chamber walls. This suggests that a very effective solution may be to use a series of baffles which absorb scattered radiation but do not get coated by the evaporating metal. This is feasible since the deposition is line of sight; that is the metal atoms do not bounce around the chamber, but generally deposit on the first surface they collide with.

2.2 Lithography on Polymer Substrates

A thin film metal layer must be patterned to generate a microheater or RTD. Many such techniques exist, some of which are capable of very high resolution (nano-scale) patterning. However, existing methods may not work when using injection moldable polymers as substrates, due to the temperature limitations and chemical susceptibility of commonly used polymers. An understanding of the chemical structure and solubility of the relevant polymers is important, as it may be necessary to modify some existing patterning techniques for use with PC and PMMA. A brief description of polymer solubility is provided here.

2.2.1 Solubility of Polymers

The microstructure of a polymer may be amorphous or crystalline, which will greatly affect its solubility. If a crystalline structure exists, then dissolving the polymer requires overcoming the latent heat of melting. This is often very difficult to accomplish with a solvent at room temperature, although it may become possible at elevated temperatures. Specific interaction between the chemical structures of the solvent and polymer may increase solubility of a polymer in a particular solvent. However, the polymers commonly used for injection molding are amorphous, so solubility of crystalline polymers will not be discussed in detail.

Solubility parameters may be used as a starting point for predicting the solubility of an amorphous polymer in a given solvent. The solubility parameter, δ with units of $\mathrm{Pa}^{1/2}$, is a measure of the intermolecular forces between molecules of a given chemical. A overall value (δ_t) may given, which measures the total strength of all intermolecular forces and is referred to as the Hildebrand para-

mater. Individual values for the strength of dispersion forces (δ_{d}), dipole forces (δ_{d}), and hydrogen bonding forces (δ_{d}) may also be given. These are referred to collectively as Hansen parameters, and provide a more accurate method of predicting solubility than the Hildebrand parameter alone. Unfortunately, Hansen parameters are only available for a limited number of solvents, and a much smaller number of polymers.

When two chemical species, A and B, are brought into contact, a solution will be formed only if the strength of the B-B inermolecular force is similar to the strength of the A-A intermolecular force. If the A-A intermolecular force is much greater than the B-B intermolecular force, than A molecules will be attracted much more strongly to other A molecules than B molecules, and the two remain separate. This fact may be roughly quantified by the following rule of thumb: solubility is predicted if the solubility parameters of the two species, δ_{A} and δ_{B}, are within approximately 2 $\mathrm{MPa}^{1/2}$ of each other. If the Hansen parameters are available for both species, then each component of the Hansen parameters may be treated as a coordinate in three-dimensional space. A point may be plotted for species A and a point may be plotted for species B; if the distance in three-dimensional space between these two points is less than approximately 2 $\mathrm{MPa}^{1/2}$, then solubility is predicted. This may be written mathematically as:

$$(\delta_{A\mathrm{d}} - \delta_{B\mathrm{d}})^2 + (\delta_{A\mathrm{p}} - \delta_{B\mathrm{p}})^2 + (\delta_{A\mathrm{h}} - \delta_{B\mathrm{h}})^2 \leq 2\mathrm{MPa}^{1/2} \tag{2.19}$$

for solubility to occur. If Hansen parameters are not available, then an estimate of the relative importance of polar and hydrogen bonds should be made based on the structure of the molecule. The Hildebrand parameter may then be used in conjunction with this estimate to predict the solubility of species A and B. Solubility parameter estimates from the literature are given in Tables 2.5- 2.7 for

Polymer	Hildebrand Parameter		Hansen Parameters		
	δ	Range	δ_d	δ_p	δ_h
PC	19.4	19.4-21.0	19.4	0.0	0.0
PMMA	19.5	17.8-23.1	15.6	10.5	5.2
PEI	21.5	19.0-23.0			
Novolak	22.5	21.5-22.5			

Table 2.5: Solubility parameters for selected polymers [53, 54]. The value shown for δ is the value considered to be most accurate. All values are in $MPa^{1/2}$

some polymers and solvents of interest. The chemical structures of some polymers used in this study are shown in Figure 2.6. The solubility parameter is an experimentally determined value which depends on the method and sample used to determine it, which is reflected in the range of values found in the literature for a given polymer or solvent. Therefore, the parameter ranges must be taken into account when predicting solubility. In some cases, the difference in Hildebrand parameter may be greater than 2.0 $MPa^{1/2}$ or less than 2.0 $MPa^{1/2}$ depending on which values are used within the given ranges. In such cases, solubility must be determined experimentally.

2.2.2 Pattern Transfer Methods

Given a thin-film metal layer, there are a variety of methods to pattern it.

Direct Writing

A energetic beam is used to expose certain areas of the wafer, thereby forming the desired pattern. The beam may be photons (i.e. laser), electrons,

Solvent	Hildebrand Parameter		Hansen Parameters		
	δ	Range	δ_{d}	δ_{p}	δ_{h}
amyl acetate	17.1	17.1-17.4	15.3	3.1	7.0
n-butyl acetate	17.8	17.3-17.8	14.5	7.8	6.8
o-xylene (1,2-dimethylbenzene)	18.5	17.9-18.5	17.0	7.5	0.0
m-xylene (1,3-dimethylbenzene)	18.2	18.0-18.3	16.5	7.2	2.4
p-xylene (1,4-dimethylbenzene)	18.1	17.9-18.1	16.5	7.0	2.0
anisole (methoxybenzene)	19.5	19.5-20.2	17.8	4.1	6.8
cyclopentanone	21.3	20.6-21.5	16.2	11.1	8.8
ethyl lactate	21.6	20.5-21.6	16.0	7.6	12.5
m-cresol (1,3-methylphenol)	22.7	20.9-22.7	18.0	5.1	12.9

Table 2.6: Solubility parameters for selected solvents [55, 54] commonly used in commercial photoresists. The value shown for δ is the value considered to be most accurate. All values are in $\mathrm{MPa}^{1/2}$

Material	Hildebrand Parameter		Hansen Parameters		
	δ	Range	δ_d	δ_p	δ_h
acetone	19.9	19.7-20.5	15.5	10.4	6.9
isopropanol (2-propanol)	23.5	23.4-23.9	15.8	6.1	16.4
methanol	29.7	29.2-30.7	11.6	13.0	24.0
water	47.9	47.5-48.0	12.2	31.2	34.1

Table 2.7: Solubility parameters for selected solvents [55, 54] commonly used in microfabrication. The value shown for δ is the value considered to be most accurate. All values are in $MPa^{1/2}$

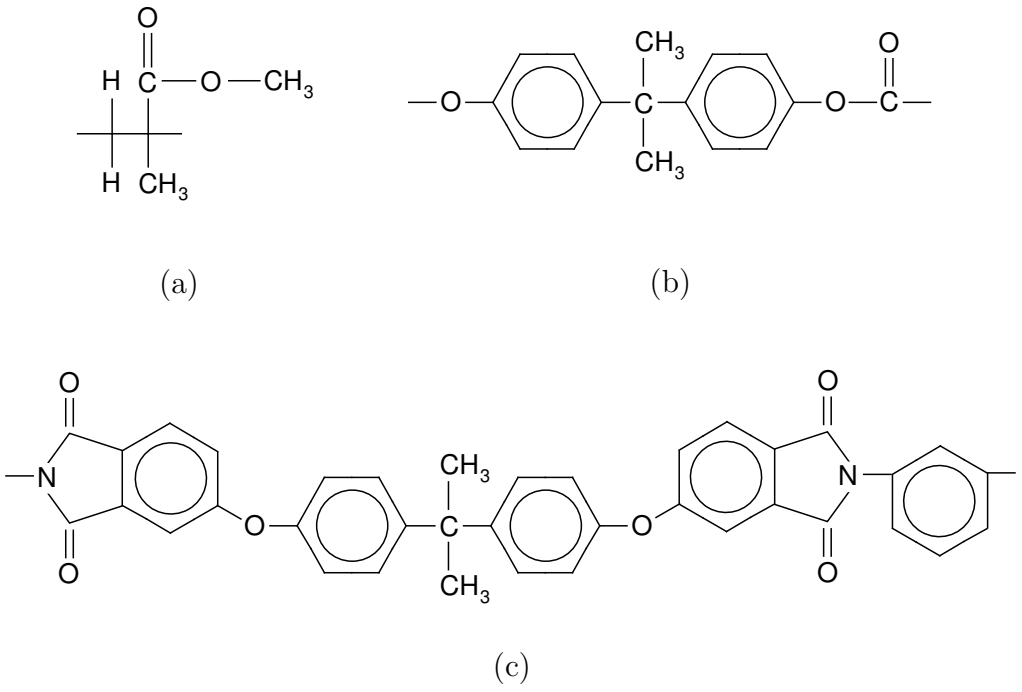

Figure 2.6: Chemical structures of the imprintable polymers used in this study. (a) Poly(methyl methacrylate). (b) Polycarbonate. (c) Polyetherimide.

ions, etc. The metal may either be burned off directly or another sacrificial layer (e.g. photoresist) may be deposited on top of the metal which is sensitive to the beam's energy. In the latter case, after patterning the sacrificial layer, the exposed metal is etched away. Although some direct writing techniques are capabale of extremely small feature sizes, direct writing is a serial process. A parallel process in which many features can be simultaneously patterned is much faster and cost efficient. Furthermore, such an energetic beam has a very high likelyhood of damaging a substrate polymer such as PMMA or PC. Infact, PMMA is often used as the sacrifical layer with electron beam lithography.

Micro-Contact Printing

Micro-contact printing, or μCP, is a recently developed technique which utilizes a Self Assembled Monolayer (SAM) to pattern certain materials including gold, silicon, silicon dioxide, copper, and silver [56]. These materials may then be used as a sacrificial layer to pattern other layers. A PDMS stamp containing the desired pattern is coated with an "ink" (alkanethiol for gold) and brought into contact with the substrate to be patterned. The "ink" transfers to the substrate, forming a SAM on the substrate surface. This patterned monolayer protects the desired regions of the underlying film when exposed to a selective etchant, allowing the transfer of the pattern to the film. The SAMs deposited in this method are far from perfect. The best film reported contained 9,000 holes per cm^2. However, polymer surfaces are often significantly rougher than the silicon/gold surfaces used in this study, so it would be reasonable to expect a higher density of defects when patterning SAMS on polymer surfaces. If this monolayer is used to pattern relatively thick films with an isotropic etchant,

then the final diameter of the hole will be approximately twice the thickness of the film. For the 0.5 μm gold films used in this work, the final heaters and sensors would be expected to contain well over 9,000 one μm holes per square centimeter, which is unacceptable for our purposes. Although this technique may hold significant promise for generating very small features in a parallel process, substantial development is still needed.

Photolithography

This is the most common and extensively developed method of patterning thin-films. A photosensitive polymer film (photoresist) is deposited, and exposed to ultraviolet radiation through a mask containing the desired pattern. After exposure, the resist is subjected to a developer which removes either the exposed resist (if the resist is positive) or unexposed resist (if the resist is negative). The key to using this technique with polymer substrates is the ability to apply and remove a polymer (photoresist) without damaging the substrate polymer. Positive photoresists are generally easier to work with and therefore are more common. A positive photoresists typically has three main components:

Resin: This is often based on novolak resin (phenol formaldehyde), with a variety of proprietary modifications.

Sensitizer: Each resin molecule is attached to a sensitizer molecule, which is insoluble in water before exposure, but becomes water soluble after exposure and development.

Solvent: This makes the photoresist a liquid at room temperature, allowing application by spin or dip coating. Most of the solvent evaporates during

coating, and the remainder is removed by briefly heating the wafer before exposure (soft bake). Generally, two or more solvents are used to achieve the desired properties.

A photoresist which is to be used on a polymer substrate must contain a solvent which dissolves the resin/sensitizer yet does not dissolve or swell the substrate polymer.

2.2.3 Development of a PC Compatible Photoresist

Photolithography is efficient, capable of sub-micron feature sizes, and extensively used in industry, making it a very attractive method of patterning metal thin-films. However, all commercial photoresists contain solvents which dissolve or swell PMMA and PC. If the metal film is atop a polymer substrate, then swelling of the polymer will damage or destroy the metal film. If the metal film is continuous and sufficiently thick, then application of photoresist will not affect the underlying substrate. However, if the metal layer is already patterned or too thin, then it will be destroyed upon application of a commercial photoresist. To overcome this problem, a custom photoresist formulation has been developed which allows the use of standard lithographic patterning of thin metal films on PC and PMMA substrates.

As indicated previously, a PC/PMMA compatible photoresist must contain a solvent system which dissolves the resin without swelling or dissolving PC or PMMA. An appropriate solvent system may be chosen by considering the solubility parameters of the polymers. Referring to Table 2.5, PC and PMMA have similar Hildebrand parameters of 19.0 and 19.4 $MPa^{1/2}$, while novolak has a Hildebrand parameter of 22.5 $MPa^{1/2}$. To dissolve the novolak, the desired solvent

must have a Hildebrand parameter in range $20.5 \leq \delta \leq 24.5$ MPa$^{1/2}$. However, to prevent interaction with PC and PMMA, the solvent must have a Hildebrand parameter greater than 21.4 MPa$^{1/2}$. Therefore, an acceptable solvent must have Hildebrand parameter which satisfies $21.4 \leq \delta \leq 24.5$. Referring again to Table 2.6, there appear to be four possible solvents: n-butyl acetate, ethyl lactate, cresol, and isopropanol. N-butyl acetate is very close, and testing revealed that it did damage thin metal layers. A combination of ethyl lactate and isopropanol was chosen and determined to be an acceptable solvent system. Addition of too much isopropanol caused a white precipitate to form, indicating that some additive was no longer soluble. An ethyl lactate to isopropanol ratio of 5:8 was found to work well. The custom photoresist was prepared from commercial photoresist by evaporating off most of the solvent and redissolving with the desired solvents. A Clariant product (AZ 7905) based on ethyl lactate and n-butyl acetate was used as the starting resist. Based on the vapor pressures plotted in Figure 2.7, it is reasonable to assume the vapor pressure of n-butyl acetate is always higher than the vapor pressure of ethyl lactate, which means n-butyl acetate will evaporate more readily. Therefore, it is not necessary to evaporate off 100% of the solvent from the AZ 7905 resist to ensure the n-butyl acetate is removed. Figure 2.8 shows the effect of the unmodified AZ 7905 resist (which contains n-butyl acetate) on a thin chromium layer. After solvent replacement, the resist can be directly applied to thin chromium and titanium layers without damage, as shown in Figures 2.9 and 2.10, respectively. Figure 2.11 also shows good lithographic patterning with features as small as 8 μm on a PC substrate.

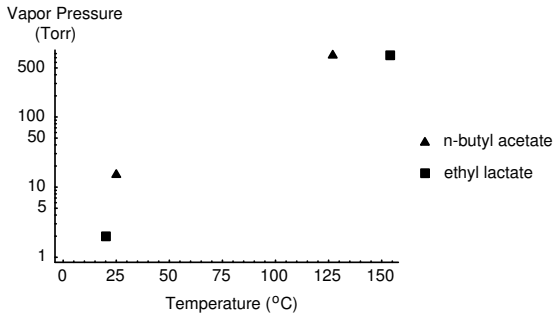

Figure 2.7: Plot of the vapor pressure and temperature for two known points: room temperature vapor pressure and boiling point.

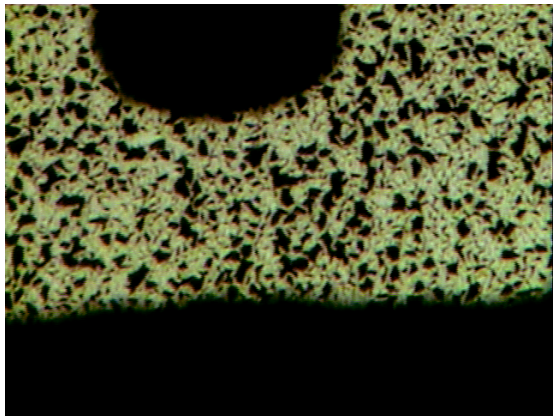

Figure 2.8: Damage to metal layer after exposure to photoresist. The metal is a 200 Å layer of chromium, and the resist used was AZ 7905 (Primary solvent is ethyl lactate with less than 5% n-butyl acetate. The line width is 50 μm.

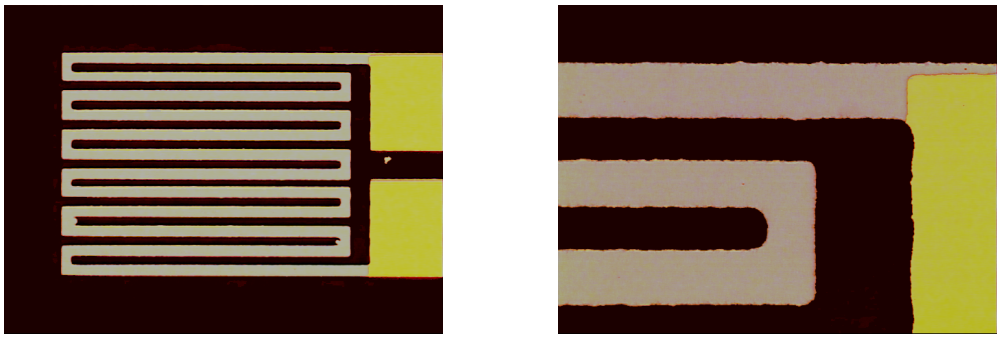

(a) (b)

Figure 2.9: Serpentine chromium sensor (200 Å) with gold leads (5000 Å). Segments are 50 μm wide. (a) Whole sensor (b) Enlargement of upper right corner where gold lead ends.

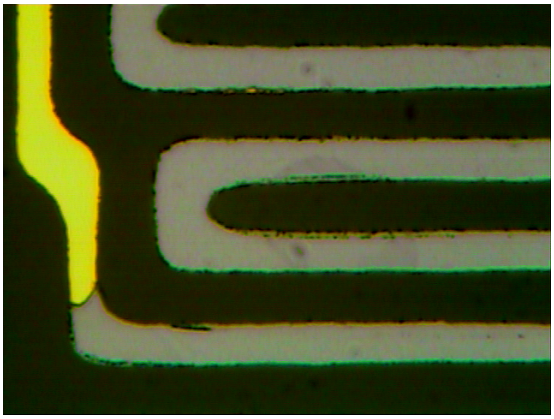

Figure 2.10: Serpentine titanium sensor (1000 Å) with gold leads (5000 Å). Segments are 8 μm wide.

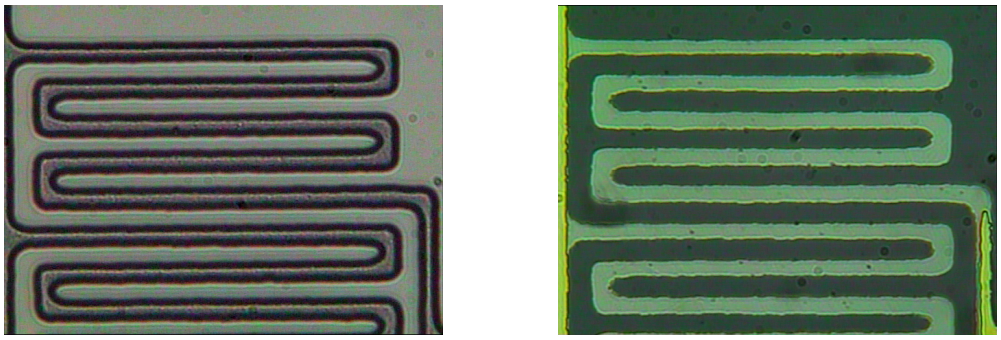

(a) (b)

Figure 2.11: Serpentine chromium sensor, 1000 Å thick with 8 μm wide segments. (a) Mask used to pattern sensor. (b) Completed sensor.

2.3 Microchannel Formation

Two methods are employed in this study for fabricating microchannels in polymers substrates. Hot embossing provides an economical method of fabricating large numbers of devices, while directly patterning SU-8 to form microchannels provides a simple method of prototyping.

2.3.1 Hot embossing

As discussed previously, this is a well established technique. In principle, this may be done with any polymer which exhibits a glass transition above room temperature. In practice, this becomes difficult for higher T_g materials. Qualitative predictions of glass transition behavior may be made by examining the chemical structure of the molecules. A polymer composed of "rigid" molecules which cannot rotate about their bonds will behave as an elastic solid. If the molecules can easily rotate about their bonds, then the polymer chains can easily rearrange themselves in response to a mechanical force, and the material may behave viscously. There is usually some amount of steric hindrance to rotation

about a bond. If large groups attached to the main chain collide during rotation, the energy required to overcome this steric hindrance greatly increases. This energy barrier to rotation may be overcome if the kinetic energy of the molecules is great enough, i.e. at a high enough temperature. However, there are several factors which will prevent a polymer from exhibiting a glass transition. Extensive cross linking will prevent molecules from rearrangement, regardless of kinetic energy. A crystalline structure will also inhibit rearrangement of the chains. Therefore, linear amorphous polymers are most likely to exhibit clear glass transitions. Polymers which contain double bonds or rings in their backbone will have higher T_g's than molecules which do not. This can be seen by comparing the structures and T_g of PMMA, PC, and PEI shown in Figures 2.6a-c. PMMA contains no rings or double bonds on the main chain, and has a relatively low T_g of 105°C. PC contains benzene rings in its backbone, but still has an -O-CO-O- linkage which allows rotation. It has an intermediate T_g of 150°C. PEI has both benzene rings and a compound ring structure in its backbone, with only an ether linkage (-O-) allowing rotation. Because the rings are so close, rotation causes the rings to collide and requires a substantial amount of energy to overcome. Therefore, PEI has a high T_g of 215 °C.

The embossing process used in this study is as follows:

- Substrate is off-gassed at 100°C overnight to dehydrate the polymer. If water vapor is present, it will be released during the hot embossing and cause bubbles in the wafer.

- Load the substrate into the press with the plattens 2°C above T_g. Note that at this point the wafer is still cold.

	Temperature (°C)			Pressure
	PMMA	PC	PEI	(MPa)
T_g	*105*	*150*	*215*	
Start	107	152	217	0
Heating	-	-	-	1.3
Press	115	160	225	1.7
Cooling	-	-	-	1.3
Release	98	143	208	0

Table 2.8: Hot embossing parameters for PC and PMMA

- Apply minimum pressure as the platens heat up to 10°C above T_g. This takes several minutes, allowing the wafer to reach T_g.
- Apply imprint pressure for 5-10 seconds.
- Apply minimum pressure as the plattens cool to 7°C below T_g.
- Release.

These parameters are summarized in Table 2.8.

Embossing Molds

The highest quality molds are generally metal, made with LIGA or similar processes, and quite expensive. Anisotropic etching of (100) silicon wafers is a commonly used alternative which is significantly less expensive. However, it has several disadvantages.

- The microchannel cross section is trapezoidal with sidewall angles of 54.7°.

Vertical sidewalls may be achieved with a different mask orientation, but corners become a problem.

- The microchannels must aligned with the <110> directions of the silicon wafer; misalignment will cause 'stepped' or jagged microchannel walls.

- Molds are time consuming to fabricate, due to the extra step of making an oxide mask, the chemicals often used (hydrofluoric acid and heated potasium hydroxide), and the long etch times (several hours) required for deep microchannels.

- Molds break frequently during embossing due to the severe mismatch of thermal expansion coefficients between the silicon (2×10^{-6} - 4×10^{-6} °C^{-1}) and polymer (65×10^{-6} - 90×10^{-6} °C^{-1} for PMMA and PC).

An alternative method is presented here utilizing patterned SU-8 as the mold. This method can eliminate most or all of the problems described above, and may be used for the embossing of PMMA and PC. The Coefficient of Thermal Expansion (CTE) for exposed SU-8 is 52×10^{-6} °C^{-1}, [57], which is close to that of PMMA and PC. Due to the high degree of cross-linking in exposed SU-8, the glass transition temperature is either very high or non-existent (greater than 200 °C). These properties make SU-8 an attractive material for an embossing mold. If an SU-8 mold is patterned on silicon, the mold will still be fragile, and the thermal mismatch between the SU-8 and silicon may shorten the life of the mold. These problems can be avoided by using an appropriate polymer as the substrate for the SU-8 mold. An ideal mold substrate should have a CTE similar to that of PC and PMMA, have a glass transition temperature higher than the material to be embossed, and form a strong bond with the SU-8. Polycarbonate

meets all of these requirements when used for embossing of PMMA. A strong bond between SU-8 and PC is achieved through the effect of the SU-8 solvent, cyclopentanone, and the polycarbonate. Referring to Table 2.5 and 2.6, the solubility parameters of SU-8 and PC indicate the possibility of solubility. Testing confirms that solubility does exist, allowing a strong solvent bond between the SU-8 and PC. Embossing of PC is accomplished using polyetherimide (PEI) as a substrate. Since PEI can not be dissolved by most common solvents at room temperature, the bond formed with SU-8 is weaker. Delamination is found to occur after 5 embossings. However, this still provides a simple and useful method for prototyping embossed microfluidic devices.

2.3.2 Patterned SU-8

Microchannels may also be formed by direct lithographic patterning of SU-8. If SU-8 is to be applied to a PMMA or PC substrate containing metal thin-films, the substrate must be protected. This is accomplished with vapor deposition of a parylene thin-film. Film thicknesses greater than 1 micron are found to adequately protect the substrate and metal layers. This method, although not viable for large scale production, is an attractive method of prototyping microfluidic systems. SU-8 microchannels patterned on polycarbonate are shown in Figure 2.12

2.4 Microchannel Sealing

The open microchannels formed by imprinting or patterning of SU-8 must be sealed to form a completed microfluidic system. This may be accomplished in several ways, three of which are used in this study: Bonding to a second wafer

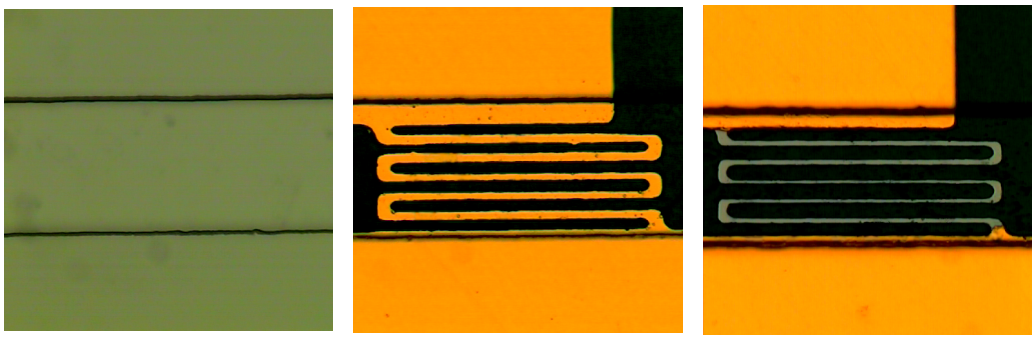

(a) (b) (c)

Figure 2.12: Microchannels patterned on parylene-coated polycarbonate. All channels are 140 μm wide and 40 μm deep. (a) Channel alone. (b) Channel over gold sensor 5000 Å thick, with a line width of 8 μm. (c) Channel over titanium sensor 1000 Å thick, with a line width of approximately 5 μm.

thermally or with adhesives, and laminating with a thin film.

2.4.1 Thermal Bonding

Thermal bonding, described earlier, is a commonly used method of sealing replicated microchannels. However, it requires heating the polymer near or slightly above its glass transition temperature. This has been found to destroy most thin-film metal layers present, possibly due to the severe mismatch in thermal expansion between the polymer and the metal. Figure 2.13 shows damage to a sensor after thermal bonding. Therefore, alternative bonding methods are required which do not affect thin-film components on the substrate surface.

2.4.2 Lamination

Lamination may be used in conjunction with patterned SU-8 microchannels, described in Section 2.3.2. A lamination film generally consists of two

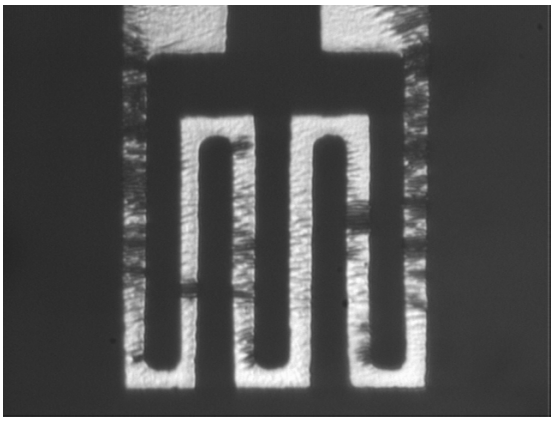

Figure 2.13: Damage to 200 Å chromium/5000 Å gold layer after thermal bonding.

polymers: an adhesive and a cover layer. The film is heated above the glass transition temperature of the adhesive layer and pressed onto the surface of the wafer. The softened adhesion layer bonds to the surface of the wafer, sealing the microchannels. Finally, localized areas of the film can be peeled off to provide access holes for fluid and electrical connections.

2.4.3 Adhesives

Most adhesives which form a strong bond do so by interacting with the surface of the polymer, and therefore can damage some thin-film metal layers. The metal layer may be protected by vapor deposition of a polymer such as parylene, followed by application of an adhesive such as epoxy. Alternatively, PDMS may be used as a thin film adhesive layer. PDMS does not contain solvents which affect polycarbonate, and can be cured at room temperature. Sylguard 184 (1 part curing agent to 10 parts elastomer) alone can be spin coated to a thickness of 10 microns, and when mixed with isopropanol (1 part curing agent,

10 parts elastomer, 10 parts isopropanol), it can be spin coated to a thickness of 2-3 microns. The PDMS layer is partially cured at 90 °C in an oven for 4.5 minutes followed by twenty minutes at room temperature. The two wafers are then brought into contact without pressure and allowed to cure for 24 hours at room temperature.

2.5 Temperature Sensing

There are a wide variety of methods for sensing temperature. They include

Density: The density change of a liquid or solid is measured, often by observing the relative expansion of two materials. Bi-metal strips and glass bulb thermometers are examples of instruments which utilize density changes.

Electrical: The change in electrical properties of a conductor or semiconductor is measured.

Pyrometry: The radiation spectrum emitted from a surface is measured and can be used to estimate the surface's temperature if the radiant properties of the surface are known. This method often has difficulty resolving small temperature differences, and therefore is most often used for high temperature applications where other methods are not practical.

Phase: Melting or crystalization may be used to indicated when a specific temperature is reached.

Fluorescence: The fluorescence intensity of some dyes varies substanially with temperature. Therefore, the fluorescence intensity of suitable dyes may be used to predict temperature.

PIV: Particle Image Velocimetry (PIV) is a method of determining the state (usually velocity) of a fluid from the motion of seed particles suspended in the fluid. However, the motion of the particles is also influenced by Brownian motion of the fluid, which is temperature dependent. Therefore, at low velocities temperature may be estimated based on PIV measurements of small seed particles [58].

Temperature measurements have been made in microfluidic systems using fluorescence [59] and PIV [58]. These non-contact methods have the advantage of high spatial and temporal resolution. If temperature control is desired, then measurements will have to be coupled with actuators (i.e. heaters) to create a closed loop system. Since the actuators and control system are generally electrical, the temperature measurement must be converted to an electrical signal. In the case of fluorescence or PIV, this requires optics, lasers, ccd cameras, and computers. A direct electrical method of measuring temperature in a microfluidic system is generally much simpler and less expensive than other methods, since it may be accomplished by measuring only voltage.

2.5.1 Electrical Temperature Sensors

There are three commonly used methods of sensing temperature electronically.

Thermocouple: Thermoelectric potential between dissimilar metals causes a voltage which is dependent on the temperature difference between two junctions. The sensitivity is only a function of material properties, and can not be changed by geometry. A thin film thermocouple requires depositing and patterning two different metals, plus an adhesion layer under one or both,

due to the generally poor adhesion between metals and polymers. Shorting of the two metal films by the adhesion layer would have to be prevented.

Resistive Temperature Detector: (RTD) The change in resistivity of a conductor as a function of temperature is measured. The sensitivity can be increased by material properties and geometry. RTD's can be more sensitive than thermocouples, depending on design.

Thermistor: The change in resistivity of a semiconductor as a function of temperature is measured. This is the most sensitive of the three types. However, depositing semiconductors on plastics such as polycarbonate is difficult due to the polymer's thermal and chemical limitations .

Due to the difficulties inherent in fabricating thermocouples and thermistors on a PC or PMMA substrate, RTD's are chosen for temperature measurement. The performance of an RTD may also be improved through design.

An RTD with high sensitivity that can measure temperature over a very small region is desired. To measure temperature over a small region with an RTD, the resistance must be very high at the point for which temperature measurement is desired and very low in the leads connecting the 'sensor' region to the bond pads. If the resistance in these leads is similar to the resistance of the 'sensor' region, then the measured change in resistance will be a complicated function of temperature at the desired point and everywhere else along the leads. This can be accomplished by making the leads much wider than the sensor region, but this approach severely limits how close together the sensors can be located (due to the bulky leads which tend to interfere with one another). Ideally, the sensor region should be composed of a thin layer of high resistivity material, while the

leads should be composed of a thick layer of low resistivity material. With this approach, the minimum spacing between sensors is not limited by large leads.

2.5.2 RTD Sensitivity

The sensitivity and accuracy of an RTD is a function of geometry, material properties, surrounding environment, measurement conditions, and calibration. To aid in the design of a highly sensitive RTD, an analysis of the design factors affecting sensitivity and accuracy of the RTD is performed. An RTD relies on the temperature dependence of the bulk resistivity of a material. For most metals, this change is approximately linear, especially over a small temperature range. This linear approximation may be expressed as:

$$\rho(T) = \rho_{rt}\left[1 + \alpha(T - T_{rt})\right] \tag{2.20}$$

where T_{rt} and ρ_{rt} are the room temperature and resistivity at T_{rt}, respectively. α is the temperature coefficient of resistivity, with units of $^{\circ}C^{-1}$. Handbook values for ρ_{rt} and α are given in Table 2.1 for some metals of interest. The change in resistance ΔR of a resistor due to a temperature change ΔT is:

$$\Delta R = \frac{L}{A}\rho_{\mathrm{rt}}\alpha\Delta T \tag{2.21}$$

Resistance is generally measured by observing the voltage, V, across the resistor for a known (measured) current, I. If the current remains constant, Ohms law may be used to predict the voltage change due to a change in temperature:

$$\Delta V = I\Delta R = I\frac{L}{A}\rho_{\mathrm{rt}}\alpha\Delta T \tag{2.22}$$

The sensitivity may be defined as

$$\frac{\Delta V}{\Delta T} = I\frac{L}{A}\rho_{\mathbf{rt}}\alpha \tag{2.23}$$

The maximum current which can be used is limited by Joule heating of the sensor; high currents will heat the sensor, reducing its accuracy. A model is developed in Section 3.3 which relates power applied to a heater and its temperature rise. It can be applied here as follows:

$$\Delta T_{\mathrm{J}} = \beta q'_{\max} = \beta I_{\max}^2 R = \beta I_{\max}^2 \frac{\rho(T_{\mathrm{op}})L}{A} \tag{2.24}$$

where ΔT_{J} is the maximum tolerable amount of Joule heating and T_{op} is the ambient temperature at which the sensor operates. Solving for $I_{\max}$ and substituting into Equation 2.23 yields

$$\frac{\Delta V}{\Delta T} = \sqrt{\frac{\Delta T_{\mathrm{J}} \rho_{\mathrm{rt}}}{\beta A \left[1 + \alpha(T_{\mathrm{op}} - T_{\mathrm{rt}})\right]}} L\alpha \tag{2.25}$$

It is clear from Equation 2.25 that the sensitivity may be increased by increasing the length or decreasing the cross-sectional area of the sensor. The length may be limited by space requirements, and the minimum line width is determined by the lithography system. Therefore, it is highly desirable to minimize the thickness of the sensor.

2.5.3 RTD Arrays

Measuring temperature distributions requires the use of multiple sensors, which can present design problems if the number of sensors is large. Interfacing with the outside world becomes increasingly difficult as the number of connections increases. High density interconnection solutions have been developed for VLSI chips, which are usually a couple square centimeters or less in size. However, microfluidic systems are generally much larger, which makes many of the existing high density interconnect products unusable. Therefore it is highly desirable to minimize the number of external electrical connections required. Contact

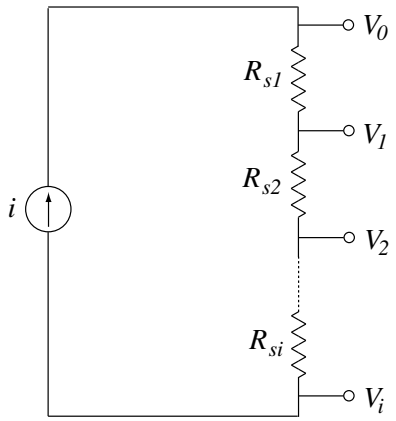

Figure 2.14: Circuit for measuring resistances of an array of sensors. A known current is applied while the voltage drop across each sensor is measured. Requires a minimum of $n + 3$ external connections, where n is the number of sensors.

resistance at the external interface is another significant problem when measuring sensor resistance. Such contact resistances can be large and unpredictable, so it is essential that the measuring circuit minimize or eliminate the effect of an unknown contact resistance.

The ideal method for measuring the resistance change of a sensor is with a four point or four wire technique, in which each sensor has one set of leads carrying a known current and a second set of leads used to measure the voltage drop across the sensor. For an array of n sensors, this requires $4n$ leads, which is often too many. The number of leads may be reduced to $n + 3$ if the sensors are all wired in series with the same known current passing through all of them. This type of circuit is illustrated in Figure 2.14. The disadvantage to this circuit is that if one sensor is broken during fabrication or use, the entire array becomes useless.

A wheatstone bridge circuit provides another means of measuring re-

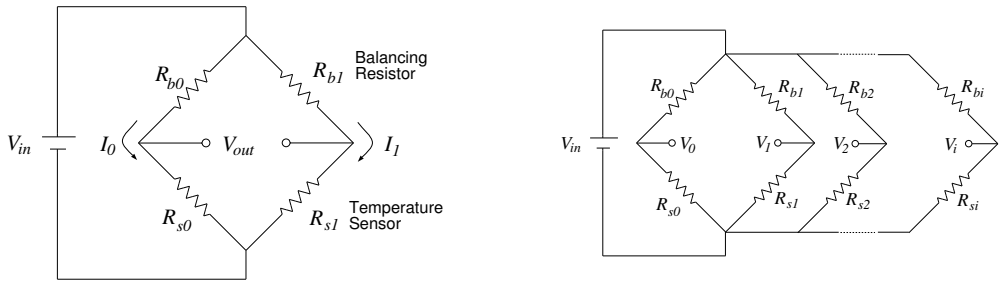

(a) (b)

Figure 2.15: Wheatstone bridge circuits. (a) Wheatstone bridge with single sensor. (b) Wheatstone bridge with multiple sensors. Requires a minimum of $n + 2$ external connections, where n is the number of sensors.

sistance, and is especially useful when measuring small changes in resistance. A simple wheatstone bridge circuit is shown in Figure 2.15a, and contains a sensor resistor (R_{s1}), a balancing resistor (R_{b1}), and a reference leg (R_{s0} and R_{s0}). If the balancing resistor and reference bridge have fixed resistances, then the resistance of the sensor may be written

$$R_{\mathrm{s1}} = \frac{R_{\mathrm{s0}}V_{\mathrm{in}} + (R_{\mathrm{b0}} + R_{\mathrm{s0}})V_{\mathrm{out}}}{R_{\mathrm{b0}}V_{\mathrm{in}} - (R_{\mathrm{b0}} + R_{\mathrm{s0}})V_{\mathrm{out}}} R_{\mathrm{b1}} \tag{2.26}$$

If the change in resistance is small, then it may be readily calculated from the change in output voltage:

$$\Delta R_{\mathrm{s1}} = \frac{(R_{\mathrm{b1}} + R_{\mathrm{s1}})^2}{R_{\mathrm{b1}}} \frac{\Delta V_{\mathrm{out}}}{V_{\mathrm{in}}} \tag{2.27}$$

where the value of R_{s1} may be approximated as the room temperature value.

A wheatstone bridge for a thin-film RTD may be fabricated in two ways: with the balancing resistor and reference leg integrated into the wafer or with an external balancing resistor and reference leg. In the former case, contact resistance does not affect the measurements since only the output voltage is measured. However, calibration may become more difficult. The latter case

is only practical if the contact resistance is very stable, which is often not the case. The wheatstone bridge circuit can also be used for multiple sensors, as shown in Figure 2.15b. The sensors in this circuit are wired in parallel, so if one fails during fabrication or use, the remaining sensors are unaffected. However, if the balancing resistors and reference leg are integrated onto the wafer, then calibration becomes substantially more complicated. Calibration of a temperature sensor generally involves heating the sensor to a known temperature and measuring the output. Knowing the temperature requires placing another calibrated temperature detector (type E thermocouples are used here) close enough to the uncalibrated sensor that the two temperatures are the same. In the case of a thin film RTD integrated into a microfluidic system, this requires placing the thermocouple outside the wafer and maintaining the whole wafer at a uniform temperature. However, if the balancing resistors and reference leg change temperature (and resistance), then Equation 2.27 no longer holds and Equation 2.26 is no longer useful, since all the resistances are unknown. The resistances of all resistors must be measured simultaneously to calibrate a fully integrated wheatstone bridge. This may be accomplished with the circuit shown in Figure 2.16. For each sensor/balancing resistor pair ($R_{\mathrm{s}i}$ and $R_{\mathrm{b}i}$), an external resistor ($R_{\mathrm{k}i}$) with a known resistance is connected. Kirchoff's Law at the junction of each triplet of resistors can be written $i_{\mathrm{s}i} + i_{\mathrm{b}i} - i_{\mathrm{k}i} = 0$. This may be rewritten in terms of voltages as follows:

$$\frac{V_{\mathrm{s}} - V_i}{R_{\mathrm{s}i}} + \frac{V_{\mathrm{b}} - V_i}{R_{\mathrm{b}i}} - \frac{V_i}{R_{\mathrm{k}i}} = 0 \tag{2.28}$$

Equation 2.28 contains two unknowns, $R_{\mathrm{s}i}$ and $R_{\mathrm{b}i}$. To find these values, two linearly independent forms of Equation 2.28 must be written for each junction and solved simultaneously. This is accomplished by applying a non-zero V_{s} while

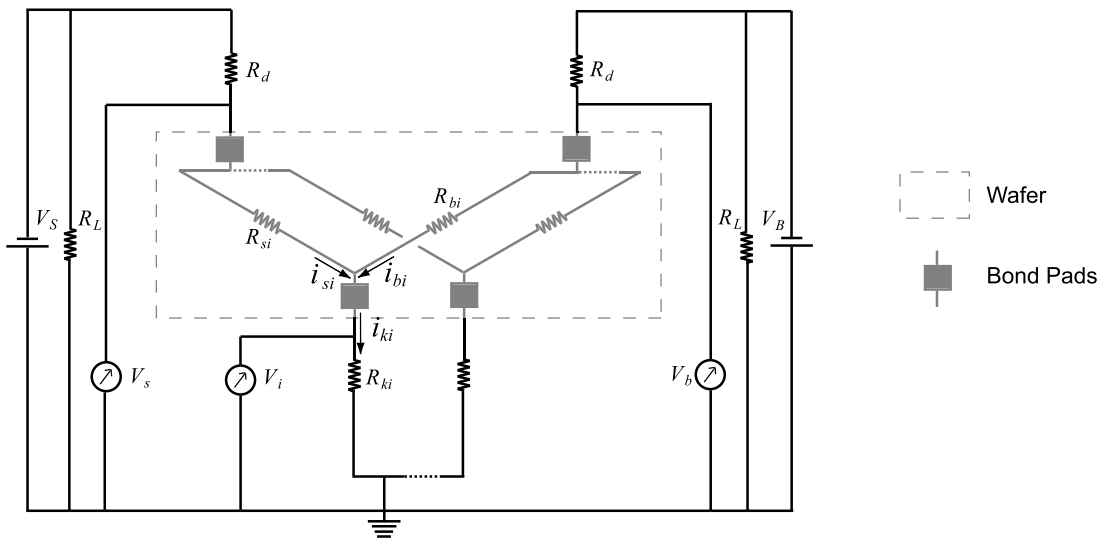

Figure 2.16: Circuit for calibrating an integrated wheatstone bridge with multiple sensors.

maintaining $V_\mathrm{b} = 0$, and then switching the voltages, applying a non-zero V_b while maintaining $V_\mathrm{s} = 0$. The resistance measurements made in this manor are an average value over duration of the two measurements. Therefore, the accuracy will be limited by rate of temperature change relative to the total time for each measurement.

2.5.4 RTD Performance Tests

Failure

The power and temperature limitations of thin film RTDs on polycarbonate are investigated by testing a series of chromium RTDs to failure. The voltage is increased linearly until failure occurs while measuring sensor resistance with a four-wire technique, i.e. independent measurements are made of the current passing through the sensor and the voltage across the sensor using four probes,

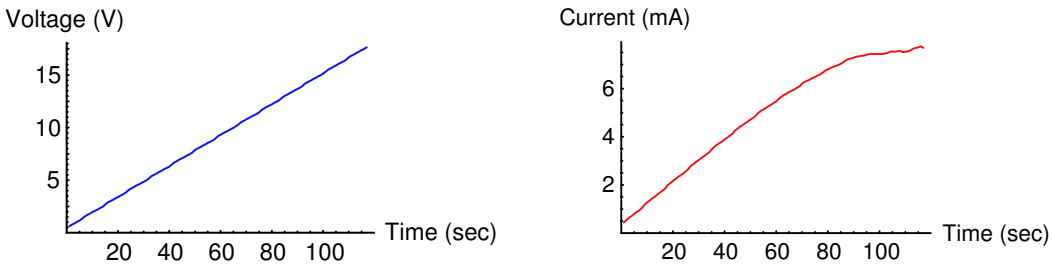

(a) (b)

Figure 2.17: Plots of voltage and current during a RTD failure test. The resistance increases dramatically shortly before failure, causing the current to stop increasing or slightly decrease despite the continued voltage increase. Voltage ramp rates are 0.22 V/sec for the 200 Å thick sensors, and 0.14 V/sec for the 1000 Å sensors. (a) Voltage. (b) Current

two at each end of the sensor. This method provides accurate resistance measurements, regardless of the contact resistance, through the entire range of the test. Sample plots of voltage and current are shown in Figure 2.17. The resistance of the sensor initially increases linearly with voltage, indicating uniform Joule heating of the sensor. However, shortly before failure, the resistance increases dramatically, as indicated in Figure 2.17. This fact, combined with the damage shown in Figure 2.18, indicates that failure occurs at the weakest or narrowest point of the sensor, and the width of this point decreases (i.e. a crack grows) as failure occurs. The most likely cause of such a crack is the thermal expansion mismatch between the polymer substrate and the metal film.

The temperature at which failure occurs may be approximated by using the TCR of the chromium, determined before testing, and the resistance change observed during testing. Applying the following relationship provides the simplest

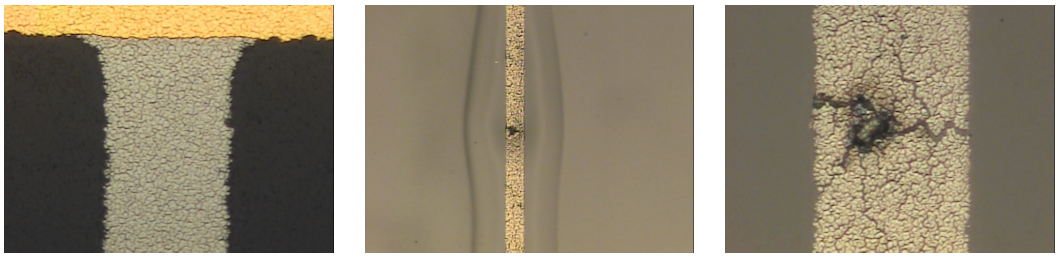

(a) (b) (c)

Figure 2.18: 1000 Å thick chromium RTD after failure caused by voltage. (a) Before testing. Crazing pattern from evaporation is visible in the gold, chromium, and polycarbonate. (b) Sensor after failure. Damage to the polycarbonate is visible. (c) Close-up. A crack has formed, presumably caused by the greater thermal expansion of the polymer substrate pulling apart the sensor.

method of determining temperature based on resistance:

$$\Delta T = \frac{1}{\alpha}\frac{R(q') - R(q'=0)}{R(q'=0)}, \quad \text{where} \qquad q' = \frac{Vi}{l} \tag{2.29}$$

This data may be used to generate a temperature curve for each test, shown in Figure 2.19. As mentioned previously, the linear resistance change at low power is due to uniform joule heating, and therefore the temperature estimated in this range may be assumed to be accurate. However, as the sensor begins to fail, the resistance increase is due to changes in the cross sectional area, so estimating temperature in this manor at high powers yields fictitious results. In Figure 2.19, the transition from a linear temperature increase to non-linear behavior represents the onset of damage to the sensor. This appears to occur at $\Delta T \approx 75°\text{C}$, or a temperature of approximately 100 °C. The slope of the linear portion of Figure 2.19 may be thought of as the heat transfer resistance of the wafer, as it relates heat generated to resulting temperature rise. If the slope is denoted β, this may

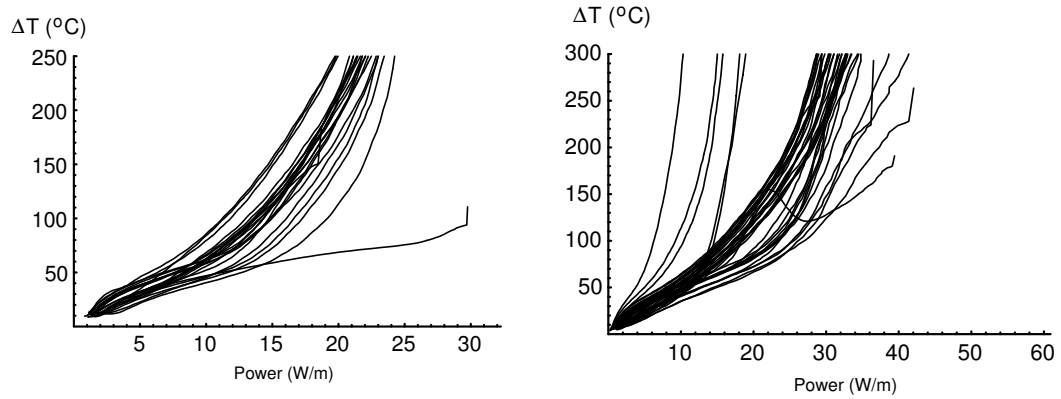

(a) (b)

Figure 2.19: Sensor temperature estimate based on resistance change versus power per unit length. Note that the sharp increase in temperature as power increases is a result of decreasing cross sectional area, not actual temperature. (a) 200 Å thick sensors. (b) 1000 Å thick sensors.

be written

$$\Delta T = \beta q' \tag{2.30}$$

The slope found from Figure 2.19 is 6 Wm/°C. This relationship may be used to estimate the average temperature of the heater at the time of failure, if the average power applied to the heater is known. Simply multiplying the voltage and current at the time of failure will give the total power, much of which is being dissipated in the region which is failing. As shown in Figure 2.18, this region is small relative to the rest of the heater. Therefore, the power applied to the bulk of the heater, excluding the power applied to the region of failure, is desired. This quantity may be approximated using the current at failure, i_{f}, and the room temperature resistance of the sensor, R_{rt}, as follows:

$$q' = R(T)I^2 = R_{\mathrm{rt}}(1 + \alpha\Delta T)I^2 \tag{2.31}$$

Equations 2.30 and 2.31 may now be combined to find the approximate temper-

	200Å	1000 Å
Mean Temperature at Failure (T_f, °C)	146	165
Standard Deviation (σ, °C)	14	41
Number of tests	22	40

Table 2.9: Sensor failure statistics for the two sets of sensors tested.

ature of the sensor at failure, T_f

$$T_f = \frac{\beta R_{rt} i_f^2}{1 - \alpha\beta R_{rt} i_f^2} + T_{rt} \tag{2.32}$$

where T_{rt} is room temperature.

The failure temperature was calculated for each test; the results are shown in Table 2.9 and Figure 2.20. The mean failure temperature was approximately 150°C for both sets of sensors, which is consistent with the damage shown in Figure 2.18b. It is reasonable to expect that temperatures in excess of the glass transition temperature of polycarbonate would be required to casue the substantial substrate damage apparent in Figure 2.18b. From the preceeing results, the following conclusions may be drawn regarding the thin film RTDs described in this chapter:

- The RTDs may be used in environments up to 100°C without damage.
- The RTDs fabricated on polycarbonate fail at approximately 150 °C.
- Failure is caused by the expansion of the substrate relative to the sensor, which ultimately tears the metal film.

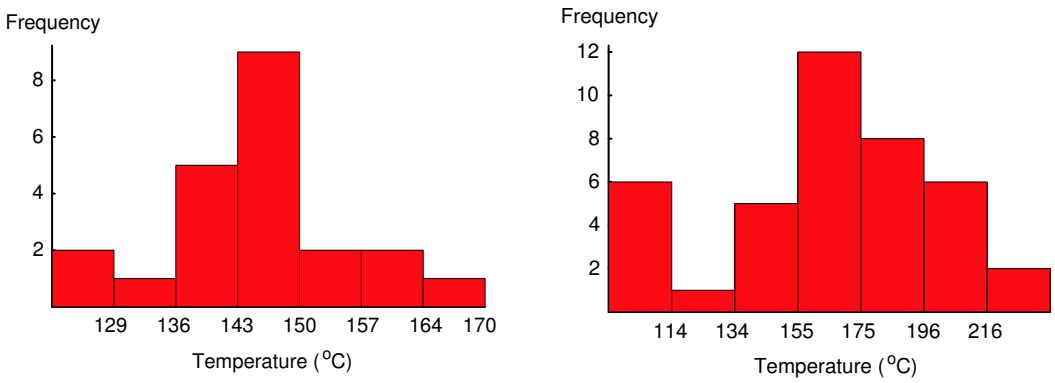

(a) (b)

Figure 2.20: Histograms of the failure temperatures for the two sets of sensors tested. (a) 200 Å thick sensors. (b) 1000 Å thick sensors.

Repeatability

Repeatability is an important parameter in evaluating an RTD's performance. The repeatability of thin film RTDs is investigated using a 200 Å thick chromium RTD fabricated on a polycarbonate substrate. A polycarbonate cover wafer containing a hole is PDMS bonded to the wafer containing the RTD, with the hole located near the RTD. A fine gauge thermocouple is embedded in the hole, and the entire stack is placed on a hotplate with foam insulation on top. This configuration ensures that the temperature measured by the thermocouple is as close as possible to the actual temperature of the RTD. This system is then cycled from 23°C to 60°C four times. The room temperature resistance of the RTD is 40.9 kΩ, and the temperature coeficient is 19.7 Ω/°C (corresponding to a TCR of 0.00048 $°C^{-1}$. After each cycle, the RTD returned to within 1.9 Ω of its original resistance; the residual change in room temperature resistance corresponds to a temperature drift of of 0.1 °C.

Thin film titanium RTDs patterned on FR-4 boards were tested in a

similar manor. The sensor readings drifted 0.065°C for each hour the sensors were maintained at 70 °C.

2.6 Integrated Silicon Components in PC Microfluidic Systems

Metals can be deposited on polycarbonate substrates, and with the above techniques can be patterned to form electrodes, RTD's, thermocouples, heaters, etc. Semiconductors pose a much greater problem, since semiconductor deposition methods usually involve temperatures which damage polycarbonate and other similar polymers. Even if methods of depositing semiconductors such as silicon on polycarbonate are developed, direct microfabrication on a PC substrate would not be practical for many devices. This is the case for small, silicon-based devices which take many processing steps to fabricate. In this case, the maximum number of devices should be batch fabricated on a single silicon wafer and then diced into individual chips which can be integrated in an inexpensive polymer microfluidic system. The key to this method is inexpensively integrating the diced semiconductor chips into a polymer microfluidic system. To date, very little work has been done in this area. The only such work was reported by Mastrangelo, and consisted of a PCR device cast in epoxy [17]. This system was fabricated by manually assembling a glass capillary with a wire coiled around it, a thermoelectric cooler, and an Omega Engineering thermocouple. This assembly was then cast in epoxy. However, no microfabrication was used in this system, and so it does not fully qualify as a microfluidic system.

Figure 2.21 outlines the process deveolped for integrating a semiconductor chip in a polymer substrate. The chip is placed face down in a PDMS coated mold. The PDMS provides for easy mold removal while also forming a seal

against the surface of the chip, preventing epoxy from covering the chip surface. The mold is placed under vacuum and filled with epoxy. Casting under vacuum prevents air bubbles from becoming trapped at the edge of the chip, which appear as large pits when the mold is removed. Filling the mold under vacuum is accomplished by placing a syringe loaded with epoxy and air in the vacuum with the mold. The trapped air slowly forces the epoxy through the small needle opening. The fill rate can be controlled by the diameter and length of the needle and epoxy viscosity. After curing of the epoxy, the mold is removed. A gap of a couple microns usually exists at the edge of the chip, which may be filled by spin coating with a layer of photodefinable polyimide. Access holes are patterned in the polyimide for electrical connections, and a metal layer is deposited and patterned.

The chip used to demonstrate this technique is a hotplate gas sensor [45]. The sensor consists of a micro-hotplate suspended over a cavity for thermal isolation. The surface of the hotplate contains electrodes beneath a tin oxide coating which changes resistivity in response to chemicals such as methanol, ethanol, and others. This chip is one square millimeter, and contains 40 bond pads for sensing and actuation. Therefore, integrating this device requires making electrical contact with the bond pads and running leads to the outside world, while running a channel over the hotplate region. This process is combined with the SU-8 microchannel formation techniques described in Section 2.3.2 to create a microfluidic system composed of heaters to vaporize a liquid, microchannels to carry the vapor, and the hot plate gas sensor[60].[1]

[1]The SU-8 microchannels and device fabrication are the work of Likun Zhu.

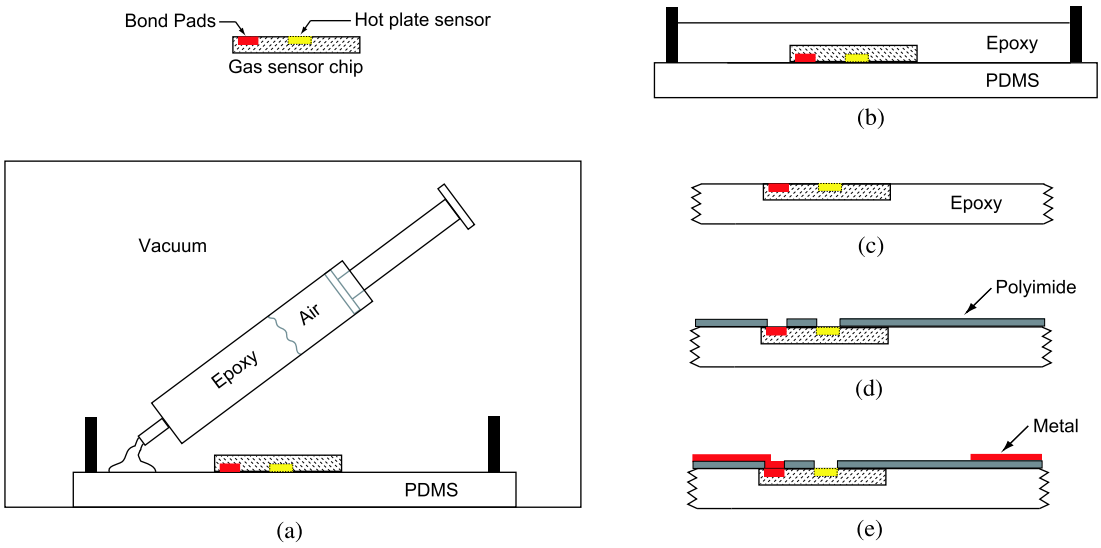

Figure 2.21: Process for integrating a small silicon chip into a polymer substrate. (a) Chip is placed in mold lined with PDMS, and filled with epoxy under vacuum. (b) Epoxy is cured at atmospheric pressure. (c) Mold is removed. (d) Photodefinable polyimide is spin coated and patterned. (e) Metal is evaporated and patterned to form leads and heaters.

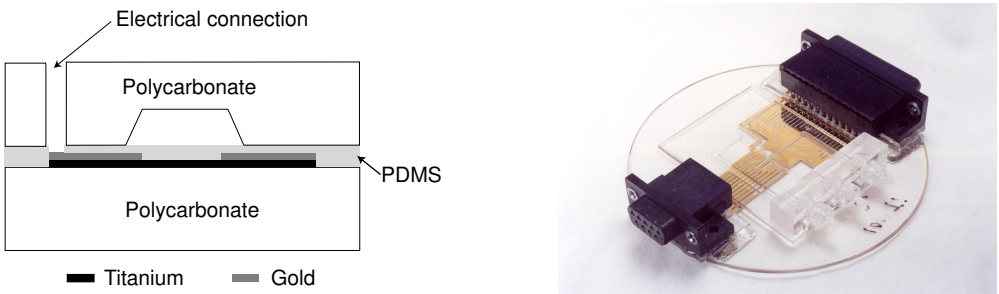

(a) (b)

Figure 2.22: Microfluidic device used for validation. (a) Photograph. (b) Cross-sectional view.

2.7 Fabrication of Demonstration Devices

2.7.1 Thermal Diffusion

A polycarbonate microfluidic device is fabricated [61] with thin film microheaters and RTDs integrated directly into the microchannels. A cross section of the system is shown in Figure 2.22a. The channels are fabricated by hot embossing of polycarbonate with an anisotropically etched silicon mold. The thin film components are made on a separate polycarbonate substrate by evaporating a 1000 Å thick layer of titanium followed by a 5000 Å thick layer of gold. The titanium serves as an adhesion layer and is also used for the RTDs, while the gold layer provides for low resistance electrical leads. As described in Section 2.4.3, a thin layer of PDMS (2-3 μm) is spun onto the wafer containing the channels. This PDMS layer is partially cured, and the two wafers are brought into contact. The PDMS is then allowed to fully cure, bonding the two wafers and sealing the microchannels. High density electrical connections are realized by attaching an inexpensive D-subminiature connector to the gold bond pads with silver-filled epoxy.

Fluid connections are accomplished with inexpensive polycarbonate molded fittings and connector blocks. The fittings are barbed on one end and thread into the connector block on the other end. The connector block is then epoxied to the wafer to form a seal with the reservoir holes. The completed device is shown in Figure 2.22b. The sensors are wired in parallel wheatstone bridges with the balancing resistors and reference leg integrated into the device. The TCR of each resistor and microheater is determined experimentally by heating the whole device on a hot plate with external thermocouples attached to the top and bottom of the device. The resistance changes of the resistors and microheaters are measured during this calibration procedure with the method described in Section 2.5.3. The maximum temperature variation throughout the device during this calibration process is found to be less than 0.5°C. The sensors are found to have a resolution of 0.025°C, based on the accuracy (5 μV) of the voltage meter used for measurements. The device was tested using an automated control and data aquisition system, shown in Figure 2.23. A LabView program controlled the power supplies and syringe pump required for testing, while an Agilent 34970A Switching unit performed all the necessary data aquisition.

2.7.2 Temperature Gradient Gel Electrophoresis

Thin film micro-heaters and RTDs allow for more precise control of substrate temperature with less power compared with bulk external heaters and sensors. However, integrating sensors and heaters into a microchannel does add cost to the device, which is particularly undesirable if the device must be disposable. In some applications, it may be desirable to separate the heaters and sensors from the channels so that the heaters and sensors may be reused while

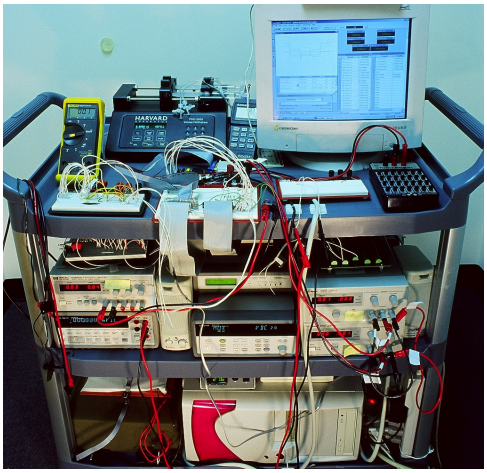

Figure 2.23: Testing equipment used for measurements. Top shelf contains a syringe pump (Harvard PHD2000 Infuse/Widthdraw), solderless bread boards, and selectable resistor. Middle shelf contains power supplies (Agilent E3600 series) and data acquisition unit (Agilent 34970A). The bottom shelf contains a hotplate for calibration and a computer with a National Instruments IO card and LabView for automated test control.

disposing of the channels. This arrangement maintains the benefits of thin film micro-heaters and RTDs while minimizing the cost of the disposable component of the system. One such application is Temperature Gradient Gel Electrophoresis (TGGE), in which a linear temperature gradient must be maintained along the length of a microchannel.

This is accomplished by fabricating the microchannels in polycarbonate and fabricating the thin-film heaters and sensors on FR-4 boards [41]. The microchannels are formed by hot embossing polycarbonate with an anisotropically etched (100) silicon wafer and sealed by thermally bonding to a second polycarbonate wafer containing fluid access holes. The electrical component fabrication begins with copper-clad FR4 boards. The copper is patterned to interface with a commercial card edge connector, allowing for reliable and simple electrical connections. A 1000 Å thick layer of titanium is deposited, followed by a 1200 Å or 6000 Å thick layer of gold. The metal layers are then patterned to form microheaters and RTDs. The measured bulk resistivity of the resulting gold layer (150×10^{-9} Ωm) is significantly higher than the value predicted by handbooks [48] (24×10^{-9} Ωm), presumably due to the very high surface roughness of the FR-4 board. The overall roughness is 710 nm RMS. Since FR-4 is a woven fiberglass laminate, the weave (which has a period of approximately 1 mm) contributes significantly to the roughness. If the effect of the weave is subtracted, the roughness is still high, with a RMS value of 590 nm. However, the roughness and high sheet resistances did not affect the performance of the microheaters or RTDs. The design of this device is discussed further in Chapter 4.

Chapter 3

Thermal Models and Experimental Results

3.1 Introduction

Integrating microheaters into a system will cause temperature non-uniformities in the substrate, which must be accounted for in the system design. This becomes increasingly difficult in systems containing many components. For example, heat from a bubble pump or hotplate gas sensor could cause unwanted effects in nearby channels. Therefore, a thermal model of the system is generally required for design and/or validation.

Many existing microfluidic systems are fabricated on silicon, quartz, or glass substrates. The high thermal conductivity of these materials requires the heaters to be isolated to conserve power. The structures required to thermally isolate the heated components make the geometries too complicated for analytical models, so Finite Element Analysis (FEA) is often used. FEA models are time consuming to generate, may be difficult to change, and may have problems converging when both fluid and thermal phenomena are modeled. Furthermore, a model generated for one isolated heater system generally can't be applied to another system, because the isolation structures vary greatly with the fabrication process used.

The low thermal conductivity of polymers allows heaters to be made directly on the substrate without any isolating structures, which simplifies the fabrication process and further reduces the cost [61, 62]. However, this will result in a significant area of the substrate being heated, which may affect nearby components of the system. These effects must be considered when designing such a system. The geometry of a non-isolated heater system is usually simple enough to be modeled analytically. A model generated for one non-isolated heater may be applied to a variety of other systems simply by changing the size of the heater and substrate. Therefore, a general model is developed for non-isolated microheaters in a microchannel and experimental validation of this model [63].

Turbulent mixing of liquids is difficult to achieve at the microscale. When two liquid streams of different temperatures (or different chemical species concentrations) are brought together, thermal (or concentration) equilibrium will only be achieved by conduction (or diffusion) through the fluid. Therefore, thermal and chemical diffusion in microfluidic systems is of significant interest. Previous studies [64] have employed a heater and array of RTDs in a microchannel to verify the temperature dependence of fluid flows in microchannels. An analytical model and experimental verification of thermal diffusion between fluids of different temperatures in a microchannel will be presented. The results obtained for thermal diffusion may be readily applied to chemical species diffusion, which will be discussed later.

3.2 Background

3.2.1 Governing Thermal Equations

Heat transfer in a stationary meduim is governed by the heat equation,

$$\frac{\partial}{\partial x}\left(k\frac{\partial T}{\partial x}\right)+\frac{\partial}{\partial y}\left(k\frac{\partial T}{\partial y}\right)+\frac{\partial}{\partial z}\left(k\frac{\partial T}{\partial z}\right)+q'''(x,y,z)=\rho c_p\frac{\partial T}{\partial t} \tag{3.1}$$

where $q'''(x,y,z)$ is volumetric internal heat generation. If the thermal conductivity is uniform throughout the domain and only steady state is considered, the heat equation reduces to

$$k\left(\frac{\partial^2 T}{\partial x^2}+\frac{\partial^2 T}{\partial y^2}+\frac{\partial^2 T}{\partial z^2}\right)+q'''(x,y,z)=0 \tag{3.2}$$

Equation 3.2 may be solved by separation of variables only if $q'''(x,y,z)=0$, i.e. no internal heat generation. Otherwise, Equation 3.2 is a form of Poisson's equation and may be solved through Green's functions, as described in Section 3.2.2

Heat transfer in an incompressible fluid is governed by the thermal energy equation [65], which in two-dimensional form is

$$\rho c_p\left(u\frac{\partial T}{\partial x}+v\frac{\partial T}{\partial y}\right)=\frac{\partial}{\partial x}\left(k\frac{\partial T}{\partial x}\right)+\frac{\partial}{\partial y}\left(k\frac{\partial T}{\partial y}\right)+\mu\Phi+q'''(x,y,z) \tag{3.3a}$$

where

$$\Phi=\left(\frac{\partial u}{\partial y}+\frac{\partial v}{\partial x}\right)^2+2\left[\left(\frac{\partial u}{\partial x}\right)^2+\left(\frac{\partial v}{\partial y}\right)^2\right]-\frac{2}{3}\left(\frac{\partial u}{\partial x}+\frac{\partial v}{\partial y}\right)^2 \tag{3.3b}$$

The following assumptions are made to simplify Equation 3.3:

Laminar flow: Laminar fluid flow occurs when the Reynolds numbers is below approximately 5×10^5. For water in a 100 μm deep channel, the Reynolds number is $0.057u$, where u is velocity in mm/sec. The maximum velocity

used in these experiments is 10 mm/sec; therefore it is clear that all flows will be laminar. The length of the channel is assumed to be in the x-direction, therefore the v terms in Equation 3.3 are all zero.

Fully developed flow: The fluid enters the microchannel with a uniform velocity profile, but after a distance $x_{\mathrm{fd,h}}$, the fluid develops a parabolic velocity profile. This is refered to as the hydrodynamic entry length, and for laminar flow it is approximately

$$\frac{x_{\mathrm{fd,h}}}{L} \approx 0.05\mathrm{Re}_L \tag{3.4}$$

For water in a μm deep channel, the hydrodynamic entry length is $0.285u$ μm, where u is velocity in mm/sec. It is clear that beyond a few microns from the entrance, fully developed flow exists and the velocity in the x-direction does not vary throughout the length of the channel. Therefore, $\partial u/\partial x = 0$. In the case of fluid flow over a microheater, the thermal entrance length for laminar flow is approximately

$$\frac{x_{\mathrm{fd,h}}}{L} \approx 0.05\mathrm{Re}_L\mathrm{Pr} \tag{3.5}$$

Assuming water in a 100 μm deep channel, the thermal entry length is $3.7u$ μm, where u is velocity in mm/sec. The maximum velocity used in this study is 10 mm/sec, producing a maximum thermal entrance length of 37 μm, while the heater widths range from 25-100 μm. Therefore, thermally fully developed flow will be assumed in some of the following derivations.

No internal heat generation: $q'''(x, y, z) = 0$.

Uniform properties: Material properties are assumed not to vary with temperature or location in the domain. With this and the previous assumptions of

laminar, hydrodynamically fully developed flow without heat generation, Equation 3.3 simplifies to

$$\rho c_p u \frac{\partial T}{\partial x} = k\left(\frac{\partial^2 T}{\partial x^2} + \frac{\partial^2 T}{\partial y^2}\right) + \mu\left(\frac{\partial u}{\partial y}\right)^2 \tag{3.6}$$

Uniform velocity profile: Equation 3.6 still must be solved numerically. If the velocity is assumed to be constant across the width of the channel, then Equation 3.6 reduces to

$$\frac{\partial^2 T}{\partial x^2} + \frac{\partial^2 T}{\partial y^2} = \frac{\rho c_p u_{\text{avg}}}{k_{\text{f}}} \frac{\partial T}{\partial x}, \tag{3.7}$$

which can be solved analytically. This is clearly not the case for a microchannel subjected to pressure driven flow, which will result in a parabolic velocity profile. However, an analytic solution provides more insight into the effect of parameters on results, and is often much simpler than numerically solving a PDE. Therefore, this assumption is made and some of the resulting solutions are compared with numerical models which account for the parabolic velocity profile (see Section 3.3.3).

3.2.2 Green's Functions in Heat Conduction

Green's functions provide a convenient method of solving a wide variety of dynamic and stead state heat transfer problems based on Equation 3.1 [66]. The Steady State Green's Function (SSGF) for a given problem is based on the boundary conditions of the domain, and denoted $G(\mathbf{r}|\mathbf{r}')$, where $\mathbf{r}$ is a position vector, and $\mathbf{r}'$ is a dummy variable. The steady state temperature distribution is

found from the Green's function with the following relationship:

$$\begin{aligned} T(\mathbf{r}) &= \int_R \frac{1}{k} G(\mathbf{r}|\mathbf{r}') q'''(\mathbf{r}')\,\mathrm{d}V' + \sum_{i=1}^{s} \int_{S_i} \frac{f_i(\mathbf{r_i'})}{k_i} G(\mathbf{r}|\mathbf{r_i'})\,\mathrm{d}s_i \\ &\quad + \sum_{j=1}^{s} \int_{S_j} f_j(\mathbf{r_j}) \left.\frac{\partial G}{\partial n_j'}\right|_{\mathbf{r}'=\mathbf{r_j'}} \mathrm{d}s_j \end{aligned} \tag{3.8}$$

where the first term accounts for internal heat generation, the second term accounts for Neumann boundary conditions, and the third term accounts for Dirichlet boundary conditions. In Equation 3.8 R is the domain being modeled, S_i is the i^{th} boundary, f_i is the i^{th} boundary condition, n_i is the normal vector to boundary S_i, and s is the number of boundary conditions of each type. One-dimensional Green's functions may be looked up in tables directly [66]; two and three-dimensional Green's functions may be constructed by multiplying the appropriate one-dimensional functions for each dimension, i.e. $G_{xyz}(x,y,z) = G_x(x)G_y(y)G_z(z)$. Green's functions are generally given as transient functions; the SSGF may be derived from the transient Green's function with:

$$G(\mathbf{r}|\mathbf{r}') = \lim_{t\to\infty} \int_{\tau=0}^{t} \alpha G(\mathbf{r}, t|\mathbf{r}', \tau)\,\mathrm{d}\tau \tag{3.9}$$

where τ is a dummy time variable. For a one-dimensional transient problem, the temperature distribution is found from the transient Green's function with the following relationship:

$$\begin{aligned} T(x,t) = &\int_{x'=0}^{L} G(x,t|x',0)F(x')dx' \\ &+ \frac{\alpha}{k} \int_{\tau=0}^{t} \int_{x'=0}^{L} g(x',\tau)G(x,t|x',\tau)dx'd\tau \\ &+ \alpha \int_{\tau=0}^{t} \sum_{i=1}^{2} \left[\frac{f_i(\tau)}{k_i} G(x,t|x_i,\tau)\right] d\tau \\ &- \alpha \int_{\tau=0}^{t} \sum_{i=1}^{2} \left[f_i(\tau) \left.\frac{dG}{dn_i'}\right|_{x'=x_i}\right] d\tau \end{aligned} \tag{3.10}$$

where the first term accounts for the initial condition, the second term accounts for internal energy generation, the third term accounts for Neumann boundary conditions, and the final term accounts for Dirichlet boundary conditions. The one-dimensional transient Green's functions for some common boundary conditions are listed here [66], with boundary conditions listed as $x = 0/x = L$.

Temperature/Temperature

$$G(x,t|x',\tau) = \frac{2}{L}\sum_{m=1}^{\infty} \mathrm{e}^{-m^2\pi^2\alpha(t-\tau)/L^2} \sin\left(m\pi\frac{x}{L}\right)\sin\left(m\pi\frac{x'}{L}\right) \tag{3.11a}$$

Temperature/Heat Flux

$$\begin{aligned} G(x,t|x',\tau) &= \frac{2}{L}\sum_{m=1}^{\infty} \mathrm{e}^{-\beta_m^2\alpha(t-\tau)/L^2} \sin\left(\beta_m\frac{x}{L}\right)\sin\left(\beta_m\frac{x'}{L}\right) \qquad (3.11b)\\ \beta_m &= \left(m-\frac{1}{2}\right)\pi \end{aligned}$$

Temperature/Convection

$$\begin{aligned} G(x,t|x',\tau) &= \frac{2}{L}\sum_{m=1}^{\infty} \mathrm{e}^{-\beta_m^2\alpha(t-\tau)/L^2} C_m \sin\left(\beta_m\frac{x}{L}\right)\sin\left(\beta_m\frac{x'}{L}\right) \qquad (3.11c)\\ B &= \frac{hL}{k}, \quad \beta_m\cot\beta_m = -B,\\ C_m &= \frac{\beta_m^2+B^2}{\beta_m^2+B^2+B} \end{aligned}$$

Heat Flux/Heat Flux

$$G(x,t|x',\tau) = \frac{1}{L}\left[1+2\sum_{m=1}^{\infty} \mathrm{e}^{-m^2\pi^2\alpha(t-\tau)/L^2} \cos\left(m\pi\frac{x}{L}\right)\cos\left(m\pi\frac{x'}{L}\right)\right] \tag{3.11d}$$

Heat Flux/Convection

$$\begin{aligned} G(x,t|x',\tau) = & \frac{2}{L}\sum_{m=1}^{\infty} \mathrm{e}^{-\beta_m^2\alpha(t-\tau)/L^2} C_m \cos\left(\beta_m\frac{x}{L}\right)\cos\left(\beta_m\frac{x'}{L}\right) \qquad (3.11e)\\ B &= \frac{hL}{k}, \quad \beta_m\tan\beta_m = -B, \quad C_m = \frac{\beta_m^2+B^2}{\beta_m^2+B^2+B} \end{aligned}$$

Convection/Convection

$$
\begin{aligned}
G(x,t|x',\tau) &= \frac{2}{L}\sum_{m=1}^{\infty} \mathrm{e}^{-\beta_m^2 \alpha (t-\tau)/L^2} \frac{1}{C_m} \left[\beta_m \cos\left(\beta_m \frac{x}{L}\right) + B_1 \sin\left(\beta_m \frac{x}{L}\right)\right] \\
&\qquad \times \left[\beta_m \cos\left(\beta_m \frac{x'}{L}\right) + B_1 \sin\left(\beta_m \frac{x'}{L}\right)\right] \qquad (3.11\text{f}) \\
B_1 &= \frac{h_1 L}{k}, \quad B_2 = \frac{h_2 L}{k}, \quad \tan\beta_m = \frac{\beta_m (B_1 + B_2)}{\beta_m^2 - B_1 B_2} \\
C_m &= (\beta_m^2 + B_1^2)\left(1 + \frac{B_2}{\beta_m^2 + B_2^2}\right) + B_1
\end{aligned}
$$

3.3 Thermal Models

The first goal is to develop a simple model which predicts the temperature distribution in a polymer microfluidic system due to integrated heaters. There are three effects which will be considered:

- The temperature distribution in a polymer substrate due to a microheater, ignoring the presence of microchannels. This is a function of boundary conditions, geometry, and thermal conductivity. See Section 3.3.1.
- The effect of a fluid flowing over the microheater, which is approximated as a function of flow velocity only. See Section 3.3.2.
- Temperature (or species concentration) non-uniformities within the fluid in the microchannel. See Section 3.3.3.

The first two effects are accounted for by deriving a relationship which predicts the temperature rise, ΔT (°C), for a given heater power per unit length, q' (W/m). A linear relationship is used, as suggested by Fourier's Law, with the proportionality constant denoted β:

$$\Delta T = \beta q'. \qquad (3.12)$$

We make the assumption that the constant β may be approximated by partitioning as follows:

$$\beta = \frac{1}{k} C_{\mathrm{bc}} C_{\mathrm{f}} C_{\mathrm{s}}, \tag{3.13}$$

where k is the thermal conductivity, C_{bc} is a non-dimensional term which takes into account the heater dimensions, wafer dimensions, and boundary conditions, C_{f} is a non-dimensional term which accounts for the effects of fluid flow in the microchannel, and C_{s} is a non-dimensional term which accounts for serpentine heater geometries.

3.3.1 Thin Film Heater

The model consists of a three dimensional rectangular region with a thin film microheater embedded in the center of the region, shown in Figure 3.1. Since there is no microchannel and only one straight heater, $C_{\mathrm{f}} = C_{\mathrm{s}} = 1$. Therefore, Equation 3.12 and 3.13 simplifies to

$$\Delta T = \frac{1}{k} C_{\mathrm{bc}} q'. \tag{3.14}$$

The sides of the rectangular region are subject to convection, while the top and bottom are subject to one of the following three conditions:

I. Conduction ($T = 0$) on both top and bottom.

II. Conduction ($T = 0$) on bottom and convection ($k\,dT/dy + h_y T = 0$) on top.

III. Convection ($k\,dT/dy \pm h_y T = 0$) on both top and bottom.

The solutions to Cases I and III are symmetric about the $y = L_y/2$ plane; therefore, only the region $0 \leq y \leq L_y/2$ is modeled. The heat flux applied to the

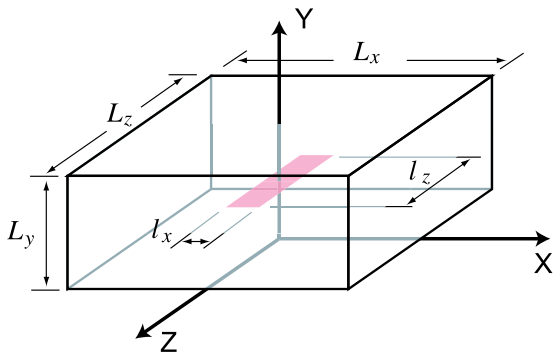

Figure 3.1: Geometry and dimensions of the heater model. The shaded area is a thin film heater.

$y = L_y/2$ boundary is q'' over the heater region and zero elsewhere. Separation of variables can now be used to solve these cases. Case II is not symmetric, and is solved using Green's functions [66].

The following non-dimensional parameters are defined:

$$\begin{aligned} x' &= \frac{x}{L_x/2}, & y' &= \frac{y}{L_y}, & z' &= \frac{z}{L_z/2}, & & \\ r_x &= \frac{l_x}{L_x}, & r_z &= \frac{l_z}{L_z}, & r_{xy} &= \frac{L_y}{L_x}, & r_a &= \frac{l_z}{l_x}, \\ Bi_x &= \frac{h_x L_x}{k}, & Bi_y &= \frac{h_y L_y}{k}, & Bi_z &= \frac{h_z L_z}{k}, & & \end{aligned} \tag{3.15}$$

where L_x, L_y, L_z, l_x, and l_z are defined in Figure 3.1. The convection coefficients h_x, h_y, and h_z apply to the $x = \pm L_x/2$, $y = 0, L_y$, and $z = \pm L_z/2$ surfaces, respectively. Equation 3.2, the three-dimensional heat equation, is solved subject to the boundary conditions described above and the assumption $L_x = L_z$. The

result is

$$T(x',y',z') = -\frac{q'}{kr_x}\sum_{m=1}^{\infty}\sum_{n=1}^{\infty} C_{mn}\cos(\beta_m x')\cos(\lambda_n z')C_y(y'), \tag{3.16a}$$

$$C_{mn} = \frac{C_{xm}C_{zn}}{\beta_m\lambda_n}\sin(\beta_m r_x)\sin(\lambda_n r_z), \tag{3.16b}$$

$$C_y(y) = \begin{cases} \dfrac{1}{\gamma_{mn}}\dfrac{\sinh(\gamma_{mn}r_{xy}y')}{\cosh(\gamma_{mn}r_{xy})} & : \text{ Case I} \\ \displaystyle\sum_{l=1}^{\infty}\frac{2C_{yl}}{r_{xy}\phi_{lmn}}\sin(\frac{\gamma_l}{2})\sin(\gamma_l y') & : \text{ Case II} \\ \dfrac{1}{\gamma_{mn}}(\dfrac{E^{\gamma_{mn}r_{xy}y'}+A_{mn}E^{-\gamma_{mn}r_{xy}y'}}{E^{\gamma_{mn}r_{xy}}-A_{mn}E^{-\gamma_{mn}r_{xy}}}) & : \text{ Case III} \end{cases} \tag{3.16c}$$

$$\begin{aligned} A_{mn} &= \frac{\gamma_{mn}r_{xy}-Bi_y}{\gamma_{mn}r_{xy}+Bi_y}, \quad C_{xm} = \frac{\beta_m^2+Bi_x^2}{\beta_m^2+Bi_x+Bi_x^2}, \\ C_{yl} &= \frac{\gamma_l^2+Bi_y^2}{\gamma_l^2+Bi_y+Bi_y^2}, \quad C_{zn} = \frac{\lambda_n^2+Bi_z^2}{\lambda_n^2+Bi_z+Bi_z^2}, \\ \phi_{lmn} &= \beta_m^2+\left(\frac{\lambda_n}{r_{xz}}\right)^2+\left(\frac{\gamma_l}{2r_{xy}}\right)^2, \\ \frac{Bi_x}{2} &= \beta_m\tan\beta_m, \quad \frac{Bi_z}{2} = \lambda_n\tan\lambda_n, \\ Bi_y &= -\gamma_l\cot\gamma_l, \quad \gamma_{mn} = \sqrt{\beta_m^2+\left(\frac{\lambda_n}{r_{xz}}\right)^2}. \end{aligned} \tag{3.16d, 3.16e}$$

It should be noted that γ_l comes from the Green's function solution and is used for case II, while γ_{mn} comes from the separation of variables solution and is used for cases I and III.

Average Heater Temperature

Equation 3.16a may be used to find the parameter C_{bc} needed in Equation 3.14 by taking the average temperature over the microheater region. This can be

expressed as

$$\bar{T} = \frac{1}{r_x r_z} \int_0^{r_x} \int_0^{r_z} T(x', y' = \frac{L_y}{2}, z') \mathrm{d}z' \, \mathrm{d}x' = \frac{1}{k} C_{\mathrm{bc}} q'. \tag{3.17}$$

Evaluating Equation 3.17 yields

$$C_{\mathrm{bc}} = -\frac{1}{r_x^2 r_z} \sum_{m=1}^{\infty} \sum_{n=1}^{\infty} C_{mn}^* C_y^*, \tag{3.18a}$$

$$C_{mn}^* = \frac{C_{xm} C_{zn}}{\beta_m^2 \lambda_n^2} \sin^2(\beta_m r_x) \sin^2(\lambda_n r_z), \tag{3.18b}$$

$$C_y^* = \begin{cases} \dfrac{\tanh(\gamma_{mn} r_{xy})}{\gamma_{mn}} & : \text{ Case I} \\ \displaystyle\sum_{l=1}^{\infty} \frac{2 C_{yl}}{r_{xy} \phi_{lmn}} \sin^2(\frac{\gamma_l}{2}) & : \text{ Case II} \\ \dfrac{1}{\gamma_{mn}} (\dfrac{E^{\gamma_{mn} r_{xy}} + A_{mn} E^{-\gamma_{mn} r_{xy}}}{E^{\gamma_{mn} r_{xy}} - A_{mn} E^{-\gamma_{mn} r_{xy}}}) & : \text{ Case III} \end{cases} . \tag{3.18c}$$

Temperature Distribution

The temperature at some point away from the microheater may be found directly from Equation 3.16a. However, this may be impractical due to the complexity and multiple summations. Therefore, a simplified approximation of Equation 3.16a is desirable. Since most microsystems are fabricated in planar processes, it is reasonable to only consider the temperature distribution on the plane of the microheater, $y = L_y/2$. The system may be further simplified by averaging the temperature in the z-direction, and considering the temperature distribution to be a function of x only. These assumptions yield a one-dimensional temperature distribution:

$$\bar{T}(x') = \frac{1}{r_z} \int_0^{r_z} T(x', y' = \frac{L_y}{2}, z') \mathrm{d}z'. \tag{3.19}$$

The region $r_x \leq x' \leq 1$ is considered, and Equation 3.19 is normalized such that its value ranges from unity at $x' = r_x$ to zero at $x' = 1$:

$$\bar{T}'(x') = \frac{\bar{T}(x')}{\bar{T}(r_x)} \tag{3.20}$$

The decay of Equation 3.20 is very similar to an exponential decay; therefore, it may be approximated with a simple exponential function without significant loss in accuracy. We assume a function of the form

$$\bar{T}'(x') \approx \mathrm{e}^{-\sigma(x'-r_x)} \tag{3.21}$$

The constant σ may be found through minimization by defining the objective function

$$f(\sigma) = \int_{r_x}^{1} (\bar{T}'(x') - \mathrm{e}^{-\sigma(x'-r_x)})^2 \mathrm{d}\, x'. \tag{3.22}$$

The error will be minimized when

$$f'(\sigma) = \frac{\partial f}{\partial \sigma} = 0. \tag{3.23}$$

For a given boundary condition and r_{xy} value, the optimum σ is found to vary less then 5% in the range $5 \leq r_a \leq 500$ and $0.01 \leq r_z \leq 1$. Therefore, σ can be considered to be only a function of geometry and r_{xy}. The temperature at any point x' may now be approximated as

$$T(x') = \frac{1}{k} C_{\mathrm{bc}} C_{\mathrm{f}} C_{\mathrm{s}} \mathrm{e}^{-\sigma(x'-r_x)} q'. \tag{3.24}$$

Some values of σ have been computed and are given in Table 3.2.

Compact Model

Equation 3.18 and Equation 3.23 are cumbersome and time consuming to calculate, particularly for small values of r_x, r_z, and r_{xy}. To make the model

more practical, these equations are solved over the parameter range $5 \leq r_a \leq 500$, $0.01 \leq r_z \leq 1$, and $0.005 \leq r_{xy} \leq 0.1$, and non-linear regression is used to find an accurate yet simple to compute equation:

$$\begin{aligned} C_{\rm bc}(r_a, r_z, r_{xy}) &= \exp\big(C_0(r_{xy}) + C_1(r_{xy}) \ln r_a + C_2(r_{xy}) \ln r_z \\ &\quad + C_3(r_{xy}) \ln r_a \ln r_z + C_4(r_{xy}) \ln^2 r_a + C_5(r_{xy}) \ln^2 r_z \\ &\quad + C_6(r_{xy}) \ln^2 r_a \ln r_z + C_7(r_{xy}) \ln r_a \ln^2 r_z\big) \end{aligned} \tag{3.25}$$

The values of $C_i(r_{xy})$ are given in Table 3.1. As mentioned previously, the value of σ varied less than 5% over the parameter range, so the relevant values are given directly in Table 3.2. For both $C_{\rm bc}$ and σ, values do not change with further increases in r_a or decreases in r_z outside of the given range, so values of $r_a > 500$ may be approximated with $r_a = 500$ and values of $r_z < 0.01$ may be approximated with $r_z = 0.01$.

Serpentine Heaters

The preceding model is for a single microheater, but may be readily adapted for a microheater containing several segments (serpentine) or an array of microheaters using the paramter $C_{\rm s}$ in Equations 3.12-3.13 and 3.24. The first heater of the array is assumed to start at $x' = 0$, the number of heaters in the array is N, and the spacing between heaters is s. The average temperature of the heater array is assumed to be

$$\bar{T} = \frac{1}{k} C_{\rm bc} C_{\rm f} \bar{C}_{\rm s} q', \tag{3.26}$$

and the temperature distribution is approximated as

$$T(x') = \frac{1}{k} C_{\rm bc} C_{\rm f} C_{\rm s} {\rm e}^{-\sigma x'} q'. \tag{3.27}$$

Case	r_{xy}	C_0	C_1	C_2	C_3	C_4	C_5	C_6	C_7
I.	0.005	-8.12	1.92	-2.24	0.558	-0.151	-0.211	-0.0320	0.0318
	0.01	-7.27	1.86	-2.22	0.538	-0.147	-0.227	-0.0308	0.0310
	0.05	-4.73	1.34	-1.66	0.430	-0.115	-0.204	-0.0275	0.0266
	0.1	-3.68	1.06	-1.29	0.337	-0.0927	-0.173	-0.0220	0.0205
II.	0.005	-7.32	1.87	-2.21	0.560	-0.150	-0.218	-0.0332	0.0327
	0.01	-6.30	1.70	-2.07	0.516	-0.139	-0.227	-0.0310	0.0308
	0.05	-3.71	1.05	-1.29	0.335	-0.0909	-0.176	-0.0216	0.0206
	0.1	-2.86	0.812	-0.939	0.251	-0.0712	-0.143	-0.0166	0.0148
III.	0.005	-0.482	0.685	-0.879	0.237	-0.0619	-0.169	-0.0161	0.0152
	0.01	-0.372	0.539	-0.630	0.177	-0.0484	-0.146	-0.0120	0.0111
	0.05	-0.585	0.373	-0.188	0.0982	-0.0330	-0.0766	-0.00676	0.00475
	0.1	-0.841	0.384	-0.133	0.0918	-0.0341	-0.0568	-0.00658	0.00345

Table 3.1: $C_i(r_{xy})$ as a function of boundary conditions.

	r_{xy}			
Case	0.005	0.01	0.05	0.1
I. Conduction	332	128.	40.0	24.0
II. Mixed	204	81.4	23.6	13.8
III. Convection	11.6	8.30	4.30	3.45

Table 3.2: $\sigma(r_{xy})$ as a function of boundary conditions.

With the non-dimensional parameters

$$r_h = \frac{s}{l_x} \quad \text{and} \quad d_i = (i-1)(r_h+1), \tag{3.28}$$

the coefficients $\bar{C}_\mathrm{s}$ and C_s may be written

$$\bar{C}_\mathrm{s} = \frac{1}{N}\sum_{i=1}^{N}\sum_{j=1}^{N}\int_{d_i}^{d_{i+1}} f_j(x')\mathrm{d}x' \tag{3.29}$$

$$C_\mathrm{s} = \sum_{i=1}^{N} \mathrm{e}^{C_\sigma r_x(ir_h+i-r_h)} \tag{3.30}$$

$$f_j(x') = \begin{cases} \mathrm{e}^{-\sigma r_x(d_j-x')} & : \quad -\infty < x' < d_j \\ 1 & : \quad d_j \le x' \le d_j+1 \\ \mathrm{e}^{-\sigma r_x(x'-d_j-1)} & : \quad d_j+1 < x' < \infty \end{cases}$$

3.3.2 Flow in a Microchannel

The effect of fluid flow over a microheater is approximated with two-dimensional models, as shown in Figure 3.2. Separate models are derived for the substrate and channel in terms of the applied heat flux on the interface between the two. Optimization is then used to determine the heat flux which satisfies temperature compatibility between the channel and substrate interface. The following boundary conditions are assumed:

Substrate:

$$\begin{aligned} T_\mathrm{s}(x=0,y) &= 0, \qquad & T_\mathrm{s}(x,y=0) &= 0, \\ T_\mathrm{s}(x=L_x,y) &= 0, \qquad & -k\left.\frac{\partial T_\mathrm{s}}{\partial y}\right|_{y=L_{ys}} &= q''_\mathrm{s}(x) \end{aligned} \tag{3.31a}$$

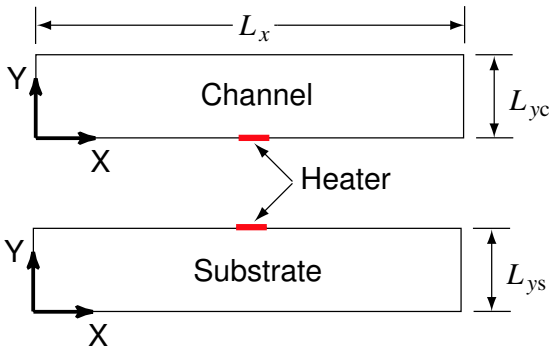

Figure 3.2: Geometry used for flow model.

Channel:

$$\begin{aligned} T_{\rm c}(x=0,y)=0, \qquad & \left.\frac{\partial T_{\rm c}}{\partial y}\right|_{y=0} = \quad q''_{\rm c}(x), \\ T_{\rm c}(x=L_x)=0, \qquad & -k\left.\frac{\partial T_{\rm c}}{\partial y}\right|_{y=L_{yc}} = \quad 0 \end{aligned} \tag{3.31b}$$

The following non-dimensional parameters are defined:

$$\begin{aligned} x' = \frac{x}{L_x}, \qquad y' = & \begin{cases} y/L_{ys} & : \text{ Substrate} \\ y/L_{yc} & : \text{ Channel} \end{cases}, \\ r_x = \frac{l_x}{L_x}, \qquad r_{xys} = & \frac{L_{ys}}{L_x}, \quad r_{xyc} = \frac{L_{yc}}{L_x}, \quad a = \frac{\rho c_p u_{\rm avg} L_x}{k_{\rm f}} \end{aligned} \tag{3.32}$$

where l_x is the width of the microheater, ρ is the fluid's density, c_p is the fluid's heat capacity , $u_{\rm avg}$ is the average fluid velocity, and $k_{\rm f}$ is the thermal conductivity of the fluid. Equation 3.7, the simplified thermal energy equation, is solved subject to the above boundary conditions, yielding

Substrate:

$$T_{\rm s}(x',y') = \frac{L_x}{k}\sum_{n=1}^{\infty} C_n \sinh(\lambda_n r_{xys} y')\sin(\lambda_n x') \tag{3.33a}$$

$$C_n = -\frac{2}{\lambda_n \cosh(\lambda_n r_{xys})}\int_0^1 q''_{\rm s}(x')\sin(\lambda_n x')\mathrm{d}x'$$

Channel:

$$T_{\mathrm{c}}(x',y') = \frac{L_x}{k_{\mathrm{f}}}\sum_{n=1}^{\infty} C_n\left(\mathrm{e}^{\beta_n r_{xyc} y'} + \mathrm{e}^{\beta_n r_{xyc}(2-y')}\right) \times \mathrm{e}^{\frac{a}{2}x'}\sin(\lambda_n x') \tag{3.33b}$$

$$C_n = -\frac{2}{\beta_n\left(1-\mathrm{e}^{2r_{xyc}\beta_n}\right)}\int_0^1 q''_{\mathrm{c}}(x')\mathrm{e}^{\frac{a}{2}x'}\sin(\lambda_n x')\mathrm{d}x'$$

where

$$\lambda_n = n\pi \quad \text{and} \quad \beta_n = \sqrt{\lambda_n^2 + \left(\frac{a}{2}\right)^2}. \tag{3.33c}$$

The heat fluxes $q''_{\mathrm{s}}(x')$ and $q''_{\mathrm{c}}(x')$ at the boundary between the substrate and channel are related by

$$q''_{\mathrm{c}}(x') - q''_{\mathrm{s}}(x') = q''\left(\mathrm{u}\left(x' - \frac{1-r_x}{2}\right) - \mathrm{u}\left(x' - \frac{1+r_x}{2}\right)\right) = q''_{\mathrm{h}}(x') \tag{3.34}$$

where $\mathrm{u}(x)$ is the unit step function and q'' is the average heat flux from the heater. Equation 3.34 states that the heat flux applied to the substrate must be equal and opposite to the heat flux applied to the channel, except over the heater region. The boundary between the substrate and channel is discretized into N regions, with each region assumed to have a width w_i, and a uniform heat flux of $q''_i = q'_i/w_i$. The power per unit length applied to region i is denoted q'_i. The average temperature of region i due to a heat flux applied to region j is

Substrate:

$$T_{ij_{\mathrm{s}}} = \frac{1}{k}\sum_{n=1}^{\infty}\frac{-2\tanh(\lambda_n r_{xys})}{\lambda_n^3} S_{ni}S_{nj}q'_j \tag{3.35a}$$

$$S_{\alpha\beta} = \frac{\cos(\lambda_\alpha x'_\beta) - \cos(\lambda_\alpha x'_{\beta-1})}{x'_\beta - x'_{\beta-1}}$$

Channel:

$$T_{ij_c} = \frac{1}{k}\sum_{n=1}^{\infty}\frac{-2}{\beta_n^5}\left(\frac{1+e^{2r_{xyc}\beta_n}}{1-e^{2r_{xyc}\beta_n}}\right)S_{ni}(\frac{a}{2})S_{nj}(-\frac{a}{2})q_j \tag{3.35b}$$

$$S_{\alpha\beta}(A) = \Big[\lambda_n\left(e^{Ax'_{\beta-1}}\cos(\lambda_\alpha x'_{\beta-1}) - e^{Ax'_\beta}\cos(\lambda_\alpha x'_\beta)\right)$$

$$-A\left(e^{Ax'_{\beta-1}}\sin(\lambda_\alpha x'_{\beta-1}) - e^{Ax'_\beta}\sin(\lambda_\alpha x'_\beta)\right)\Big]/(x'_\beta - x'_{\beta-1})$$

The start and end points of region i are x'_{i-1} and x'_i, respectively. Equation 3.35b is valid for all flow velocities; however, at high velocities the $\exp(ax/2)$ term causes numerical difficulties in the computation. This problem may be avoided by using the following simplifications:

- Thermally fully developed flow exists. The heater used in this simulation is 50 μm wide, while the maximum thermal entry length calculated in Section 3.2.1 is approximately 37 μm. When calculating the effect of heat flux from region j on the temperature of region i, it is assumed that the heat flux in all of the other regions is zero. This is equivilant to assuming region j is a heater in an insulated channel. Therefore, the fully developed temperature profile in the y-direction is assumed to be constant, so

$$\frac{\partial^2 T}{\partial y^2} = 0. \tag{3.36}$$

- Convective transport dominates over conduction at high velocities. Consider an insulated channel with a heater in the center, neglecting temperature differences across the width of the channel. The heat transfered from the heater to the end of the channel via conduction is $q''_c = k\Delta T/(L_x/2)$. The heat transfered due to convective flow is $q''_f = u_{avg}\rho c_p \Delta T$. Therefore, the ratio of heat transfered due to convection versus conduction is

$$\frac{q''_f}{q''_c} = \frac{\rho c_p u_{avg} L_x}{2k_f} = \frac{a}{2} \tag{3.37}$$

Therefore, if $a \gg 1$, then heat transfer due to conduction may be ignored, or

$$\frac{\partial^2 T}{\partial x^2} = 0. \tag{3.38}$$

With these simplifications, the solution to Equation 3.7 simplifies to a constant temperature downstream of the heater:

$$T_{ij_c} = \frac{1}{k_f} \left(\begin{cases} 0 & : \quad i < j \\ \frac{1}{a r_{xyc}} & : \quad i \geq j \end{cases} \right) q'_j \tag{3.39}$$

Once the boundary region has been discretized, Equations 3.35a and 3.35b may be used to generate matrices $\mathbf{H}_s(a, r_x, r_{xys})$ and $\mathbf{H}_c(a, r_x, r_{xyc})$ which relate a heat flux vector to the resulting temperature distribution:

$$\vec{T}_s = \mathbf{H}_s(r_x, r_{xys})\vec{q}_s{}' \quad \text{and} \quad \vec{T}_c = \mathbf{H}_c(a, r_x, r_{xyc})\vec{q}_c{}' \tag{3.40}$$

Equations 3.34 and 3.40 may be combined to obtain the heat flux and hence the temperature at the boundary for a given geometry and flow rate, as shown in Figure 3.3. The most direct way of solving these equations is to set $\vec{T}_c = \vec{T}_s = \vec{T}$, substitue Equation 3.34 ino Equation 3.40 and solve for $\vec{T}$, obtaining

$$\vec{T} = \left(\mathbf{H}_c^{-1} - \mathbf{H}_s^{-1} \right)^{-1} \vec{q}_h{}' \tag{3.41}$$

This solution requires twice inverting matrices which are generally large and may be poorly conditioned. Therefore, extremely high numerical precision is required in this computation. Although Equation 3.41 is found to work well at extremely high precisions, the required precision is excessive. At lower precisions, erroneous oscillations are seen in the q_i values away from the heater, where the values should approach zero. The double matrix inversion may be avoided by using

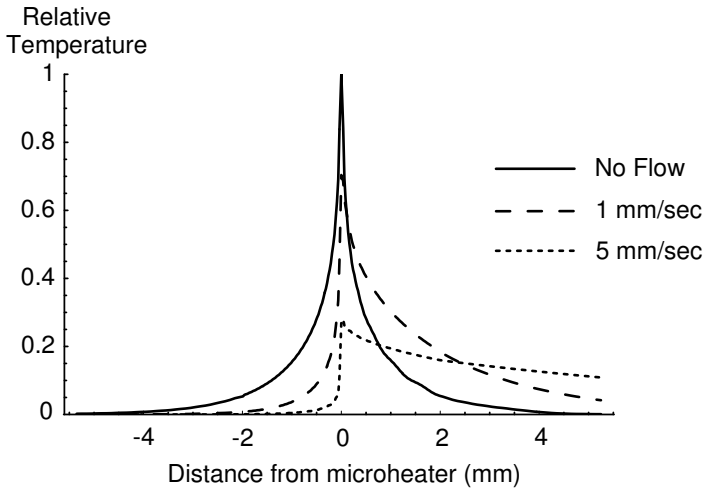

Figure 3.3: Temperature distribution at the microchannel surface as a function of flow velocity, calculated for water flowing over a polymer substrate with $r_x = 0.0005$ and $r_{xy} = 0.032$. The fluid flows from left to right, cooling the left side of the substrate and carrying heat to the right.

optimization subject to physical constraints. Using Equation 3.34, Equation 3.40 may be rewritten

$$\vec{T}_{\mathrm{s}} = \mathbf{H}_{\mathrm{s}}\vec{q}_{\mathrm{s}}{}' \quad \text{and} \quad \vec{T}_{\mathrm{c}} = \mathbf{H}_{\mathrm{c}}\vec{q}_{\mathrm{s}}{}' + \mathbf{H}_{\mathrm{c}}\vec{q}_{\mathrm{h}}{}' \tag{3.42}$$

An objective function may be defined as

$$\begin{aligned} f(\vec{q}_{\mathrm{s}}{}') &= (\vec{T}_{\mathrm{c}} - \vec{T}_{\mathrm{s}}).(\vec{T}_{\mathrm{c}} - \vec{T}_{\mathrm{s}}) \\ &= ((\mathbf{H}_{\mathrm{c}} - \mathbf{H}_{\mathrm{s}})\vec{q}_{\mathrm{s}}{}' + \mathbf{H}_{\mathrm{c}}\vec{q}_{\mathrm{h}}{}') \,.\, ((\mathbf{H}_{\mathrm{c}} - \mathbf{H}_{\mathrm{s}})\vec{q}_{\mathrm{s}}{}' + \mathbf{H}_{\mathrm{c}}\vec{q}_{\mathrm{h}}{}') \end{aligned} \tag{3.43}$$

The resulting heat fluxes should be largest close to the heater and decrease with increasing distance from the heater. A new vector, $\vec{q}_{\mathrm{s}}{}^{*}$ is defined to ensure this, as illustrated in the following example. The heat flux on the region closest to the heater, q_1', is defined as $q_1' = q_1^*$. The next region's heat flux is set to $q_2' = q_1^* - q_2^*$, etc. These relationships may be assembled into a constraint matrix, $\mathbf{A}$, with

$$\vec{q}_{\mathrm{s}}{}' = \mathbf{A}\vec{q}^{*} \tag{3.44}$$

Equation 3.44 is substituted into Equation 3.43, and $f(\vec{q}^{*})$ is minimized subject to the constraint $q_i^* \geq 0$ using Rosen's gradient projection method [67]. This is performed for a variety of flow velocities using water as the fluid, $r_x = 0.0005$ and $r_{xy} = 0.032$. For each velocity, the average heater temperature, $\bar{T}_{\mathrm{h}}$, is divided by the average heater temperature for zero flow velocity. This may be written

$$C_{\mathrm{f}v} \equiv \frac{\bar{T}_{\mathrm{h}}(u_{\mathrm{avg}})}{\bar{T}_{\mathrm{h}}(u_{\mathrm{avg}} = 0)}. \tag{3.45}$$

$C_{\mathrm{f}v}$ has a value of 1.0 at zero velocity and decreases as velocity increases, as shown in Figure 3.4. Linear regression is used to determine a polynomial fit to this data:

$$C_{\mathrm{f}v} = 1 - 0.1276u_{\mathrm{avg}} \tag{3.46}$$

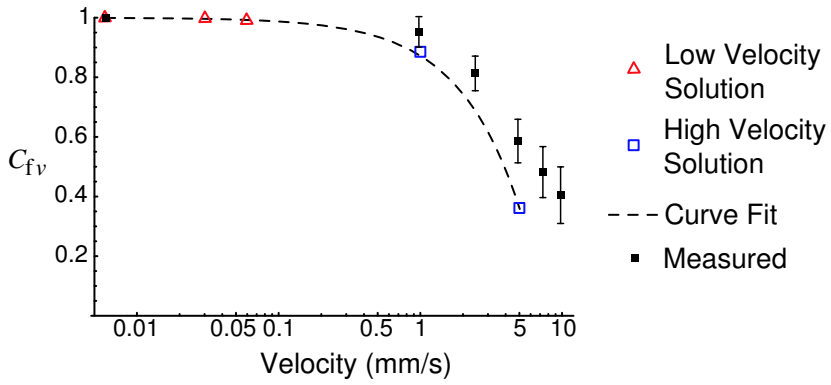

Figure 3.4: Effect of flow velocity on microheater temperature. C_{fv} is a non-dimensionalized measure of temperature.

where u_{avg} has units of mm/sec.

A fluid such as water in the microchannel will have an effect on the temperature of a heater, even if the velocity is zero, due to the different thermal conductivities. To account for this, the above method was used to find the temperature distribution resulting from zero flow velocity for the following two cases. In the first case, the thermal conductivity of the fluid is assumed to be that of water; in the second case, it is assumed to be that of the polymer (i.e. no microchannel is present). The average heater temperature is found for each of these cases. The ratio of the heater temperature with fluid present to the temperature without fluid is defined as C_{f0} and found to be

$$C_{f0} = \frac{\bar{T}_{\text{fluid}}}{\bar{T}_{\text{no fluid}}} = 0.794 \tag{3.47}$$

The parameter C_f may now be written

$$C_f = C_{f0} C_{fv} = 0.794(1 - 0.1276 u_{avg}) \tag{3.48}$$

This parameter is used in Equations 3.12-3.13 and 3.24 to account for the effect of water in a microchannel, and is valid in the range $0 \leq u_{avg} \leq 5$ mm/sec.

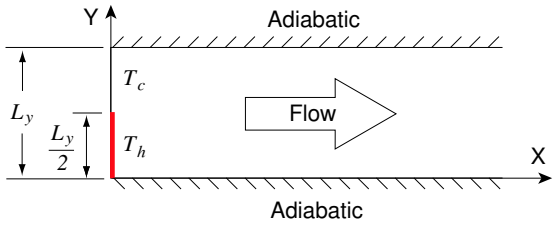

Figure 3.5: Two dimensional model of a hot and cold fluid mixing in a microchannel.

3.3.3 Thermal Diffusion Inside a Microchannel

Thermal diffusion is modeled by considering a hot and a cold fluid which are suddenly brought into contact in a microchannel, as shown in Figure 3.5. Equation 3.7 may be used for all flow velocities, but once again it is convenient to use a simplified version for high velocities. When convection dominates over conduction as the mode of heat transfer in the x-direction, then the $\partial^2 T/\partial x^2$ term may be neglected. These equations are solved subject to the boundary conditions:

$$T(x'=0,y') = \begin{cases} T_h & : \quad 0 \le y' \le \frac{L_y}{2} \\ 0 & : \quad \frac{L_y}{2} < y' \le L_y \end{cases}, \qquad \left.\frac{\partial T}{\partial y}\right|_{y=0} = 0,$$
$$T(x'=L_x,y') = 0, \qquad \left.\frac{\partial T}{\partial y}\right|_{y=L_y} = 0. \tag{3.49}$$

The following non-dimensional parameters are defined:

$$x' = \frac{x}{L_x}, \qquad y' = \frac{y}{L_y},$$
$$r_x = \frac{l_x}{L_x}, \qquad r_{xy} = \frac{L_y}{L_x}, \quad a = \frac{\rho c_p u_{\text{avg}} L_x}{k_{\text{f}}}. \tag{3.50}$$

The resulting temperature distribution in the fluid is

Low Velocity:

$$\begin{aligned} T(x',y') &= \frac{T_h}{2}\left(1+\sum_{n=1}^{\infty} C_n \mathrm{e}^{\frac{a}{2}x'}\left(\mathrm{e}^{\beta_n x'}-\mathrm{e}^{\beta_n(2-x')}\right)\cos(\lambda_n y')\right) \quad (3.51a)\\ C_n &= \frac{4(-1)^{n+1}}{\lambda_n(1-\mathrm{e}^{2\beta_n})},\\ \lambda_n &= (2n-1)\pi, \quad \beta_n = \sqrt{\left(\frac{a}{2}\right)^2+\left(\frac{\lambda_n}{r_{xy}}\right)^2} \end{aligned}$$

High Velocity:

$$\begin{aligned} T(x',y') &= \frac{T_h}{2}\left(1+\sum_{n=1}^{\infty} C_n \exp\left(-\left(\frac{\lambda_n}{r_{xy}}\right)^2\frac{x'}{a}\right)\cos(\lambda_n y')\right) \quad (3.51b)\\ C_n &= \frac{4(-1)^{n+1}}{\lambda_n},\\ \lambda_n &= (2n-1)\pi. \end{aligned}$$

As $x \to \infty$ the temperature in the channel approaches a uniform value of $T_h/2$. The average temperature difference between the hot and cold sides of the channel, normalized with respect to the far-field value of $T_h/2$, is denoted $\Delta\bar{T}$ and defined as

$$\Delta\bar{T} = \frac{4}{T_h L_y}\int_0^{L_y/2}\left(T(x',y')-\frac{T_h}{2}\right)\mathrm{d}y. \quad (3.52)$$

Evaluating Equation 3.52 yields

Low Velocity:

$$\Delta\bar{T}(x') = 8\sum_{n=1}^{\infty}\mathrm{e}^{\frac{a}{2}x'}\left(\frac{\mathrm{e}^{\beta_n x'}-\mathrm{e}^{\beta_n(2-x')}}{\lambda_n^2(1-\mathrm{e}^{2\beta_n})}\right), \quad (3.53a)$$

High Velocity:

$$\Delta\bar{T}(x') = 8\sum_{n=1}^{\infty}\frac{1}{\lambda_n^2}\exp\left(-\left(\frac{\lambda_n}{r_{xy}}\right)^2\frac{x'}{a}\right). \quad (3.53b)$$

The distance required for the fluid to come within a given percent of equilibrium may now be quantified by setting $\Delta\bar{T}$ equal to the given percentage

and solving for x'. In this manor, the diffusion distance d is defined here as the distance required for the fluid to reach 95% of equilibrium, and is calculated by numerically solving Equation 3.53 for d:

$$0.05 = \Delta\bar{T}(d) \tag{3.54}$$

The diffusion distance is calculated via both methods, and the results are shown in Figure 3.6. Note that at lower velocities, the high velocity solution deviates significantly from the low velocity solution; it is evident that in this region, the neglection of the $\partial^2 T/\partial x^2$ term is not reasonable.

Both the low and high velocity models assume a uniform velocity profile within the channel. However, the velocity is actually zero at the channel walls and parabolically increases to a maximum value a the center of the channel. Finite Element Analysis (FEA) was performed on a three-dimensional model of the system, shown in Figure 3.12a, to account for the effects of the parabolic velocity profile. The results are shown in Figure 3.6. At higher velocities, the more accurate FEA simulation begins to diverge from the analytical models, due to the effect of the velocity profile.

The previous results may be readily applied to species concentrations in a binary mixture. Consider a mixture of species A and B in the microchannel illustrated in Figure 3.5. In this case, the two incoming streams have different concentrations of species A. If C_{A} is the molar concentrations of species A, and D_{AB} is the binary diffusion coefficient, then the governing PDE for species diffusion is

$$\frac{\partial^2 C_{\mathrm{A}}}{\partial x^2} + \frac{\partial^2 C_{\mathrm{A}}}{\partial y^2} = \frac{u_{\mathrm{avg}}}{D_{\mathrm{AB}}}\frac{\partial C_{\mathrm{A}}}{\partial x}, \tag{3.55}$$

This is identical in form to Equation 3.7, with boundary conditions of the same form. The solutions are therefore the same, except T is replaced by C_{A} and a is

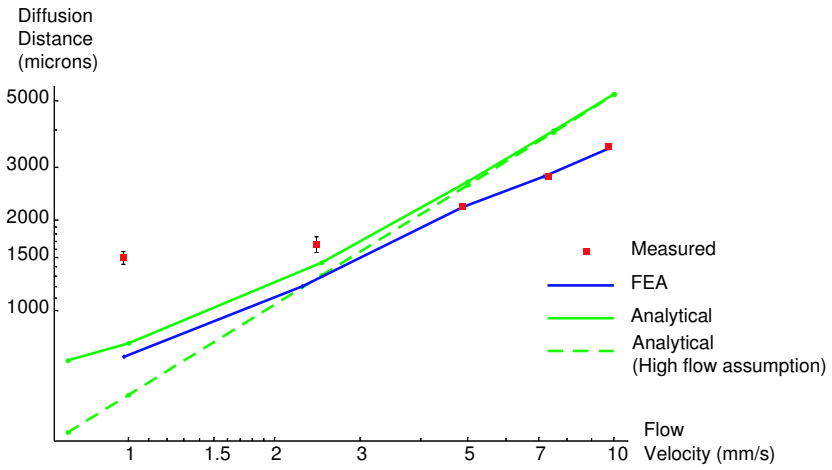

Figure 3.6: Thermal diffusion in a microchannel. The diffusion distance is the distance required for the hot and cold fluid to reach 95% equilibrium.

redefined as $a = u_{\text{avg}}/D_{\text{AB}}$.

3.3.4 Transient Model

The length of time for a polymer system with non-isolated heaters to reach thermal equilibrium is of considerable importance for applications such as PCR, bubble pumping, etc. A one-dimensional model is considered which consists of a polymer substrate maintained at $T = 0$ on one side and exposed to a heat flux, q'', on the other side. The substrate is assumed to start at a uniform temperature of zero. This model may be used to approximate the heat flux due to a heater, metal deposition, or lithographic exposure. The boundary and initial conditions may be written:

$$T(x = 0, t) = 0, \qquad -k \left.\frac{\partial T}{\partial x}\right|_{x=L} = q'', \quad \text{and} \quad T(x, t = 0) = 0 \tag{3.56}$$

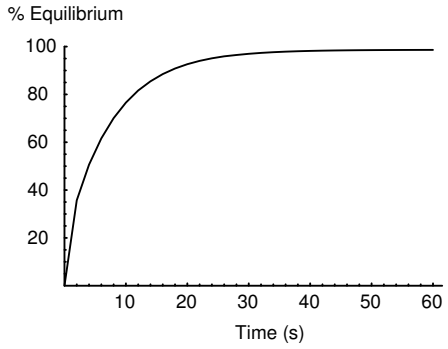

Figure 3.7: Transient respone for a 1/16" thick polycarbonate wafer subjected to a uniform heat flux. 95% of equilibrium is achieved in 24 seconds.

The governing equation

$$\frac{\partial^2 T}{\partial x^2} = \frac{1}{\alpha}\frac{\partial T}{\partial t}, \qquad \alpha = \frac{k}{\rho c_p} \tag{3.57}$$

is solved subject to the above boundary and initial conditions using Green's functions. The result is

$$T(x', t') = \frac{Lq''}{k} \sum_{m=1}^{\infty} \frac{2}{\beta_m^2} \left(1 - \mathrm{e}^{-\beta_m^2 t'}\right) (-1)^{m+1} \sin(\beta_m x') \tag{3.58}$$

where t' is the Fourier number, a non-dimensional time:

$$t' = \mathrm{Fo} = \frac{\alpha t}{L^2} \tag{3.59}$$

The temperature on the surface subjected to the heat flux is divided by the steady state temperature, $T = Lq''/L$, to determine the percentage of equilibrium, $\delta(t')$, which has been achieved by time t':

$$\delta(t') = \sum_{m=1}^{\infty} \frac{2}{\beta_m^2} \left(1 - \mathrm{e}^{-\beta_m^2 t'}\right) \tag{3.60}$$

The result is plotted in Figure 3.7.

3.4 Experimental Validation

3.4.1 Temperature Measurements

The preceeding models are verified using the polycarbonate microfluidic device described in Section 2.7.1. The device, shown in Figure 3.8, consists of a T-intersection of three microchannels with a 5 × 5 array of RTDs at the intersection. Fluid flows in from the top and bottom channels, mixes, and flows out to the left. The input channels are 310 μm wide at the top and 495 μm wide at the base, while the main channel is 545 mum wide at the top and 731 mum wide at the base. All channels are 107 μm deep. A microheater in the top channel heats the fluid, which then combines with the room temperature fluid from the bottom channel. The RTD array allows measurement of the thermal diffusion which occurs when the two fluid streams are brought into contact. The temperature of the microheater is estimated by measuring its resistance change. The measured heater temperature and temperature distribution can be compared to the compact microheater model described above.

The sensors are wired in parallel wheatstone bridge circuits, as shown in Figure 2.15. The change in output voltage for each sensor relative to its room temperature output voltage is expressed as ΔV_{ij}. Given this voltage change, Equation 2.27 may be used to find the corresponding temperature change:

$$\Delta T_{ij} = \frac{(R_{\mathrm{b}i} + R_{\mathrm{s}i})^2}{R_{\mathrm{b}i} R_{\mathrm{s}i} \alpha V_{\mathrm{in}}} \Delta V_{ij} \tag{3.61}$$

where $R_{\mathrm{s}i}$ and $R_{\mathrm{b}i}$ are the resistances of the sense and balance resistors, given in Table 3.3. V_{in} is the voltage applied to the bridge (0.5 V), and α is the TCR value of the titanium layer, found during calibration to be 0.0017 $^{\circ}\mathrm{C}^{-1}$.

The voltage applied to the microheater, the microheater current, the

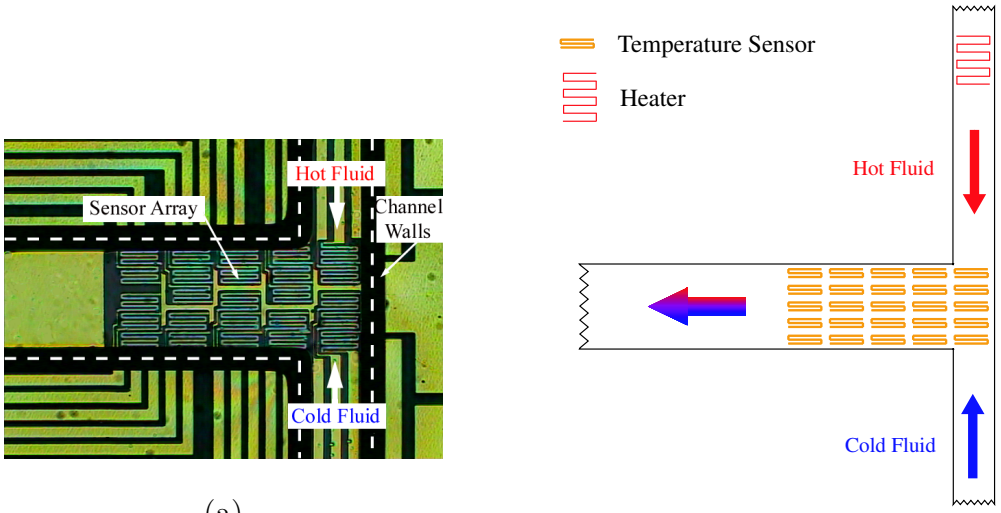

(a) (b)

Figure 3.8: Microheater/RTD array used for validation. (a) Photograph of RTD array and microchannel junction. (b) System Schematic.

	R_{sij} (Ω)					R_{bij} (Ω)				
$j =$	1	2	3	4	5	1	2	3	4	5
$i = 1$	1605	1451	1506	1517	1435	2130	2272	2322	2052	2308
$i = 2$	1599	1533	1389	483	1166	2169	2093	2158	2099	2783
$i = 3$	1639	1574	1035	1481	1463	2448	2231	2216	2473	2552
$i = 4$	1551	1495	1507	1063	1364	2256	2136	2464	2190	2425
$i = 5$	1548	1485	1496	1006	1291	2044	2052	2492	2149	2174

Table 3.3: Resistances of the sense and balance resistors.

	Mean (μV)					Noise (μV)				
$j =$	1	2	3	4	5	1	2	3	4	5
$i = 1$	299	310	328	355	377	14	15	17	32	16
$i = 2$	282	303	311	201	286	15	16	12	12	29
$i = 3$	262	284	234	295	308	12	12	76	12	12
$i = 4$	251	268	273	247	271	10	9	12	10	12
$i = 5$	247	256	268	238	272	8	6	5	4	5

Table 3.4: Voltage change, ΔV_{ij}, and noise for each sensor.

voltage applied to the RTD array, and the voltage outputs of the RTD bridges are measured with an Agilent 34970A data aquisition/switch unit. Measurement scans are performed every 15 seconds. After each change in heater power or fluid velocity, two minutes are allowed for equilibrium to be reached. Data is then aquired for seven minutes, providing 28 voltage measurements which are averaged. The noise level is considered to be the root mean square of these points. The sensor voltage outputs, ΔV_{ij}, for a heater power of 2.45 W/m and zero fluid velocity are given in Table 3.4 as an example which will be compared to the micro heater model described previously. Table 3.4 illustrates the performance of both the microfluidic system and the measurement apparatus. The noise for most sensors is less than 15 μV, which approaches the $\pm 5\mu$V accuracy of the voltage meter.

The room temperature resistance of the heater is 57.0 Ω, and the TCR was found during calibration to be 0.0017 $^{\circ}\mathrm{C}^{-1}$. In this measurement example, the change in resistance of the heater was 1.31 Ω, with a noise level of 0.01 Ω. This corresponds to a heater ΔT of 13.5 °C and noise level of 0.1 °C. The temper-

	Mean (°C)					Noise (°C)				
$j =$	1	2	3	4	5	1	2	3	4	5
$i = 1$	1.43	1.53	1.62	1.71	1.87	0.069	0.076	0.083	0.16	0.077
$i = 2$	1.36	1.46	1.54	1.55	1.61	0.072	0.077	0.057	0.091	0.16
$i = 3$	1.28	1.38	1.27	1.48	1.56	0.058	0.059	0.41	0.059	0.062
$i = 4$	1.23	1.30	1.36	1.32	1.38	0.047	0.043	0.059	0.055	0.062
$i = 5$	1.18	1.24	1.34	1.29	1.37	0.037	0.030	0.028	0.023	0.025

Table 3.5: Temperature readings and noise level for each sensor.

ature change of each senor is calculated with Equation 3.61, and shown in Table 3.5. The average noise level of the sensor readings shown in Table 3.5 is 0.065 °C, which is comparable to measurements made with commercially available bulk thermocouples. The noise of sensor $3-3$ is not counted in this noise average since it appeared to have contact problems, resulting in erroneous readings and abnormally high noise levels. Table 3.5 also demonstrates the resolution of the RTD array. It is able to clearly discern a temperature profile in which the difference between the maximum and minimum temperature is 0.7 °C.

3.4.2 Compact Microheater Model

The heater and sensor data given above may be used to verify the thin film heater model (Equations 3.25, 3.26, and 3.29) and the flow effect model (Equation 3.46). The following example illustrates the use and accuracy of this compact model.

The layout and dimensions are shown in Figure 3.9 and Table 3.6. The wafer is circular, with a diameter of 10 cm. Since the thin-film heater model

Parameter	Value	Units
L_x, L_z	10	cm
L_y	1/8	inch
l_x	25	μm
l_z	250	μm
N	21	
s	25	μm
k	0.19	W m^{-1} °C^{-1}

Non-dimensional Parameter	Value
r_{xy}	0.03175
r_x	0.00025
r_z	0.002
r_a	10
r_h	1
N	21

Table 3.6: Dimensions of polycarbonate microfluidic device used for model verification.

assumes a rectangular domain, the actual device does not conform exactly to this model. However, since the domain is much larger than the heaters, the diameter may still be used as the characteristic length without introducing any significant error. Both the top and bottom wafer are 1/16" thick, so the total thickness of the device is 1/8". The serpentine heater has 21 segments, each of which is 250 μm by 25 μm. The non-dimensional paramteres required for the model are also shown in Table 3.6. The distance from the coordinate system origin to the center of each sensor is shown in Table 3.7. The values in Table 3.7 are normailized to the wafer length, L_x, as defined in Equation 3.16.

The terms used in Equation 3.26 amd 3.27 are computed and shown in Table 3.8. C_{bc} is computed using Equation 3.25 for the closest values of r_{xy} given in Table 3.1. This yields $C_{\text{bc}} = 0.106$ for $r_{xy} = 0.01$ and $C_{\text{bc}} = 0.0954$ for $r_{xy} = 0.05$. Linear interpolation between these two points is used to approximate the value of C_{bc} for $r_{xy} = 0.03175$. Similarly, $\sigma = 81.4$ for for $r_{xy} = 0.01$ and

	$j=1$	$j=2$	$j=3$	$j=4$	$j=5$
$i=1$	0.0552	0.0536	0.0525	0.0517	0.0515
$i=2$	0.0571	0.0556	0.0544	0.0537	0.0535
$i=3$	0.0590	0.0575	0.0564	0.0557	0.0555
$i=4$	0.0609	0.0594	0.0584	0.0577	0.0575
$i=5$	0.0628	0.0614	0.0603	0.0597	0.0595

Table 3.7: Non-dimensional distance from heater origin to the center of each sensor.

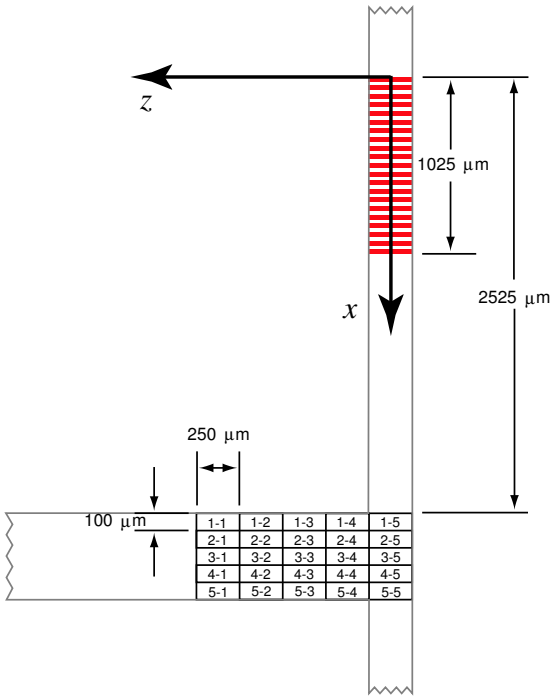

Figure 3.9: Layout of the validation device.

Term	Value
C_{bc}	0.0975
σ	34.6
C_{s}	27.0
$\bar{C}_{\mathrm{s}}$	18.1
C_{f}	0.794

Table 3.8: Values for the terms used in the compact model.

$\sigma = 23.6$ for $r_{xy} = 0.05$, yielding $\sigma = 34.6$ for $r_{xy} = 0.03175$. The value of C_{f} at zero flow velocity is computed using Equation 3.48. The values of $\bar{C}_{\mathrm{s}}$ and C_{s} are calculated using Equations 3.29 and 3.30, respectively. Finally, Equation 3.26 is used to calculate the heater temperature predicted in Figure 3.10a, and Equation 3.27 along with the values given in Table 3.7 are used to compute the predicted temperatures plotted in Figure 3.10a. The model predicts the average heater temperature within 7 % of the measured value, while the sensor temperatures are predicted with an average error of 8%.

The measured effect of fluid velocity on microheater temperature is shown in Figure 3.4. For each velocity, 25 different measurements were performed. The standard deviation of these measurements is reflected in the error bars of Figure 3.4. The measurements and predictions agree by definition at zero velocity, but the measured values of $C_{\mathrm{f}v}$ at higher velocities are larger than predicted. This is due to the fact that the flow model assumes a single heater, and the heater used for measurements is a serpentine heater. The first few segments of the serpentine heater cool off as fluid passes over them in the same manor as a single heater. However, by the time the fluid reaches the latter segments of the heater, it is

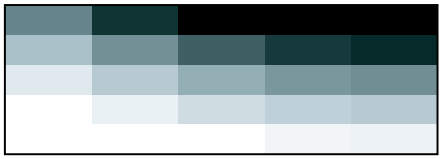

(a) Heater Temperature = 14.2°C

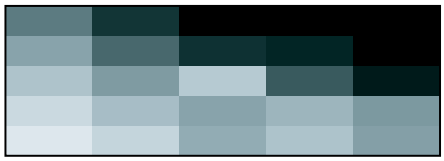

(b) Heater Temperature = 13.5°C

Figure 3.10: Steady-state temperature distribution in validation device without fluid flow for a heater power per unit length of 2.45 W/m. (a) Model prediction of heater temperature and sensor readings. (b) Measured values of heater temperature and sensor readings.

already close to thermal equilibrium with the heater, so little cooling occurs in these segments. Therefore, the average temperature drop of the whole serpentine heater is significantly less than for a single heater.

3.4.3 Thermal Diffusion

The RTD array very clearly shows the effects of fluid velocity on the temperature profile at the intersection. This effect is plotted for a heater power of 2.45 W/m in Figure 3.11. The diffusion distance is defined here in the same manor as in the diffusion model, Section 3.3.3. That is, the distance from the start of the sensor array at which 95% of equilibrium is achieved. The measured values are plotted in Figure 3.6. Each data point in Figure 3.6 represents the mean of 25 measurements, while the standard deviation is reflected in the error bars. At higher velocities, the measurements correspond well with the FEA simulation. However, at low velocities, the measured results diverge significantly from the predictions. This is most likely due to the trapezoidal geometry of the real microchannels, shown in Figure 3.12. The diffusion distance increases with channel width, and the channel is wider at the sensor plane than accounted for in the predicted result (which assumes a rectangular channel). In addition, the hot and cold fluid enter from the sides of the main channel, not the back as assumed in the model. This will further increase the diffusion distance, by at least the width of the entrance channels (which are also trapazoidal, and hence larger at the sensor plane). These effects are most evident at low flow rates, when the predicted diffusion distance is close to the widths of the microchannels. However, as the diffusion distance becomes much larger than the microchannel widths, the measurements match the predictions more closely.

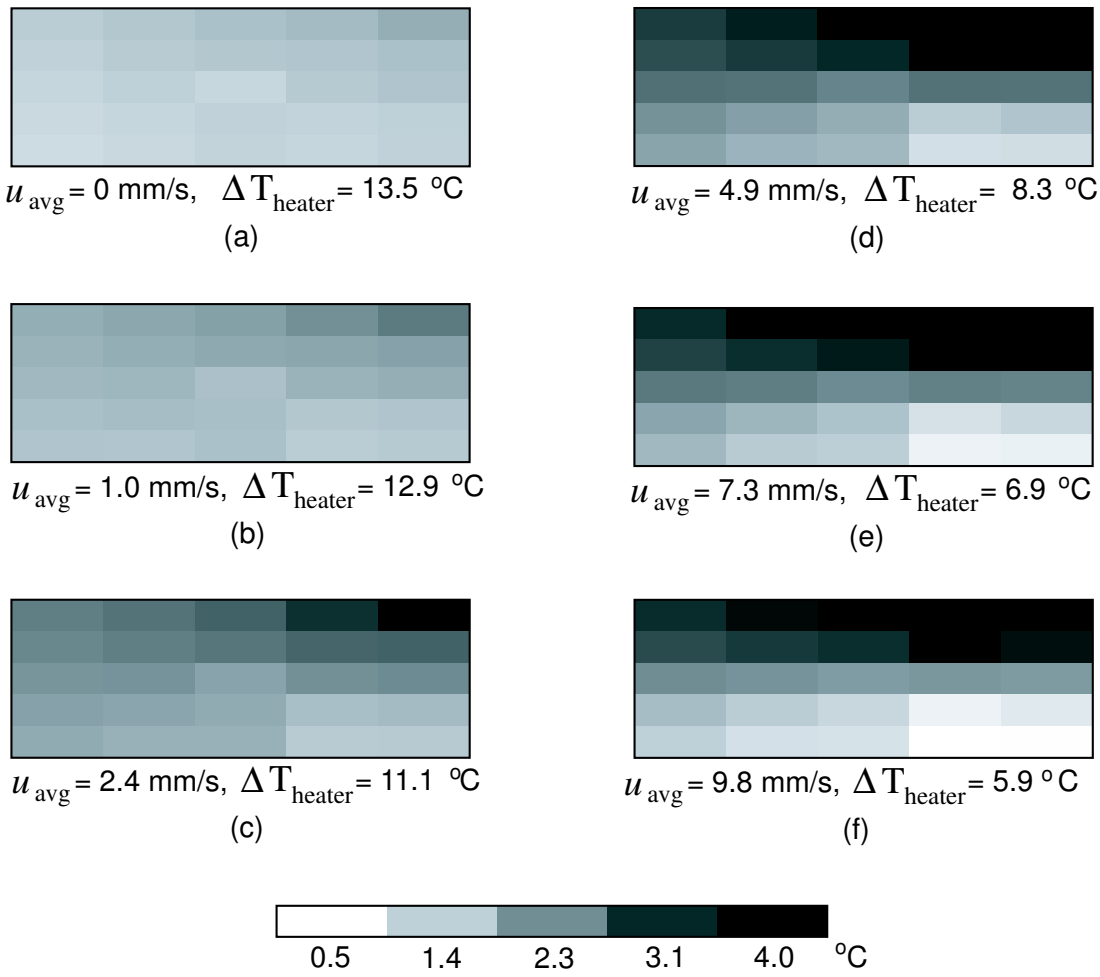

Figure 3.11: Temperature distribution measured by the RTD array for various fluid velocities. The same heater power, 2.45 W/m, is maintained for all flow velocities.

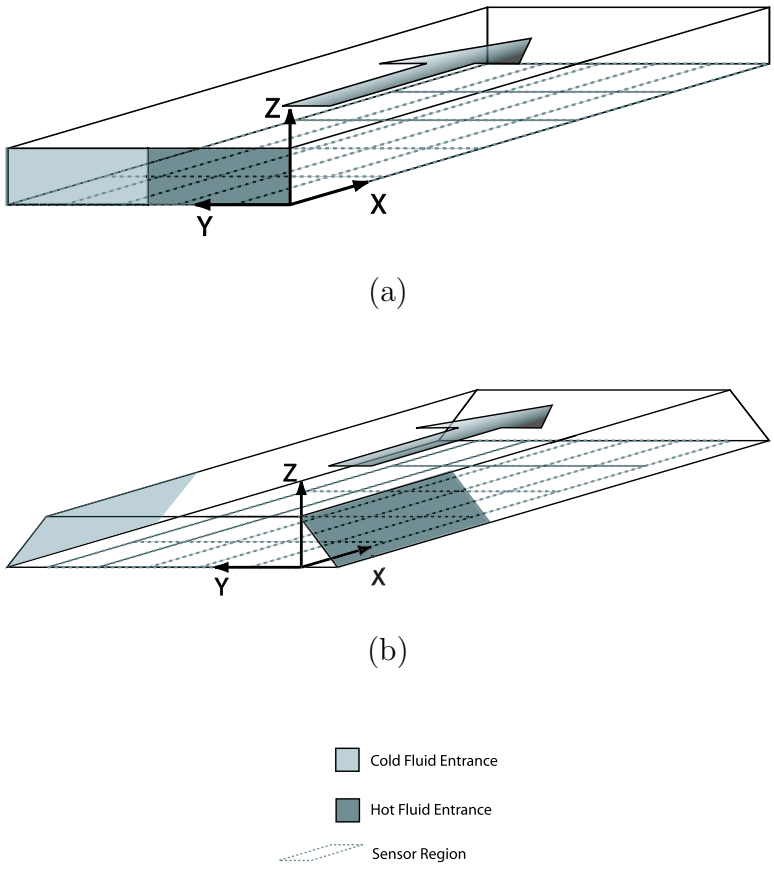

Figure 3.12: (a) Geometry used for three-dimensional FEA flow model. (b) Geometry of actual device.

Chapter 4

Temperature Gradient Gel Electrophoresis System

An integrated system combining polymer microfluidics and modular electrothermal heater arrays has been developed for performing Temperature Gradient Gel Electrophoresis (TGGE). A detailed thermal model for the separation platform is presented, and experimental validation demonstrates less than 0.2°C variation between desired and measured spatial temperature gradients. The design, simulation, and separation performance using 140 base pair DNA fragments containing a single mutation is discussed. [1]

4.1 Introduction

4.1.1 Mutation Detection Methods

The movement toward functional genomic studies in the post-genomic era has placed an emphasis on the analysis of gene variants in human populations for the purpose of disease diagnosis, prognosis, and management. In order to improve upon existing mutation analysis technologies, the rapid, inexpensive, and accurate identification of DNA sequence heterogeneity has been recognized

[1]The DNA and reagent preparation, detection system design and operation, and electrophoretic separations were the work of Jesse Buch.

as being of major importance.

In their current states, mutational analysis via DNA sequencing and DNA microarrays remain cost intensive. Furthermore, DNA sequencing endures difficulty in detecting heterozygotes, while microarray DNA chips continue to suffer from poor accuracy and sensitivity. Nevertheless, DNA sequencing continues to be the accepted gold standard for mutation identification. As a result, more rapid and inexpensive mutation screening techniques are being sought to decrease the sequencing load for identifying mutations. The potential of microfluidic devices for low cost and extremely rapid analyses makes these platforms amenable to this endeavor.

Traditionally, mutation screening is primarily performed in the slab gel format employing a variety of methods. Compared to capillary and microchip electrophoresis, slab gel methods continue to suffer from intensive labor requirements, slow analysis speed, and poor reproducibility. The most prevalent slab gel-based mutation screening techniques include heteroduplex analysis (HDA) [68] , single-strand conformation polymorphism (SSCP) [69] , and denaturing gradient gel electrophoresis (DGGE) [70] . Of these methods, DGGE has shown the most promise as it can handle longer DNA fragments, is less time consuming, and its mutation detection sensitivity can theoretically reach 100%. However, irreproducibility in preparing identical chemical denaturant gradient gels makes implementation difficult.

Temperature gradient gel electrophoresis (TGGE) is analogous to DGGE and has been successfully demonstrated in slab gel [71] and capillary [72, 73] formats. TGGE employs the same mode for mutation detection as DGGE, but does so by implementing a thermal denaturing gradient instead of a chemical one. In

TGGE, the thermal denaturing gradient can be applied temporally [71, 72] or spatially [73] . TGGE provides the same theoretical sensitivity as DGGE, while being much easier to implement and offering much better reproducibility. Furthermore, TGGE is significantly easier to implement in a miniaturized format using microfluidic technology, as described in this paper.

4.1.2 Mutation Detection with TGGE

TGGE is able to reveal the presence of sequence heterogeneity in the following manor. A sample to be screened may contain DNA fragments of identical size but different sequences; the simplest case is shown in Figure 4.1a where only one base pair has changed from A-T to G-C or vise versa. This mixed sample is heated until all fragments completely melt, separating into single stranded DNA (ssDNA) molecules. The sample is next cooled to allow the fragments to recombine into double stranded DNA (dsDNA), forming the original homoduplexes as well as two heteroduplexes, illustrated in Figure 4.1a. This sample is then electrophoretically moved through a temperature gradient. At low temperatures, all fragments are unmelted and have very similar electrophoretic mobilities (Figure 4.1b). As the temperature increases, the heteroduplexes partially melt which lowers their electrophoretic mobility. The DNA fragments now begin to separate into two bands corresponding to homoduplexes and heteroduplexes. If temperature is increased further, the homoduplexes partially melt and the fragments all move with the same velocity, but in distinct bands. If all of the fragments in the original sample were identical in sequence, then no heteroduplexes would be present after the first step (Figure 4.1a), and only one band would be observed after the separation. The GC clamp is a region composed entirely of G-C base

pairs, which have a significantly higher melting temperature than the rest of the fragment. This prevents any of the fragments from completely melting into ssDNA, since ssDNA has a much higher electrophoretic mobility than any of the homoduplexes or heteroduplexes.

4.1.3 Integrated Microsystem for TGGE

The integrated temperature control system presented here is capable of providing the thermal gradient required for accurate TGGE analysis in many multiplexed channels while consuming approximately 0.5W. This power requirement is an improvement of at least 25 and 300 times compared to external temperature control systems reported in the literature for microchip [74] and capillary [72] electrophoresis formats, respectively. The most important difference between generating a spatial temperature gradient with microheaters versus the previous approaches is that previous approaches require a heat source and a heat sink to generate a gradient, i.e. heat must continuously flow from the source to the sink. Shaped microheaters allow a spatial temperature gradient to be maintained using only a source. This requires much less power, but presents a significant design challenge: the heater must provide a non-uniform power distribution which creates the desired spatial temperature gradient. The design of this heating platform and its ability to perform DNA mutational analyses by TGGE in an integrated microfluidic system is presented.

4.2 System Design

An overview of the system is shown in Figure 4.2 The system consists of two separable components: a polycarbonate (PC) wafer with microchannels, and

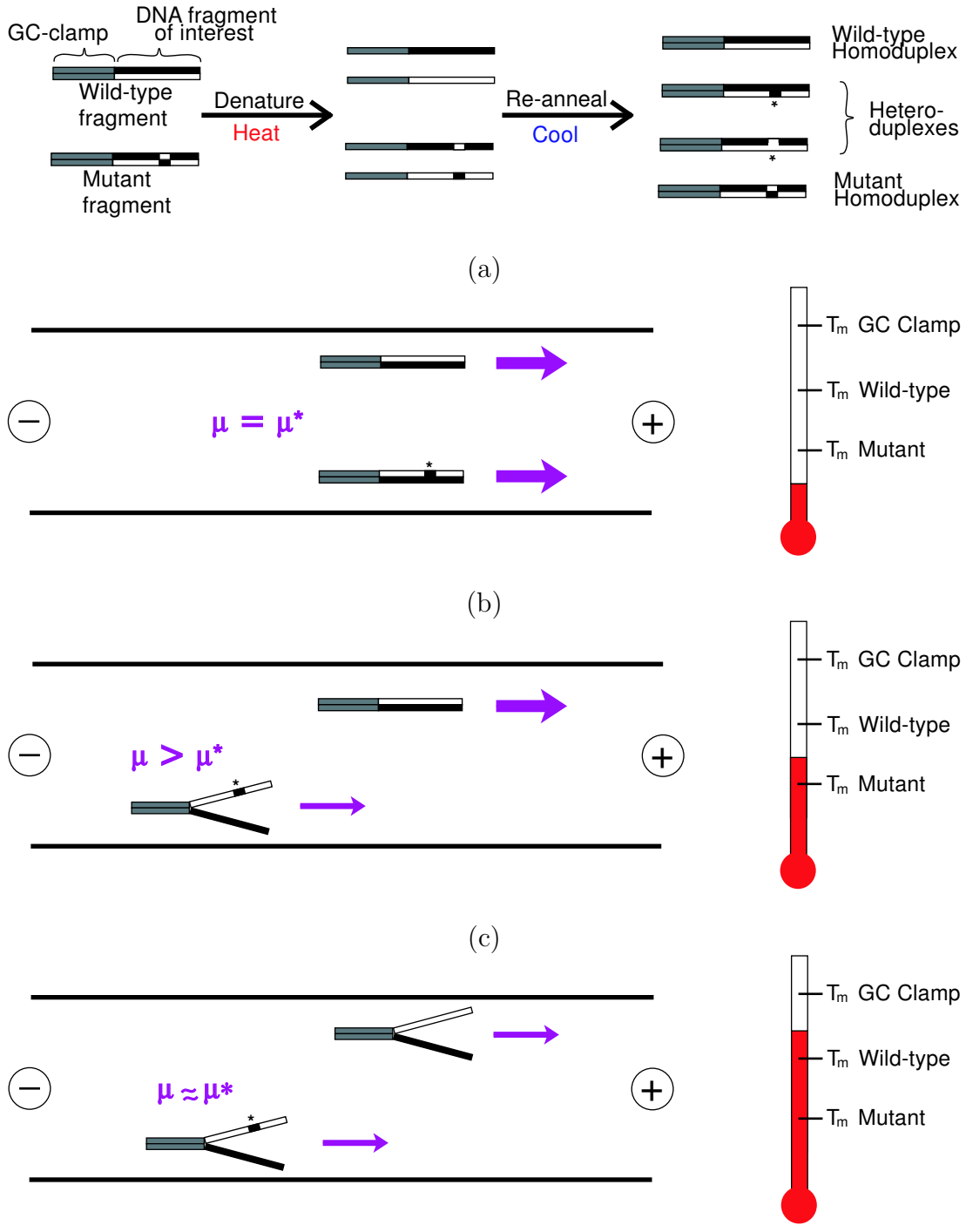

Figure 4.1: Detection of mutations using TGGE. (a) Creation of heteroduplexes . (b) All fragments unmelted. (c) Homoduplexes unmelted, heteroduplexes partially melted. (d) All fragments partially melted.

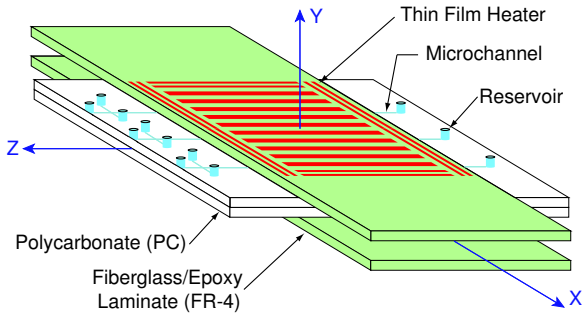

Figure 4.2: TGGE system. The polycarbonate channel wafer (clear) is located between two identical heater wafers (shaded).

a pair of identical FR-4 boards with micro-heaters and temperature sensors. FR-4 is a woven glass fiber/epoxy laminate which is commonly used as a substrate for printed circuit boards. This allows the channels to be disposable while reusing the heaters. A cross sectional view of the TGGE platform is shown in Figure 4.3. The channels are made with an anisotropically etched silicon mold which is hot embossed into a PC wafer. The microchannels are sealed by thermally bonding with another PC wafer containing access ports. The microheaters are patterned on one side of each FR-4 board, and Resistive Temperature Detectors (RTDs) are patterned on the other side. The microheaters and RTDs are fabricated by evaporating an adhesion layer of titanium (1000 Angstroms) on both sides of the FR-4 board, followed by a layer of gold (1000 Angstroms for the RTDs and 6000 Angstroms for the microheaters). The boards are assembled as shown in Figure 4.2 - 4.3, with the PC channel wafer sandwiched between the two identical FR-4 heater wafers. The heaters are located on the outside of the stack and the sensors are located midway between the heaters and channels, thereby improving the temperature measurement accuracy. The completed system is shown in Figure 4.4

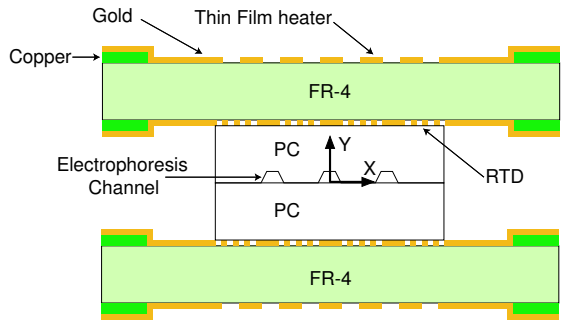

(a)

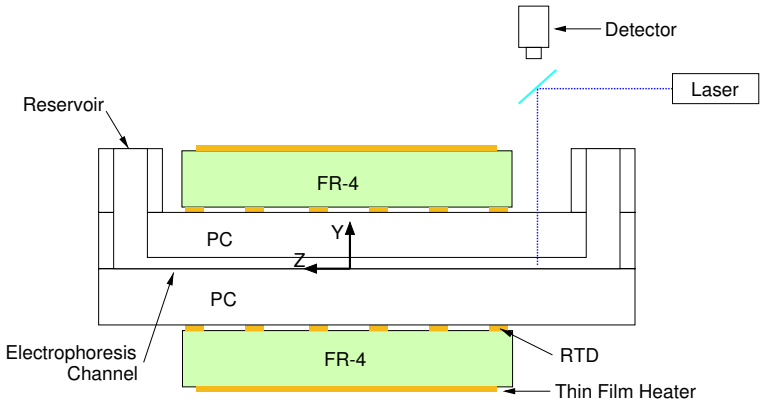

(b)

Figure 4.3: Cross section of the TGGE system (a) perpendicular to the microchannels and (b) parallel to the microchannels. The thin film heaters are located on the top and bottom surfaces, the micro-channels are located in the center, and the thin film sensors are located midway between the heaters and channels.

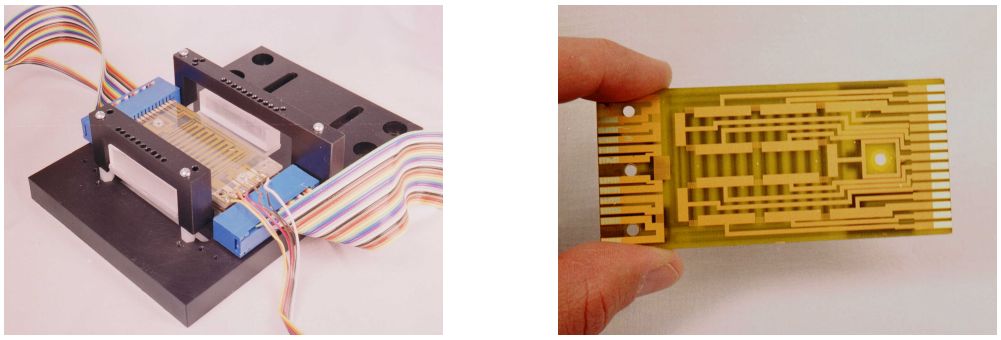

(a) (b)

Figure 4.4: (a) Assembled TGGE system. (b) Thin film sensors on heater wafer.

The channel wafer and heater wafers all extend beyond the heated region, as shown in Figures 4.5. A significant amount of heat will be lost through these extended surfaces. If a uniform heat flux is applied across the heated region, the temperature at the edge of the heated region will be much lower than the temperature at the center. To compensate for this, the heaters must provide a larger heat flux at the edges of the heated region. The temperature sensors are not located in the same plane as the channels, as shown in Figure 4.3. A uniform temperature distribution in the sensor plane will result in a non uniform temperature distribution in the channel plane, due to the heat loss occurring through the ends of the channel wafer. Therefore, a thermal model of the system is needed both for design and interpretation of the sensor measurements. We have developed an analytical model, which can be easily re-evaluated for different geometries.

4.2.1 Thermal Model

The heater/channel system is shown in Figure 4.2. The system is symmetric about the yz plane, and is approximated as being symmetric about the xz and xy

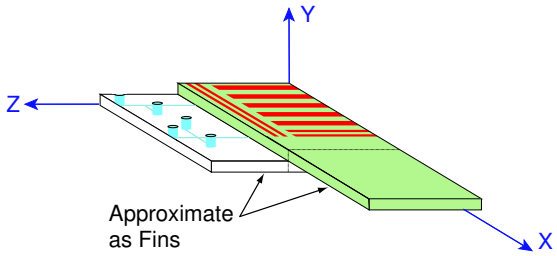

Figure 4.5: Reduced model of the TGGE system showing the simplifications made by symmetry assumptions.

planes. The convection coefficients on the top and bottom surfaces are slightly different, generating a small asymmetry about the xz plane, but this effect is ignored. The heaters generate a temperature gradient in the z direction, so the temperature on one side of the xy plane is slightly higher than the temperature on the other side. However, the target gradient is $3°C$, which is approximately 6% of the total temperature change. Therefore, the temperature gradient can initially be ignored in the model. The simplified model is shown in Figure 4.5. The thermal conductivities of the polycarbonate and FR-4 are 0.19 and 0.25 W/mK, respectively. Since the thermal conductivities are reasonably close, the two materials are approximated as a single material with a thermal conductivity of 0.22 W/mK.

The extended surfaces shown in Figure 4.5 can be approximated using a one dimensional fin approach as follows. A one dimensional fin is shown in Fig 4.6. The convection coefficient on the top, bottom and sides is denoted h_s, while the convection coefficient on the tip is denoted h_t. The governing equation is [65]

$$\frac{d^2T}{dx^2} - \frac{h_s P}{kA_c}T = 0, \tag{4.1}$$

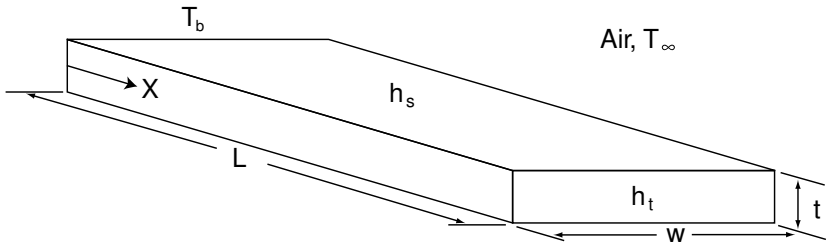

Figure 4.6: One dimensional fin. The base temperature (at $T(x = 0)$) is held at T_b, while the rest of the fin is exposed to convection.

where k is thermal conductivity, P is the perimeter, and A_c is the cross-sectional area. The general solution is

$$T(x) = C_1 e^{mx} + C_2 e^{-mx}, \tag{4.2}$$

where

$$m = \sqrt{\frac{h_s P}{k A_c}} = \sqrt{\frac{2h_s}{k}\left(\frac{1}{w} + \frac{1}{t}\right)}. \tag{4.3}$$

Applying the boundary conditions,

$$\begin{aligned} T(0) &= T_b \\ h_t T(L) &= -k\frac{dT}{dx}\bigg|_{x=L}, \end{aligned} \tag{4.4}$$

the temperature distribution in the fin found to be

$$T(x) = \frac{\frac{h_t}{km}\sinh(m(L-x)) + \cosh(m(L-x))}{\frac{h_t}{km}\sinh(mL) + \cosh(mL)} T_b. \tag{4.5}$$

The heat flux through the base is

$$q_b'' = km\left(\frac{\frac{h_t}{km}\cosh(mL) + \sinh(mL)}{\frac{h_t}{km}\sinh(mL) + \cosh(mL)}\right) T_b = h_f T_b, \tag{4.6}$$

where

$$h_f = km\left(\frac{\frac{h_t}{km}\cosh(mL) + \sinh(mL)}{\frac{h_t}{km}\sinh(mL) + \cosh(mL)}\right). \tag{4.7}$$

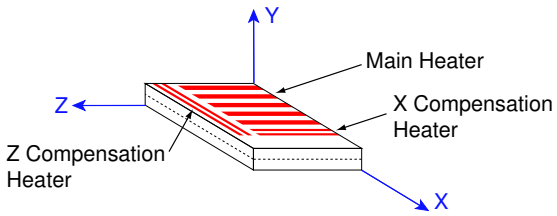

Figure 4.7: Simplified model of the TGGE system. Extended surfaces have been removed and replaced with an equivalent convection coefficient, and the whole system is approximated as one material.

If the fin is removed and the exposed base area is assumed to have an average convection coefficient of h_f, the heat flux through this area will be

$$q'' = h_f T_b, \tag{4.8}$$

which is identical to Eqn. 4.6. Therefore, a one dimensional fin may be approximated as an average convection coefficient, given by Eqn. 4.7. This approximation will only be valid if the temperature variations across the surface exposed by removing the fin are small compared to the temperature variations along the length of the fin. This condition will hold for a thin plate, as is the case in Figure 4.5.

With the fins removed and a single material assumed, the system in Figure 4.5 is reduced to a simple rectangular volume shown in Figure 4.7. The effects of the heater are modeled by applying a heat flux on the boundary region corresponding to the heater. Since the heaters are located on the surface of the wafer, the power generated by the heaters will be dissipated by convection as well as entering the wafer. Applying a heat balance to this surface of the wafer yields the boundary condition

$$k \left.\frac{dT}{dy}\right|_{y=L_y} + h_y T(L_y) = -q''_h(x,z) \tag{4.9}$$

The symmetry planes are modeled as insulated boundary conditions:

$$\left.\frac{dT}{dx}\right|_{x=0} = 0, \qquad \left.\frac{dT}{dy}\right|_{y=0} = 0, \qquad \text{and} \qquad \left.\frac{dT}{dz}\right|_{z=0} = 0 \tag{4.10}$$

Convection is assumed at the wafer edges, which yields the remaining two boundary conditions:

$$k \left.\frac{dT}{dx}\right|_{x=L_x} + h_x T(L_x) = 0 \tag{4.11}$$

$$k \left.\frac{dT}{dz}\right|_{z=L_z} + h_z T(L_z) = 0 \tag{4.12}$$

The three dimensional, homogeneous, steady-state heat equation,

$$\frac{\partial^2 T}{\partial x^2} + \frac{\partial^2 T}{\partial y^2} + \frac{\partial^2 T}{\partial z^2} = 0, \tag{4.13}$$

is solved subject to these boundary conditions, yielding

$$T(x,y,z) = \sum_{m=1}^{\inf} \sum_{n=1}^{\inf} C_{mn} \cos\beta_m x \cos\lambda_n z \cosh\gamma_{mn} y, \tag{4.14a}$$

where

$$C_{mn} = -\frac{4L_y}{L_x L_z k} \frac{C_{\beta m} C_{\lambda n}}{L_y \gamma_{mn} \sinh\gamma_{mn} L_y + Bi_y \cosh\gamma_{mn} L_y} I_{mn}, \tag{4.14b}$$

$$I_{mn} = \int_0^{L_x} \left(\int_0^{L_z} q''_h(x,z) \cos\lambda_n z dz \right) \cos\beta_m x dx. \tag{4.14c}$$

The heater array is divided into N rectangular regions, each producing a uniform heat flux. The x and z coordinates of the lower left and upper right corners of region i are (x_{i1}, z_{i1}) and (x_{i2}, z_{i2}), respectively. The heater regions ($y = L_y$) are projected onto the channel plane ($y = 0$); the average temperature of region i on the channel plane is:

$$T_i = \sum_{m=1}^{\infty} \sum_{n=1}^{\infty} C_{mn} S_{imn} \sum_{j=1}^{N} S_{jmn} q''_j, \tag{4.15a}$$

where

$$C_{mn} = \frac{4r_{xy}\cosh(\gamma_{mn}r_{xy}y)C_{\beta_m}C_{\lambda_n}}{\gamma_{mn}r_{xy}\sinh(\gamma_{mn}r_{xy}) + Bi_y\cosh(\gamma_{mn}r_{xy})}, \quad (4.15b)$$

$$C_{\beta_m} = \frac{{\beta_m}^2 + {Bi_x}^2}{{\beta_m}^2 + Bi_x + {Bi_x}^2}, \quad (4.15c)$$

$$C_{\lambda_n} = \frac{{\lambda_n}^2 + {Bi_z}^2}{{\lambda_n}^2 + Bi_z + {Bi_z}^2}, \quad (4.15d)$$

$$S_{kmn} = \frac{(\sin(\beta_m x_{k2}) - \sin(\beta_m x_{k1}))(\sin(\lambda_n z_{k2}) - \sin(\lambda_n z_{k1}))}{(x_{k2} - x_{k1})(z_{k2} - z_{k1})}, \quad (4.15e)$$

$$Bi_x = \frac{h_x L_x}{k}, \quad Bi_y = \frac{h_y L_y}{k} \text{ , and } \quad Bi_z = \frac{h_z L_z}{k}. \quad (4.15f)$$

The parameters β_m, λ_n, and γ_{mn} are given by the transcendental equations

$$Bi_x = \beta_m \tan\beta_m \quad (4.15g)$$

$$Bi_z = \lambda_n \tan\lambda_n \quad (4.15h)$$

$$\gamma_{mn} = \sqrt{{\beta_m}^2 + \left(\frac{\lambda_n}{r_{xz}}\right)^2}. \quad (4.15i)$$

Equation 4.15a is written in terms of the heat flux per unit area, q''. However, when designing the heaters, it is more convenient to work with the power dissipated per unit length of the heater, q':

$$q'' = \begin{cases} \dfrac{q'}{(z_{i2} - z_{i1})} & : \text{ Current in x direction} \\ \dfrac{q'}{(x_{i2} - x_{i1})} & : \text{ Current in z direction} \end{cases} \quad (4.16)$$

Equation 4.15a must be inverted to determine the heat flux distribution needed to generate the desired temperature distribution. Equation 4.15a can not be directly inverted. However, it can be converted into a matrix equation which may be invertible. To do so, a unit heat flux (1 W/m) is applied only to heater region j, and Equation 4.15a-4.15i is used to find the resulting channel temperature (B_{ij}) of region i on the channel plane. This relationship may be

written as

$$T_i = B_{ij} q'_j. \tag{4.17}$$

Equation 4.17 may be written for each value of i and j. These equations may be assembled into matrix form:

$$\vec{T} = \mathbf{B}\vec{q}' \tag{4.18}$$

The resulting B matrix is non-singular and can be easily inverted. However, if the desired temperature distribution is $\vec{T}_{tar}$, then using $\mathbf{B}^{-1}\vec{T}_{tar}$ results in a $\vec{q}$ whose elements alternate signs. Physically, this solution corresponds to a series of alternating heat sources and sinks. The thin film heaters will only generate heat, so this solution is physically meaningless. It is necessary to impose some physical constraints on the system to generate a useful solution. This is accomplished through a transformation matrix and constrained optimization. The heat loss increases substantially near the end of the heater, whereas the thermal gradients we are interested in require much smaller changes in heat flux. Therefore, it can be assumed that the heat flux will increase monotonically from the center of the heater to the end. This constraint is imposed by defining the heat flux in the first heater region (at the center of the heater) as q_1^*, then defining the heat flux in the next heater region as $q_1^* + q_2^*$, where q_2^* is the additional heat flux required in the second region. So for region i, the heat flux applied is equal to the heat flux applied to the previous region plus q_i^*. This can be written as:

$$\vec{q}' = \begin{Bmatrix} q'_1 \\ q'_2 \\ q'_3 \\ \vdots \\ q'_N \end{Bmatrix} = \begin{Bmatrix} q_1^* \\ q_1^* + q_2^* \\ q_1^* + q_2^* + q_3^* \\ \vdots \\ q_1^* + q_2^* + q_3^* + \cdots + q_N^* \end{Bmatrix} = \mathbf{A} \begin{Bmatrix} q_1^* \\ q_2^* \\ q_3^* \\ \vdots \\ q_N^* \end{Bmatrix} = \mathbf{A}\vec{q}^* \tag{4.19}$$

This transformation matrix is applied to Equation. 4.18:

$$\vec{T} = \mathbf{BA}\vec{q}^{*} = \mathbf{B}^{*}\vec{q}^{*}. \tag{4.20}$$

The optimization objective function is defined as

$$f(\vec{q}^{*}) = (\vec{T}_{tar} - \mathbf{B}^{*}\vec{q}^{*}) \cdot (\vec{T}_{tar} - \mathbf{B}^{*}\vec{q}^{*}). \tag{4.21}$$

This objective function is optimized using Rosen's gradient projection method [67] subject to the constraints

$$\vec{q}_i{}^{*} \geq 0 \tag{4.22}$$

Once the optimum $\vec{q}^{*}$ is found, the width of each heater segment is given by

$$w_i = \frac{I^2 R_s L}{q_i'}, \tag{4.23}$$

where I is the current, R_s is the sheet resistance (in Ω) of the thin film, L is the segments length, and Equation. 4.19 is used to convert from $\vec{q}^{*}$ to $\vec{q}'$.

4.3 Experimental

4.3.1 Sample Preparation

140bp model fragments containing single nucleotide polymorphisms (SNPs) were prepared by amplifying DNA Toolbox plasmid template DNA [10] via PCR. Briefly, 4 plasmids constructed by Highsmith et al. [10] , containing 40%-GC content and differing in sequence at one site, were amplified with the required primers to produce 140bp fragments. The forward primer was synthesized with a 40bp GC-rich region at the 5 -end for the purpose of artificially introducing a 40-mer GC clamp at one end of the amplified fragments. This GC clamp serves to prevent full denaturation of sample fragments into single stranded DNA, which would rapidly migrate through the system.

All amplifications consisted of a 50 l reaction volume that included 2.5 mM MgCl2, 1X PCR buffer, 200 M dNTPs, 1.0 U Taq polymerase, 10 ng of template DNA, and 40 pmol of each primer. Each reaction was executed for 40 cycles using a PE GeneAmp PCR System 9700 (Applied Biosystems, Foster City, CA). Heteroduplex formation was accomplished by combining equal volumes of the two analogous homoduplex samples. The mixture was heated to 94C for 3 minutes, and slowly cooled to room temperature.

4.3.2 Separation

The separations were performed in 5-cm long microfabricated channels with a 60 μm average width and 40 μm height. The microheaters established a thermal gradient that linearly increased from 65 °C to 75 °C over 1.5 cm along the separation channel length. The separations were performed at 150 V/cm electric field strength with 4.5% Poly(vinylpyrrolidone) (PVP; 360,000 MW) in 1X TBE buffer (89mM Tris, 89mM boric acid, 2mM EDTA) as the separation matrix. The DNA was labeled with YOYO-1 (491/509; Molecular Probes, Eugene, OR) intercalating fluorescent dye prior to analysis. Electropherograms were recorded at a sampling rate of 10Hz via Laser-Induced Fluorescence Detection (LIFD) with a 16-bit cooled CCD camera (Andor Technology, South Windsor, CT). The effective length of the separation was 4.0cm.

4.4 Results

4.4.1 Thermal Performance

The temperature distribution in the microchannel was verified by embedding an array of small gauge thermocouples in one of the microchannels. The

results are shown in Figure 4.8. The temperature in the microchannel was maintained to within 0.2°C of the desired temperature distribution, corresponding to a maximum temperature error of 0.5%. The temperatures measured by the thin film RTDs at the edge of the wafer must be slightly higher than the desired gradient to compensate for heat loss through the ends of the channel wafer.

4.4.2 Mutation Analysis

In preparing the model samples, 140bp fragments were amplified from each of two distinct plasmids. The selected plasmids contained sequences that were identical except at one site. The 140bp fragments were amplified individually to provide two distinct homoduplex samples with their forward strands containing T or G at the mutation site (position 88 on the PCR fragments). The samples containing T and G at the mutation site are designated as the wild-type and mutant fragments, respectively. The wild-type sample was left untreated and used as the homoduplex control for the analysis. In order to detect the presence of a change in sequence in the mutant sample, a portion of the wild-type and mutant samples were combined, denatured, and re-annealed to form heteroduplexes, as illustrated in Figure 4.1a. Due to the formation of mismatched base-pairing in the heteroduplex sample, a range of melting temperatures results among the double stranded DNA (dsDNA) species in the mixture. The mutation may now be detected by performing two TGGE separations, illustrated in Figure 4.1b-d. First, the homoduplex control sample is passed through the temperature gradient. Since only homoduplexes are present, a single large peak is detected, as shown in Figure 4.9a. Next, the mixed sample containing both heteroduplexes and homoduplexes is passed through the same temperature gradient, producing

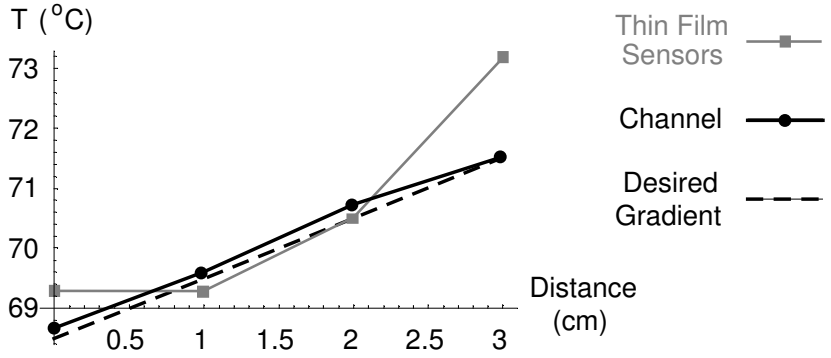

Figure 4.8: Thermal performance of TGGE system. The temperature in the microchannel was validated with an array of thermocouples embedded in the microchannel. The temperature at the edges of the heater wafer must be higher to compensate for heat loss through the channel wafer.

two large peaks, as shown in Figure 4.9b. The smaller peaks to the right of both electropherogram are sample contamination, most likely from the PCR process used to amplify the DNA samples. The electropherograms shown in Figure 4.9 were obtained using the integrated microfluidic system under the conditions described in Section 4.3.2.

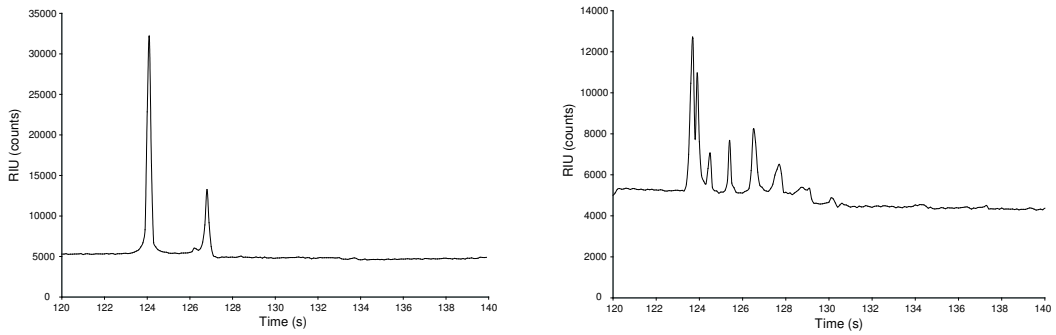

(a) (b)

Figure 4.9: Separation results. Sample containing only wild type DNA which produces only homoduplexes (a), and sample containing both wild type and mutant DNA which produces homoduplexes and heteroduplexes (b).

Chapter 5

Conclusions and Future Work

5.1 Conclusions

An analysis of the evaporation process and solubility of polymers is presented which may serve as a guide for developing processes compatible with injection moldable polymers. These analysis show the importance of heat management during evaporation and suggest ways to improve the deposited films. They also provide a method for selecting solvents which will not damage polymer substrates. Methods for patterning thin-film metal layers on PC and PMMA, creating and sealing microchannels in PC and PMMA, and making electrical and fluid connections are presented. Two example devices which illustrate different approaches to low cost polymer systems are discussed. One device utilizes microheaters and RTDs which are integrated directly into PC microchannels, while the other utilizes re-usable microheaters and RTDs. Methods of sensing two-dimensional temperature distributions are discussed, and the performance of thin-film RTDs fabricated on polycarbonate substrates is investigated.

Models are presented which may be used to predict the temperature distribution in a polymer microfluidic system due to an integrated heater, including the effect of fluid flow and thermal mixing within a microchannel. These models

are found to be in good agreement with measurements from a polycarbonate microfluidic device with integrated thin film microheaters and RTDs. This model should be helpful in the design process, allowing thermal effects to be accounted for in systems containing thermal powered actuators, hot plate sensors, heated chemical reactions, etc.

A microfluidic system is described which successfully detects the presence of sequence heterogeneity in a 140- bp heteroduplex DNA sample using TGGE as the separation mode. Microheaters and RTDs on a polymer substrate generate a controllable temperature gradient in a microchannel without the use of a heat sink. With this method, the necessary temperature gradient may be maintained in 10 parallel channels with less than one Watt of power. This system provides the basis for an inexpensive, disposable device for mutation screening.

5.2 Significant Contributions

- A lithography process which is completely compatible with the most commonly used injection/hot embossing polymers.
- A bonding process utilizing PDMS as an adhesive which does not expose thin metal layers on polymer substrates to high temperatures or damaging solvents.
- A simple and inexpensive method for fabricating polymer molds for hot embossing.
- A process for integrating diced chips in an inexpensive microfluidic system.
- A compact mathematical model for predicting microheater and RTD performance in polymer microfluidic systems.

5.3 Future Work

Although this work presents a variety of methods for fabricating low-cost polymer microfluidic devices, there are several areas which may be improved.

Metal deposition: The metal layers demonstrated in this study have resistivites which are often 10 times the handbook values or even greater, while the TCR values are half or less of their predicted values. This could be the result of contamination, which may be minimized by increasing deposition rate, or thermal effects, which may be minimized by shielding the wafer from radiation. A systematic study of the effect of deposition rates on film properties would lead to better metal films.

High density interconnects: Simple and reliable interconnects are achieved with printed circuit boards due to the excellent adhesion of a thick patternable copper film. However, the electrical interconnects to polycarbonate devices in this study have relied on silver filled epoxy, which is subject to oxidation and changes in electrical properties with time and temperature. No methods presently exist for depositing copper films with excellent adhesion to PC or PMMA substrates. Research in this area would lead to less expensive and more reliable devices.

Transient model: A one-dimensional transient model is presented which is a function of only the wafer thickness. However, the size and dimensions of the heater will certainly affect the time constant. A two or three dimensional model would be more accurate, and is important for applications such as bubble pumping and Polymerase Chain Reaction (PCR), where thermal time constants are critical.

BIBLIOGRAPHY

[1] S. Terry, J. Jermann, and J. Angell, "A gas chromatographic air analyzer fabricated on a silicon wafer," *IEEE Transactions on Electron Devices*, vol. ED-26, pp. 1880–1886, December 1979.

[2] J. Webster, M. Burns, D. Burke, and C. Mastrangelo, "Electrophoresis system with integrated on-chip fluorescence detection," in *Proceedings IEEE 13th Annual International Conference on MEMS*, pp. 306–310, January 2000.

[3] H. Fouckhardt, A. Grosse, M. Grewe, and M. Kuhnke, "Micro flow modules with combined fluid flow channel and optical detection waveguide - hyper rayleigh scattering as a case study," *Fresenius Journal of Analytical Chemistry*, vol. 371, pp. 218–227, July 2001.

[4] E. Lagally and R. Mathies, "Integrated pcr-ce system for dna analysis to the single molecule limit," in *Micro Total Analysis Systems 2001* (J. Ramsey and A. van den Berg, eds.), pp. 117–118, November 2001.

[5] B. Johnson *et al.*, "Microfabricated components for integrated chemical analysis," in *Proceedings of the Symposium on Microstructures and Microfabricated Systems IV*, pp. 43–53, Electrochemical Society, November 1998.

[6] J. Tsai and L. Lin, "A thermal bubble actuated micro nozzle-diffuser pump," in *Proceedings 14th IEEE International Conference on MEMS*, pp. 409–412, IEEE, January 2001.

[7] T. Lammerink, V. Spiering, M. Elwenspoek, J. Fluitman, and A. van den Berg, "Modular concept for fluid handling systems," in *Proceedings IEEE 9th Annual International Conference on MEMS*, pp. 389–394, IEEE, February 1996.

[8] J. McDonald, D. Duffy, *et al.*, "Fabrication of microfluidic systems in poly(dimethylsiloxane)," *Electrophoresis*, vol. 21, no. 1, pp. 27–40, 2000.

[9] D. Weston, T. Smekal, D. Rhine, and J. Blackwell, "Fabrication of microfluidic devices in silicon and plastic using plasma etching," *Journal of Vacuum Science and Technology B*, vol. 19, pp. 2846–2851, Nov/Dec 2001.

[10] T. Boone, H. Hooper, and D. Soane, "Integrated chemical analysis on plastic microfluidic devices," in *Solid-State Sensor and Actuator Workshop*, pp. 87–92, June 1998.

[11] W. Ropke *et al.*, "Manufacturing issues of polymer microfluidic devices with integrated electrodes for electrochemical detection of heavy metals in environmental samples," in *Micro Total Analysis Systems 2001* (J. Ramsey and A. van den Berg, eds.), pp. 183–184, November 2001.

[12] S. Metz, S. Gawad, and P. Renaud, "Flexible polyimide-based microchannels with embedded microelectrods," in *Micro Total Analysis Systems 2001* (J. Ramsey and A. van den Berg, eds.), pp. 171–172, November 2001.

[13] P. Man, D. Jones, and C. Mastrangelo, "Microfluidic plastic capillaries on silicon substrates: A new inexpensive technology for bioanalysis chips," in *Proceedings IEEE 10th Annual International Conference on MEMS*, pp. 311–316, IEEE, January 1997.

[14] J. Webster, M. Burns, D. Burke, and C. Mastrangelo, "An inexpensive plastic technology for microfabricated capillary electrophoresis chips," in *Micro Total Analysis Systems 1998*, pp. 249–252, October 1998.

[15] M. Zhao *et al.*, "Functional and efficient electrode-integrated microfluidic plastic devices," in *Micro Total Analysis Systems 2001* (J. Ramsey and A. van den Berg, eds.), pp. 193–194, November 2001.

[16] D. Armani and C. Liu, "Microfabrication technology for polycaprolactone, a biodegradable polymer," *Journal of Micromechanics and Microengineering*, vol. 10, pp. 80–84, March 2000.

[17] P. Sethu, H. Yu, P. Grodzinski, and C. Mastrangelo, "Fabrication of genetic analysis microsystems using plastic microcasting," in *Solid-State Sensor and Actuator Workshop*, pp. 175–178, June 2000.

[18] H. Yu *et al.*, "A miniaturized and integrated plastic thermal chemical reactor for genetic analysis," in *Micro Total Analysis Systems 2000* (A. van den Berg *et al.*, eds.), pp. 545–548, November 2000.

[19] D. Beebe *et al.*, "Microfluidic tectonics: A comprehensive construction platform for microfluidic systems," *Proceedings of the National Academy of Science*, vol. 97, pp. 13488–13493, December 2000.

[20] A. Wego, S. Richter, and L. Pagel, "Fluidic microsystems based on printed circuit board technology," *Journal of Micromechanics and Microengineering*, vol. 11, pp. 528–531, July 2001.

[21] T. Merkel, M. Graeber, and L. Pagel, "A new technology for fluidic microsystems based on pcb technology," *Sensors and Actuators A: Physical*, vol. 77, pp. 98–105, October 1999.

[22] K. Ikuta, T. Hasegawa, T. Adachi, and S. Maruo, "Fluid drive chips containing multiple pumps and switching valves for biochemical ic family," in *Proceedings IEEE 13th Annual International Conference on MEMS*, pp. 739–744, IEEE, January 2000.

[23] V. Varadan and V. Varadan, "Micro pump and venous valve by micro stereo lithography," in *Smart Structures and Materials 2000: Smart Electronics and MEMS*, vol. 3990, pp. 246–254, SPIE, 2000.

[24] D. Pugmire *et al.*, "Surface characterization of laser-ablated polymers used for microfluidics," *Analytical Chemistry*, vol. 74, pp. 871–878, September 1997.

[25] H. Becker and C. Gartner, "Polymer microfabrication methods for microfluidic analytical applications," *Electrophoresis*, vol. 21, no. 1, pp. 12–26, 2000.

[26] Y. Chiang, M. Bachman, C. Chu, and G. Li, "Characterizing the process of cast molding microfluidic systems," in *Microfluidic Devices and Systems II*, vol. 3877, pp. 303–311, SPIE, September 1999.

[27] "Dvd: The inside story," http://www.mtsu.edu/ dsmitche/rim456/DVD.PDF, 1995.

[28] A. Han, K. Oh, S. Khansali, H. Henderson, and C. Ahn, "A low temperature biochemically compatible bonding technique using fluoropolymers for biochemical microfluidic systems," in *Proceedings IEEE 13th Annual International Conference on MEMS*, pp. 414–418, IEEE, January 2000.

[29] M. Roberts, J. Rossier, P. Bercier, and H. Girault, "Uv laser machined polymer substrates for the development of microdiagnostic systems," *Analytical Chemistry*, vol. 69, pp. 2035–2042, June 1997.

[30] M. Taylor *et al.*, "Microfluidic bioanalysis cartridge with interchangeable microchannel separation components," in *Technical Digest of 11th International Conference on Solid State Sensors and Actuators (Transducers'01)*, pp. 1214–1217, June 2001.

[31] L. Martynova *et al.*, "Fabrication of plastic microfluid channels by imprinting methods," *Analytical Chemistry*, vol. 69, pp. 4783–4689, December 1997.

[32] K. Kamper *et al.*, "A self-filling low-cost membrane micropump," in *Proceedings IEEE 11th Annual International Conference on MEMS*, pp. 432–437, IEEE, January 1998.

[33] Y. Su and L. Lin, "Localized plastic bonding for micro assembly, packaging and liquid encapsulation," in *Proceedings IEEE 14th Annual International Conference on MEMS*, pp. 50–53, IEEE, January 2001.

[34] B. Grab *et al.*, "A new pmma microchip device for isotachophoresis with integrated conductivity detector," *Sensors and Actuators B: Chemical*, vol. 72, pp. 249–258, February 2001.

[35] J. Fahrenberg, W. Bier, D. Maas, W. Menz, R. Ruprecht, and W. Schomburg, "A microvalve system fabricated by thermoplastic molding," *Journal of Micromechanics and Microengineering*, vol. 5, pp. 169–171, June 1995.

[36] P. Yuen, L. Kricka, and P. Wilding, "Semi-disposable microvalves for use with microfabricated devices or microchips," *Journal of Micromechanics and Microengineering*, vol. 10, pp. 401–409, September 2000.

[37] C. Laritz and L. Pagel, "A microfluidic ph-regulation system based on printed ciruit board technology," *Sensors and Actuators A: Physical*, vol. 84, pp. 230–235, September 2000.

[38] N. Nguyen and X. Huang, "Miniature valveless pumps based on printed circuit board technique," *Sensors and Actuators A: Physical*, vol. 88, pp. 104–111, February 2001.

[39] T. Merkel, M. Graeber, L. Pagel, and H. Glock, "Electric fields in fluidic channels and sensor applications with capacitance," *Sensors and Actuators A: Physical*, vol. 80, pp. 1–7, March 2000.

[40] Y. Lin, C. Yang, and M. Huang, "Simulation and experimental validation of micro polymerase chain reaction chips," *Sensors and Actuators B: Chemical*, vol. 71, no. 2, pp. 127–133, 2000.

[41] C. Kimball, J. Buch, C. Lee, and D. DeVoe, "Temperature gradient gel electrophoresis in an integrated polycarbonate microsystem," in *Proceedings of Transducers'03*, vol. 1, pp. 24–27, 2003.

[42] D. Ross and L. Locascio, "Microfluidic temperature gradient focusing," *Analytical Chemistry*, vol. 74, no. 11, pp. 2556–2564, 2002.

[43] J. Tsai and L. Lin, "A thermal-bubble-actuated micronozzle-diffuser pump," *Journal of Microelectromechanical Systems*, vol. 11, no. 6, pp. 665–671, 2002.

[44] M. Baroncini *et al.*, "MEMS flow sensors for nano-fluidic applications," in *2001 International Symposium on VLSI Technology, Systems, and Applications*, pp. 164–167, IEEE, April 2001.

[45] S. Semancik *et al.*, "Microhotplate platforms for chemical sensor research," *Sensors and Actuators B: Chemical*, vol. 77, pp. 579–591, June 2001.

[46] S. Wu, Q. Lin, Y. Yuen, and Y. Tai, "MEMS flow sensors for nano-fluidic applications," *Sensors and Actuators A: Physical*, vol. 89, pp. 152–158, March 2001.

[47] N. Damean, P. Regtien, and M. Elwenspoek, "Heat transfer in a MEMS for microfluidics," *Sensors and Actuators A: Physical*, vol. 105, no. 2, pp. 137–149, 2003.

[48] J. Shackelford, *Introduction to Materials Science for Engineers*. Prentice-Hall, 1996.

[49] C. Moosbrugger and F. Cverna, *Electrical and Magnetic Properties of Metals*. ASM International, 2000.

[50] I. Brodie and J. Muray, *The physics of micro/nano-Fabrication*. Plenum, 1992.

[51] E. Brandes and G. Brook, eds., *Smithells metals reference book*. Butterworth Heinemann, 7 ed., 1992.

[52] A. Sala, *Radiant properties of materials*. Elsevier, 1986.

[53] A. Barton, *Handbook of Polymer-Liquid Interaction Parameters and Solubility Parameters*. CRC Press, 1990.

[54] J. Brydson, *Plastics Materials*. Butterworth Heinemann, 7th ed., 1999.

[55] A. Barton, *Handbook of Solubility Parameters and Other Cohesion Parameters*. CRC Press, 2nd ed., 1991.

[56] J. Wilbur and G. Whitesides, "Self-assembly and self-assembled monolayers in micro- and nanofabrication," in *Nanotechnology* (G. Timp, ed.), ch. 8, pp. 332–369, AIP Press, 1999.

[57] H. Lorenz, M. Laudon, and P. Renaud, "Mechanical characterization of a new high-aspect-ratio near uv-photoresist," *Microelectronic Engineering*, vol. 41, pp. 371–374, 1998.

[58] V. Hohreiter, S. Wereley, M. Olsen, and J. Chung, "Cross-correlation analysis for temperature measurement," *Measurement Science and Technology*, vol. 13, pp. 1072–1078, 2002.

[59] D. Ross, M. Gaitan, and L. Locascio, "Temperature measurement in microfluidic systems using a temperature-dependent fluorescent dye," *Analytical Chemistry*, vol. 73, pp. 4117–4123, September 2001.

[60] L. Zhu, C. Kimball, N.Sniadecki, S. Semancik, and D. DeVoe, "Integrated microfluidic gas sensors for water monitoring," in *Micro Total Analysis Systems 2003*, p. ??, 2003.

[61] C. Kimball and D. DeVoe, "Integrated thin film temperature sensors for polycarbonate microfluidics," in *Micro Total Analysis Systems 2002*, pp. 724–726, Kluwer, November 2002.

[62] T. Smekal, D. Rhine, D. Weston, and P. Grodzinski, "Design, fabrication, and tesing of thermal components and their integration into a microfluidic device," in *Eighth Intersociety Conference on Thermal and Thermomechanical Phenomena in Electronics Systems*, pp. 1039–1045, IEEE,ASME, May 2002.

[63] C. Kimballl and D. DeVoe, "Theoretical and experimental analysis of thermal transport in polymer microchannels," in *Micro Total Analysis Systems 2003*, p. ??, 2003.

[64] H. Park, J. Pak, S. Son, G. Lim, and I. Song, "Fabrication of a microchannel integrated with inner sensors and the analysis of its laminar flow characteristics," *Sensors and Actuators A: Physical*, vol. 103, no. 3, pp. 317–329, 2003.

[65] F. Incropera and D. DeWitt, *Fundamentals of Heat and Mass Transfer*. Wiley, third ed., 1990.

[66] J. Beck, K. Cole, A. Haji-Sheikh, and B. Litkouhi, *Heat Conduction using Green's Functions*. Hemisphere Publishing, 1992.

[67] A. Belegundu and T. Chandrupatla, *Optimization Concepts and Applications in Engineering*. Prentice Hall, 1999.

[68] A. Nataraj, I. Olivos-Glander, N. Kusukawa, and W. Highsmith, "Single-strand conformation polymorphism and heteroduplex analysis for gel-based mutation detection," *Electrophoresis*, vol. 20, no. 6, pp. 1177–1185, 1999.

[69] N. Arnold, E. Gross, U. Schwarz-Boeger, J. Pfisterer, W. Jonat, and M. Kiechle, "A highly sensitive, fast, and economical technique for muta-

tion analysis in hereditary breast and ovarian cancers," *Human Mutations*, vol. 14, no. 4, pp. 333–339, 1999.

[70] E. Gross, N. Arnold, J. Goette, U. Schwarz-Boeger, and M. Kiechle, "A comparison of BRCA1 mutation analysis by direct sequencing, SSCP and DHPPLC," *Human Genetics*, vol. 105, no. 1, pp. 72–78, 1999.

[71] D. Riesner, G. Steger, R. Zimmat, R. Owens, M. Wagonhofer, W. Hillen, S. Vollbach, and K. Henco, "Temperature-gradient gel electrophoresis of nucleic acids: analysis of conformational transitions, sequence variations, and protein-nucleic acid interactions.," *Electrophoresis*, vol. 10, no. 5, pp. 377–389, 1989.

[72] Q. Gao and E. Yeung, "High-throughput detection of unknown mutations by using multiplexed capillary electrophoresis with poly(vinylpyrrolidone) solution," *Analytical Chemistry*, vol. 72, no. 11, pp. 2499–2506, 2000.

[73] L. Zhu, H. Lee, B. Lin, and E. Yeung, "Spatial temperature gradient capillary electrophoresis for DNA mutation detection," *Electrophoresis*, vol. 22, no. 17, pp. 3683–3687, 2001.

[74] H. Mao, A. Holden, M. You, and P. Cremer, "Reusable platforms for high-throughput on-chip temperature gradient assays," *Analytical Chemistry*, vol. 74, no. 19, pp. 5071–5075, 2002.